

**FINITE ELEMENT SIMULATION OF  
ATHEROSCLEROTIC PLAQUE  
THROUGH MORPHOELASTICITY**

by

Navid Mohammad Mirzaei

A dissertation submitted to the Faculty of the University of Delaware in partial fulfillment of the requirements for the degree of Doctor of Philosophy in Applied Mathematics

Summer 2020

© 2020 Navid Mohammad Mirzaei  
All Rights Reserved

## ACKNOWLEDGEMENTS

Firstly, I would like to express my sincere gratitude to my advisor Dr. Fok for his guidance during my time as a PhD student. His thoughtful comments and recommendations on this dissertation have made me a better researcher and writer. His patience and resourcefulness will continue to be a model for me to follow as I continue my journey in academia.

Besides my advisor, I would like to thank the rest of my thesis committee: Dr. Braun, Dr. Guyenne and Dr. Zurakowski. In addition to their insightful comments on and encouragement for this dissertation they have had tremendous impact upon me as a student in their courses; without the knowledge I built there I would not have made it here.

I also would like to thank the University of Delaware, especially the Department of Mathematical Sciences for the trust they put in me. Ewing Hall has provided me a second home and incredible friends over the past 5 years, whose support in this endeavor is immesurable.

In addition, I would like to acknowledge Delaware-CTR Accel program who partially funded this dissertation.

Special thanks to my parents and my sister for encouraging me to apply abroad and supporthing me financially and emotionally to take this leap of faith. I would not be here if it was not for them.

Last but not least, I thank my wife. She has been my best friend and my biggest motivatior since the start of graduate school. This journey would not have been as exciting, fun, or fufilling without her by my side.

## TABLE OF CONTENTS

<b>LIST OF TABLES . . . . .</b>	<b>iv</b>
<b>LIST OF FIGURES . . . . .</b>	<b>v</b>
<b>ABSTRACT . . . . .</b>	<b>xi</b>
Chapter	
<b>1 INTRODUCTION . . . . .</b>	<b>1</b>
1.1 Atherosclerosis . . . . .	1
1.2 Literature Review . . . . .	5
1.3 Mechanical aspect and Morphoelasticity . . . . .	10
1.4 Aim of this thesis . . . . .	14
<b>2 ATHEROSCLEROSIS MODEL IN CYLINDRICAL COORDINATES . . . . .</b>	<b>16</b>
2.1 Weak formulation in cylindrical coordinates . . . . .	20
2.2 Assumptions . . . . .	27
2.3 The effect of pure growth in each direction . . . . .	27
2.3.1 Pure radial growth . . . . .	28
2.3.2 Pure circumferential growth . . . . .	30
2.3.3 Pure axial growth . . . . .	31
2.4 Growth and energy change . . . . .	32
2.5 Isotropic Growth vs General Anisotropic Growth . . . . .	34
2.6 Conclusion . . . . .	40
<b>3 ATHEROSCLEROSIS MODEL IN THREE DIMENSIONS . . . . .</b>	<b>42</b>
3.1 Assumptions and methods . . . . .	43
3.1.1 Coordinate system transformation . . . . .	47

3.1.2	Results . . . . .	49
3.2	Conclusion . . . . .	57
<b>4</b>	<b>ATHEROSCLEROSIS IN 3D WITH HISTOLOGY . . . . .</b>	<b>60</b>
4.1	Methods and assumptions . . . . .	63
4.1.1	System of PDEs . . . . .	65
4.1.2	PDGF equation . . . . .	69
4.2	Mechanisms . . . . .	71
4.2.1	Case A . . . . .	73
4.2.2	Case B . . . . .	76
4.2.3	Case C . . . . .	79
4.2.4	Case D . . . . .	79
4.2.5	Case E . . . . .	83
4.3	Conclusion . . . . .	85
<b>5</b>	<b>CONCLUSION . . . . .</b>	<b>87</b>
<b>BIBLIOGRAPHY . . . . .</b>		<b>90</b>
<b>Appendix</b>		
<b>A</b>	<b>DOMAIN AND MESH GENERATION . . . . .</b>	<b>100</b>
<b>B</b>	<b>PARAMETERS FOR GAUSSIAN FUNCTIONS . . . . .</b>	<b>103</b>

## LIST OF TABLES

2.1	List of parameter values used in this thesis. . . . .	25
2.2	Blood pressure category by American Heart Association. . . . .	27
2.3	Energy in $\mu J$ for 6 time values. . . . .	33
4.1	Size of necrotic core in advanced plaques. See pages 22 and 39 of [98] for diagrams.	60
4.2	Time-dependent parameters for Case A. The time variable $t$ changes from 0 to 12 months. . . . .	75
4.3	Time-dependent parameters for Case B. The time variable $t$ changes from 0 to 12 months. . . . .	76
4.4	Time-dependent parameters for Case C. The time variable $t$ changes from 0 to 12 months. . . . .	79
4.5	Time-dependent parameters for Case D. The time variable $t$ changes from 0 to 12 months. . . . .	80
4.6	Time-dependent parameters for Case E. The time variable $t$ changes from 0 to 12 months. . . . .	83
4.7	Parameter values for equations (4.1)-(4.4) and equations (4.15) and (4.16) used to generate Figures 4.8 to 4.18. Abbreviations: MC = Macrophage Cells, NC = Necrotic Cells, O <sub>2</sub> = Oxygen, PDGF = Platelet Derived Growth Factor. . . . .	84
B.1	Parameters for equation (4.21). . . . .	103
B.2	Parameters for equation (4.22) and (4.23). . . . .	104

## LIST OF FIGURES

1.1	(a) Three layer schematic structure of arteries. The boundary $A$ is the endothelium and the lumen is where the blood flows. (b) A healthy coronary artery cross section courtesy of Diego et al. [20]. . . . .	2
1.2	Schematic of atherosclerosis histology. The pink region here and the internal elastic lamina correspond to the intima and boundary B in Figure 1.1. . . . .	4
1.3	(a) Remodeling behavior depends on whether stenosis (eq. 1.1) is less than or greater than 30%. With the same data, Glagov et al. were also able to fit a piecewise linear curve with a jump in derivative at about 30% [34]. In this case, the curve gently increases when stenosis is less than 30% and decreased when the stenosis was more than 30%. (b) Schematic showing what happens to the vessel wall inferred from Glagov's data. . . . .	9
1.4	Angiography will not be able to distinguish between cases 1 and 2. However, according to formula (1.1) the stenosis in case 2 is larger than case 1. . . . .	10
1.5	Deformation of domain $\Omega$ via the deformation vector field $\varphi(X, Y, Z)$ . Every point $(X, Y, Z)$ in the reference domain gets mapped to a point in the deformed domain $\omega$ by $\varphi(X, Y, Z)$ . . . . .	10
1.6	Deformation gradient decomposition based on morphoelasticity. Configurations in red are incompatible due to overlapping elements. . . . .	12
1.7	Going from the reference state to state 2 we apply $\mathbf{F}_1^* \mathbf{F}_1 = \mathbf{F}_{e_1}^* \mathbf{G}_1^* \mathbf{F}_{e_1} \mathbf{G}_1$ . However, $\mathbf{F}_{e_1}^*$ and $\mathbf{G}_1$ do not necessarily commute. Therefore, in general $\mathbf{F}_1^* \mathbf{F}_1 = \mathbf{F}_{e_1}^* \mathbf{G}_1^* \mathbf{F}_{e_1} \mathbf{G}_1$ cannot be written as $\mathbf{F}_2 = \mathbf{F}_{e_2} \mathbf{G}_2$ which is required in the Morphoelasticity framework. . . . .	13
2.1	(a) Mathematical reference domain with subdomains and boundary labels. (b) Mathematical deformed domain with subdomains and boundary labels. We use lower case letters for the deformed domain. (c) Plan view of the artery and the orientation of representative fibers. Vector $\mathbf{b}$ is defined for each layer by (2.30) and the values of $\varphi$ for each layer are given in Table 2.1. . . . .	18

2.2	<i>Top:</i> The unpressurized reference domain. <i>Middle:</i> The reference domain after applying the blood pressure of 16 kPa. <i>Bottom:</i> Mesh sample for $-0.58 \leq Z \leq 0.58$ . Mesh is denser where growth is larger. . . . .	28
2.3	Evolution of the domain for $-0.58 \leq Z \leq 0.58$ subject to (a) pure radial growth with $(\alpha, \beta, \gamma) = (1, 0, 0)$ , (b) pure circumferential growth with $(\alpha, \beta, \gamma) = (0, 1, 0)$ and (c) pure axial growth with $(\alpha, \beta, \gamma) = (0, 0, 1)$ . The material point at A moves to the right under the effect of axial growth. Parameter $a$ in (2.32)-(2.34) is taken to be 14.29. . . . .	29
2.4	<i>Left:</i> Lumen area against stenosis. Star denotes the time $t = 0$ . <i>Right:</i> Lumen area in time. With pure radial growth close to the center of growth $Z = 0$ the remodeling is strictly inward. . . . .	30
2.5	<i>Left:</i> Lumen area against stenosis. Star denotes the time $t = 0$ . <i>Right:</i> Lumen area in time. With pure circumferential growth close to the center of growth $Z = 0$ the remodeling is mostly outward. . . . .	31
2.6	<i>Left:</i> Lumen area against stenosis. Star denotes the time $t = 0$ . <i>Right:</i> Lumen area in time. With pure axial growth close to the center of growth $Z = 0$ the remodeling is mostly outward with no significant increase in stenosis. . . . .	32
2.7	The changes in total strain energy for growth in each direction. . . . .	34
2.8	Changes in anisotropic growth parameters $\alpha_t, \beta_t, \gamma_t$ and isotropic growth parameter $\xi_t$ . . . . .	36
2.9	Evolution of the domain for $-0.58 \leq Z \leq 0.58$ subject to (a) isotropic growth with $\xi_t$ from Fig. 2.8, (b) general anisotropic growth with $(\alpha_t, \beta_t, \gamma_t)$ from Fig. 2.8. Parameter $a$ in (2.32)-(2.34) is taken to be 14.29. . . . .	37
2.10	<i>Left:</i> Comparison between the lumen area against stenosis for both isotropic and anisotropic growth. Star denotes the time $t = 0$ . <i>Right:</i> Comparison between the lumen area in time for both isotropic and anisotropic growth. <i>Dashed</i> lines correspond to isotropic and <i>solid</i> lines correspond to anisotropic growth. . . . .	38
2.11	Changes in the strain energy produced by isotropic and anisotropic growth in time. . . . .	38

2.12	<i>Top:</i> These graphs belong to the case of isotropic growth with $\xi_t$ from Fig. 2.8. (a) Changes in the minimum and maximum fiber angles. (b) Changes in the maximum of $I_4$ in each layer. <i>Bottom:</i> These graphs correspond to the anisotropic growth with $(\alpha_t, \beta_t, \gamma_t)$ from Fig. 2.8. (c) Changes in the minimum and maximum fiber angles. (d) Changes in the maximum of $I_4$ in each layer. . . . .	39
3.1	A radial cut on an annular arterial cross section causes it to spring open. This is evidence for residual stress. The angle shown in 2 is the opening angle. . . . .	43
3.2	<i>Left:</i> IVUS image of a coronary artery cross section. <i>Right:</i> Our three-layer domain. . . . .	44
3.3	<i>Top:</i> Side view and front view of a family of fibers. The fiber direction at an inner point B is the average of inner and outer boundary unit tangent vectors at the points closest to B. The weight is determined by the distance between points. <i>Bottom:</i> The fiber orientations in each layer at a cross section of our 3D domain.	46
3.4	A sample mesh. . . . .	47
3.5	Fiber coordinate system at a point $(X, Y, Z)$ . Red arrow pointing outside of the domain is $\mathbf{e}_R$ , blue arrow is $\mathbf{e}_\Phi$ and the purple arrow is $\mathbf{e}_Z$ . . . . .	48
3.6	Local growth centered at $(X_0, Y_0, Z_0) = (0, -0.8, 0)$ . . . . .	49
3.7	(a) Schematic of the fiber coordinate system in the reference uncut domain at a random point and a point on the site of the radial cut. Red, blue and purple arrows correspond to radial, fiber and axial directions in the fiber coordinate system. (b) The hinge of the opening angle is at the intersection of the endothelium with the plane $x = 0$ . (c) Deformed arterial sections due to growth in the (i) radial direction, (ii) fiber direction and (iii) axial direction. . . . .	50
3.8	Changes in growth tensor entries in time. . . . .	52
3.9	Anisotropic growth. <i>Top:</i> Changes in the opening angle. <i>Bottom:</i> Evolution of the intact domain. The hinge of the opening angle is the intersection of the endothelium with the plane $x = 0$ , see Figure 3.7(b) . . . . .	52
3.10	Isotropic growth. <i>Top:</i> Changes in the opening angle. <i>Bottom:</i> Evolution of the intact domain. The hinge of the opening angle is the intersection of the endothelium with the plane $x = 0$ , see Figure 3.7(b). . . . .	53
3.11	<i>Left:</i> The opening angle as a function of time. <i>Right:</i> The opening angle as a function of stenosis. Stars mark every 0.1 decade. . . . .	53

3.12	Strains in radial, fiber and axial directions for anisotropic growth. . . . .	55
3.13	Strains in radial, fiber and axial directions for isotropic growth. . . . .	56
3.14	Maximum strains in radial, fiber and axial directions for anisotropic (solid) and isotropic (dashed) growth. . . . .	57
4.1	IVUS images taken from Kubo et al. 2010 [54]. The baseline and follow-up images were acquired within a year of each other. Gray scale images are the original IVUS images and the colored ones are acquired after spectrum classification of plaque structure. The red corresponds to necrotic regions and the white speckles are signs of calcification. Green shows fibrotic regions free of necrosis and calcification and yellow represents the fibrofatty regions. Blue arrows show the orientation of the catheter head. White arrows mark the location of Thin Cap Fibroatheromas (TCFA). . . . .	62
4.2	First column: IVUS images. Second and third columns: computer generated domains. . . . .	64
4.3	Arrows show the areas with the most intense fluorescence, indicating the presence of NITP, a marker of hypoxia, [8]. . . . .	67
4.4	(MC = Macrophage Cells). A simulation showing the effect of macrophage density and intima thickness on necrosis. The parameters used for this simulation are similar to the parameters from case B in Table 4.7 except low density of MC corresponds to $M_0(t) = 4.6 \times 10^3$ cells/cm <sup>3</sup> and high density of MC corresponds to $M_0(t) = 4.6 \times 10^5$ cells/cm <sup>3</sup> . We have manually changed the thickness of the domain to show the effect of intimal thickening on necrosis. <i>Top</i> : No necrosis in the intima with thickness < 30 $\mu\text{m}$ and macrophage density $10^5$ cells/cm <sup>3</sup> . <i>Middle</i> : No necrosis in the intima with thickness > 30 $\mu\text{m}$ and macrophage density < $10^5$ cells/cm <sup>3</sup> . <i>Bottom</i> : Necrotic intima with thickness > 30 $\mu\text{m}$ and macrophage density > $10^5$ cells/cm <sup>3</sup> . . . . .	68
4.5	PDGF produced by platelets of endothelial cells promote cell proliferation at the site of an injury or endothelial dysfunction. . . . .	69
4.6	Flowchart of our algorithm. . . . .	71
4.7	Threshold value $1.4 \times 10^6$ cells/cm <sup>3</sup> represented by a plane. Densities above this value (above the plane) are considered necrotic. . . . .	73

4.8	Typical 3D plaque model results. Baseline concentrations of NC, Chemoattractant, oxLDL, MC and and oxygen are outputted as spatially dependent fields distributed in the intima. For PDGF concentration, the media and adventitia are also indicated along with the finite element mesh. . . . .	74
4.9	Typical 3D plaque model results. Follow-up concentrations of NC, Chemoattractant, oxLDL, MC and and oxygen are outputted as spatially dependent fields distributed in the intima. For PDGF concentration, the media and adventitia are also indicated along with the finite element mesh. See tables 4.2 -4.7 for parameter values. . . . .	74
4.10	Necrotic core in baseline and follow-up state for the intimal cross section at $Z = 0$ . . . . .	75
4.11	Typical 2D plaque model results. Baseline concentrations of NC, Chemoattractant, oxLDL, MC and and oxygen are outputted as spatially dependent fields distributed in the intima. No PDGF concentration has been considered for this case. . . . .	77
4.12	Typical 2D plaque model results. Follow-up concentrations of NC, Chemoattractant, oxLDL, MC and and oxygen are outputted as spatially dependent fields distributed in the intima. PDGF is absent for this case. See tables 4.3-4.7 for parameter values. . . . .	77
4.13	Typical 2D plaque model results. Baseline concentrations of NC, Chemoattractant, oxLDL, MC and and oxygen are outputted as spatially dependent fields distributed in the intima. For PDGF concentration, the media and adventitia are also indicated along with the finite element mesh. . . . .	78
4.14	Typical 2D plaque model results. Follow-up concentrations of NC, Chemoattractant, oxLDL, MC and and oxygen are outputted as spatially dependent fields distributed in the intima. For PDGF concentration, the media and adventitia are also indicated along with the finite element mesh. See tables 4.4-4.7 for parameter values. . . . .	78
4.15	Typical 2D plaque model results. Baseline concentrations of NC, Chemoattractant, oxLDL, MC and and oxygen are outputted as spatially dependent fields distributed in the intima. For PDGF concentration, the media and adventitia are also indicated along with the finite element mesh. . . . .	81

4.16	Typical 2D plaque model results. Follow-up concentrations of NC, Chemoattractant, oxLDL, MC and and oxygen are outputted as spatially dependent fields distributed in the intima. For PDGF concentration, the media and adventitia are also indicated along with the finite element mesh. See tables 4.5-4.7 for parameter values. . . . .	81
4.17	Typical 2D plaque model results. Baseline concentrations of NC, Chemoattractant, oxLDL, MC and and oxygen are outputted as spatially dependent fields distributed in the intima. For PDGF concentration, the media and adventitia are also indicated along with the finite element mesh. . . . .	82
4.18	Typical 2D plaque model results. Follow-up concentrations of NC, Chemoattractant, oxLDL, MC and and oxygen are outputted as spatially dependent fields distributed in the intima. For PDGF concentration, the media and adventitia are also indicated along with the finite element mesh. See tables 4.6-4.7 for parameter values. . . . .	82
A.1	A sample 3D domain and its meshed version in GMSH environment . . . . .	101

## ABSTRACT

Atherosclerosis is a disease which can cause a narrowing of the blood vessels therefore reducing the blood flow. It is one of the leading causes of death in the world. Under-standing the behavior and dynamics of the vessel wall before and after atherosclerosis has been a motivation for many studies. We investigate this phenomenon as a combi-nation of mechanical deformation of the vessel wall along with cell and chemical dynamics that occur within.

In chapter 2 of this thesis, we investigate this phenomenon as a pure mechanical deformation to learn how growth anisotropy affects the deformation of the arterial wall. We consider the vessel wall as a growing hyperelastic material with three layers. To describe tissue growth, we use morphoelasticity as the mathematical framework. Then we investigate the effect of anisotropic growth on arterial wall remodeling in five different cases: pure radial, pure circumferential, pure axial, isotropic and general anisotropic growth. We speculate that the nature of anisotropy is inclined towards the growth direction that requires the least amount of energy. We propose a scheme that minimizes the energy with respect to the displacement and growth anisotropy.

In chapter 3, we utilize our results to see the effect of the most energetically favorable growth on an essential mechanical property of the vessel wall: the opening angle which is a measure of residual strain. We use a general 3D domain and investigate the changes in the opening angle with respect to growth in each separate direction. We notice that the growth in the circumferential direction has a more significant effect on the opening angle than the other two directions. We also compare the opening angle and the strain in the most energetically favorable anisotropic case with an isotropic growth regime. Due to the geometry of the cross section (specifically the axial length of the domain) the anisotropic and isotropic growth show similar results.

Finally in chapter 4, we use an integrated model that also includes cell and chemical dynamics that occur within the arterial wall. The growth tensor now is a function of Platelet Derived Growth Factor (PDGF). In this part, we explore the distribution of oxidized lipids, macrophages, foam cells, oxygen and necrotic cells in the intima at each growth step via a system of partial differential equations. Altogether, this allows us to observe intimal thickening as a result of PDGF-induced vessel growth along with histological changes within the wall such as the development of necrotic zones. Our simulations show results similar to the images acquired from ultrasound scans.

# Chapter 1

## INTRODUCTION

### 1.1 Atherosclerosis

Our cardiovascular system is one of the most vital systems in our body responsible for many important tasks among which are: transportation of nutrients, oxygen, hormones and blood cells to our body organs as well as fighting diseases and stabilizing our body temperature and pH. Blood vessels are the pathways for blood and consist of three layers; intima, media and adventitia, see Figure 1.1. The blood flows in the lumen and the interface that separates lumen from the intima is called the endothelium which consists of a thin layer of cells called endothelial cells. These cells have many functions such as homeostasis, hormone trafficking, protecting the intima from harmful substances in the blood flow and white blood cell recruitment. Cardiovascular disease (CVD) has always been a major challenge in the medical realm. Not only does it impose a threat to global health but it also carries a heavy economic burden. According to the American Heart Association, in 2016, CVD cost America \$555 billion. By 2035, the cost will skyrocket to \$1.1 trillion [2]. It has affected more than 121 million people in 2016 in the United States and about 48% of adults [7]. Atherosclerosis is one manifestation of CVD, which causes the arteries to narrow due to plaque build-up. This disease dates back more than 3500 years and it has been observed in Egyptian mummies from 1580 BCE [98] and it has been the subject of many medical articles [50, 40, 22, 23, 80]. Atherosclerosis can cause angina and might lead to more serious problems such as heart-attack, stroke or even death. Atherosclerotic lesions present different structures and stages. Necrosis is one of these stages and it happens as a result of cell death due to injury or lack of nutrients and oxygen. However, Necrosis

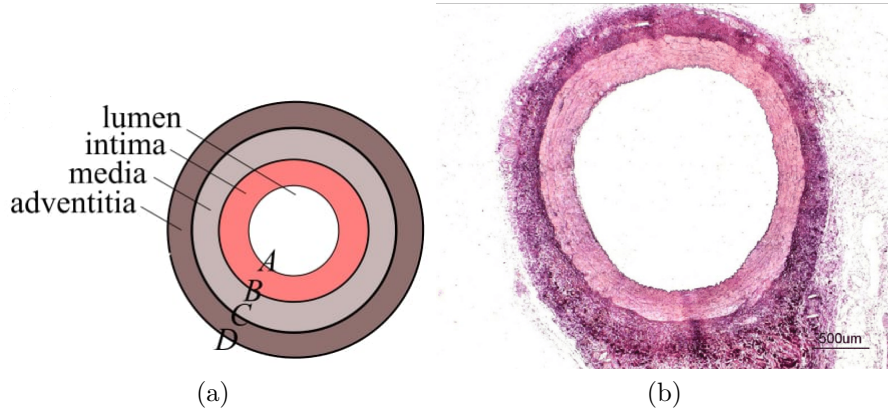


Figure 1.1: (a) Three layer schematic structure of arteries. The boundary *A* is the endothelium and the lumen is where the blood flows. (b) A healthy coronary artery cross section courtesy of Diego et al. [20].

and cell death are not the same, but cell death is a precursor to necrosis. It takes some time for the dead cells to become necrotic. They have to go through irreversible genetic changes to qualify as necrotic cells [62].

Early atherosclerotic lesions divide into three subcategories [98]:

- **Pathologic intimal thickening:** There is an abundance of smooth muscle cells (SMC) in this plaque in addition to the presence of proteoglycan<sup>1</sup> matrix and focal accumulation of extracellular lipid.
- **Fibrous cap atheroma:** During early necrosis, macrophages infiltrate into lipid pools with an overlying fibrous cap<sup>2</sup>. During later stages of necrosis, one can observe matrix loss and extensive cellular debris.
- **Thin cap fibroatheroma:** In this stage a thin, fibrous cap (< 65 μm) is infiltrated by macrophages and lymphocytes with rare or few SMCs and a relatively large underlying necrotic core; intraplaque hemorrhage/fibrin may be present.

---

<sup>1</sup> A compound consisting of a protein bonded to glycosaminoglycan groups, present especially in connective tissue.

<sup>2</sup> The fibrous cap is a layer of fibrous connective tissue, which is thicker and less cellular than the normal intima, found in atherosclerotic plaques.

See page 39 of [98] for diagrams.

More advanced lesions present acute thrombi<sup>3</sup>. Most acute coronary syndromes are caused by luminal thrombi, which arise from three different plaque morphologies: rupture, erosion and calcified nodules

- **Ruptured plaque:** These plaques have a significant necrotic core that causes thrombus as a result of physical contact with platelets. This happens after a mechanical rupture in the thin fibrous cap. In fact, ruptured plaques are a natural progression from thin cap fibroatheromas and can cause acute events such as myocardial infarction (MI).
- **Eroded plaque:** Unlike rupture, eroded plaques have little to no necrotic core and the fibrous cap remains thick and intact. The thrombosis happens on top of a smooth muscle cell and proteoglycan-rich plaque. This thrombus is often called a white thrombus as opposed to the red thrombus caused by rupture.
- **Calcified nodule:** The least common type of plaques are calcified nodules. These lesions contain calcified plates and bony nodules that erupt into a lumen. The intima contains few endothelial cells.

See page 22 of [98] for pictures.

Atherosclerosis is an intricate biological phenomenon that involves many biochemical factors. Low blood flow imposed shear stress plays an essential role in triggering atherosclerosis [57, 66, 19, 63]. Healthy endothelial cells produce a certain amount of nitric oxide (NO) which is a vasodilator. Decrease in laminar shear stress reduces the production of this chemical which leads to endothelial dysfunction. This increases the permeability of the endothelium to low density lipoproteins (LDL) as well as the production of Vascular Cell Adhesion Molecule-1 (VCAM-1). These adhesive molecules start an inflammatory process by binding with Intracellular Adhesion

---

<sup>3</sup> A blood clot formed within the artery which impedes blood flow.

Molecule-1 (ICAM-1) on the surface of leukocytes present in the blood stream. Attached to the endothelium, leukocytes penetrate the vessel wall in response to chemoattractant (MCP-1) present in the intima. Once inside, macrophage colony stimulating factor (M-CSF) causes them to go through morphogenesis and turn into macrophages. LDLs that have infiltrated the intima go through oxidization and turn into oxidized LDLs. Macrophages cause inflammation and release more chemoattractant. They also consume oxidized LDLs and turn into foam cells, see Figure 1.2. SMCs can also migrate into the plaque from the underlying media and consume oxidized LDLs but at a much lower rate than the macrophages. The death of SMCs, foam cells and macrophages all contribute to a necrotic core, one of the defining characteristics of a vulnerable plaque (rupture-prone plaque) [57, 98].

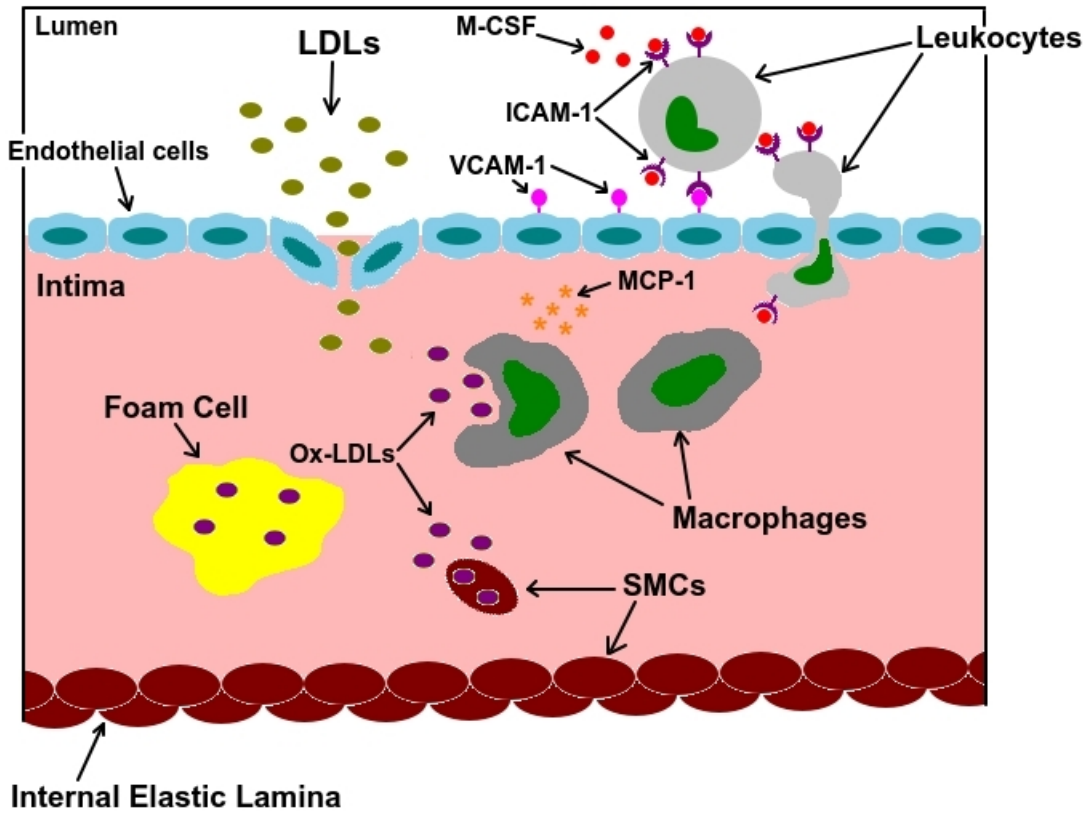


Figure 1.2: Schematic of atherosclerosis histology. The pink region here and the internal elastic lamina correspond to the intima and boundary B in Figure 1.1.

The plaque build-up in atherosclerosis is often associated with a thickened intima. Intimal thickening (IT) is one of the most important factors in assessing cardiovascular risk and one of the most common methods in measuring the progression of atherosclerosis. However, it is quite different from atherosclerosis as in IT the associated lesions are less inflamed since inflammatory agents like macrophages are almost non-existent inside the intima. IT is considered to be an important precursor to atherosclerosis [51, 96, 69]. Thickened intimas are often thought as the “soil” for atherosclerosis. This phrase was coined by Schwartz [86].

## 1.2 Literature Review

There are many studies that try to understand the cell and chemical dynamics of intimal thickening and atherosclerosis. Here we briefly introduce a few different points of view. One well known example is Hao and Friedmans study [41]. They had most of the key players including a velocity field which was the result of movement of macrophages, T-cells and smooth muscle cells into the intima. This procedure promoted intimal thickening. Their model, however, did not consider the mechanical properties of the intima and neglected the other two layers of the vessel wall. Chalmers et al. used differential equations to purely explore the dynamics of early atherosclerosis [15]. Their model considered the concentration of LDLs, chemoattractants, Endothelium-Stimulating (ES) cytokines, macrophages and foam cells. All of their simulations were done in one dimension and their result provided qualitative and quantitative insight into the effect of LDL penetration in the inflammatory response. In 2017, Chalmers et al. further investigated the effect of High Density Lipoproteins (HDL) in plaque regression [14]. They observed that increasing HDL influx regresses plaques with a low density of foam cells and slows the growth of plaques with a high density of foam cells. El Khatib et al. suggested that inflammation propagates in the intima as a reaction diffusion wave [21]. They concluded that in the case of intermediate LDL concentrations there are two stable equilibria: one corresponding to the disease free state and the other one to the inflammatory state while the traveling wave connects these two

states. Fok investigated the effect of the spatial distribution of oxidized LDL on the location and size of the necrotic core [24]. He predicted the location and size of the necrotic core due to the chemotaxis of macrophages towards sources of oxidized LDLs and their death due to lack of oxygen. Cobbold et al. investigated the deposition of cholesterol as a result of LDL oxidation using a system of ODEs [18]. In their system, they considered the concentration of antioxidants specifically vitamin E and vitamin C, HDL, LDL and free radicals. They showed that vitamin E supplementation is not as beneficial as HDL and vitamin C for hindering the oxidation process.

Blood vessels present mechanical behaviors that are interesting to many researchers in different disciplines. Investigating the mechanical properties of the blood vessels is an essential step towards understanding cardiovascular diseases. Fung, the founder of modern biomechanics has many contributions to this field. One of his important findings was the formulation of residual stress (remaining stress in a load-free arterial cross section) as a function of the opening angle. He noticed that when load-free cross sections of arteries were cut radially they sprang open. With this being evidence of residual stress, he proposed a formula to relate the opening angle of the cut sector to the residual stress in the load free cross section [16]. Thereafter, the concept of residual strain/stress attracted many researchers. Humphrey and Taber investigated the stress-modulated growth and residual stress of arteries using the concept of opening angles [92]. In their research, they speculated that vascular heterogeneity must be a result of changes in the orientation and mechanical properties of collagen fibers. In a more experimental study, Greenwald et al. measured the distribution of residual strain in the artery wall [35]. They designed two sets of experiments. In the first one they eliminated collagen and elastin by chemical methods and destroyed SMCs by freezing them. They concluded that lack of elastin increased the opening angle while the collagen fibers and SMCs had no effect. In the other experiment, they removed different layers of the arterial wall from the outer surface by lathing frozen cross sections. After thawing them they observed that the more they lathed the bigger the opening angle became. In 2005, Holzapfel et al. determined the mechanical properties of coronary artery layers

with nonatherosclerotic intimal thickening [46]. In their study, they experimented on thirteen hearts, from 3 women and 10 men which were harvested within 24 hours of death. Then they created coronary artery cross sections and cut them along the axial direction to obtain flat rectangular sheets. Thereafter, by exposing the sheets to tensile stresses, they were able to infer layer-specific mechanical parameters later used in their strain energy function. This function was able to capture the stiffening effect of collagen fibers that exist in each layer. This energy function is often called Holzapfel-Gasser-Ogden (HGO). Many researchers have used the HGO model to simulate and investigate arterial biomechanics. Olsson and Klarbring used this model to predict the residual stresses in a cylindrical artery as a result of growth and remodeling of the fiber angle [73]. They chose deviations from homeostatic pressure to be the trigger that initiates the growth. Also deviations from principle stress directions were considered as the cause of fiber remodeling.

Cardiovascular research is not limited to the arterial wall. Blood flow plays a big role in arterial biomechanics. Changes in the laminar shear stress or concentration of different chemicals inside the bloodstream are some of the crucial factors that can affect the biomechanical and histological behavior of the arteries. Study of laminar flow inside a cylindrical tube goes back to 1840 when Poiseuille proposed his famous formula [75]. After that, numerous researchers have studied the dynamics of different fluids in different vessels or the interaction between the fluid and the vessel. Some early examples are: calculating the blood flow velocity in animal arteries *in-vivo*, using an electric circuit [60] and finding an analytic solution for the flow of a viscous fluid in femoral arteries [10]. Sherwin et al. used two different discretization methods; discontinuous Galerkin and Taylor-Galerkin with different terminal boundary conditions for their 1D blood flow simulation [87]. They saw that using terminal resistance produced a dicrotic notch<sup>4</sup> which is an important feature of the pressure waveform in

---

<sup>4</sup> In the arterial pulse waveform, one pulse consists of a sharp increase corresponding to the systolic pressure, then a decline called systolic decline followed by the diastolic decrease. The transition from the systolic decline and diastolic runoff however, does not happen smoothly. There is a cusp that connects them which is known as the dicrotic notch.

the cardiac cycle. In another study, Quarteroni et al. coupled lumped and distributed models of blood flow [76]. Lumped models, are widely adopted in blood flow modeling with the help of ODEs and DAEs. One can often see the use of hydraulic or electric circuits in the literature to assist with duplicating physiologic or pathologic situations in this type of models. For example, they can divide a big cardiovascular system into smaller parts with blood flow inputs, outputs and resistances which can be modeled by electric or hydraulic circuit components. Distributed models, such as Navier-Stokes equations focus on more local phenomena. Quarteroni et al. were the first to couple these approaches, in the way that the lumped model provided estimates for the boundary conditions of the distributed model. There are many models that target the blood flow inside the heart. Peskin studied the blood flow inside the heart using a moving immersed boundary method and compared the results of natural and prosthetic valves [74]. This is an example of a fluid-structure interaction model where the blood and the blood vessel exert forces on each other. Liu and Marsden proposed a model that couples the dynamics of a viscous fluid to a hyperelastic solid in a unified computational framework [58].

In 1987, Seymour Glagov discovered an important behavior of arteries by experimenting on a section of the left main coronary artery in 136 hearts obtained at autopsy [34]. He found that arteries remodel as the plaque grows. This is done by radial enlargement (or outward remodeling) of the lumen area to compensate for growth of the plaque. This compensation will continue until the lesion reaches about 30% stenosis defined by

$$\text{Stenosis} = \frac{\text{Intima Area}}{\text{Intima Area} + \text{Lumen Area}}. \quad (1.1)$$

and then the lumen area starts shrinking (inward remodeling) as the plaque grows. Intima area in equation (1.1) is the area enclosed by the boundaries  $A$  (endothelium) and  $B$  (internal elastic lamina (IEL)) in Figure 1.1 and the denominator of (1.1) is the area enclosed by  $B$  (IEL). Stenosis is a common measurement of plaque burden in cardiovascular research.

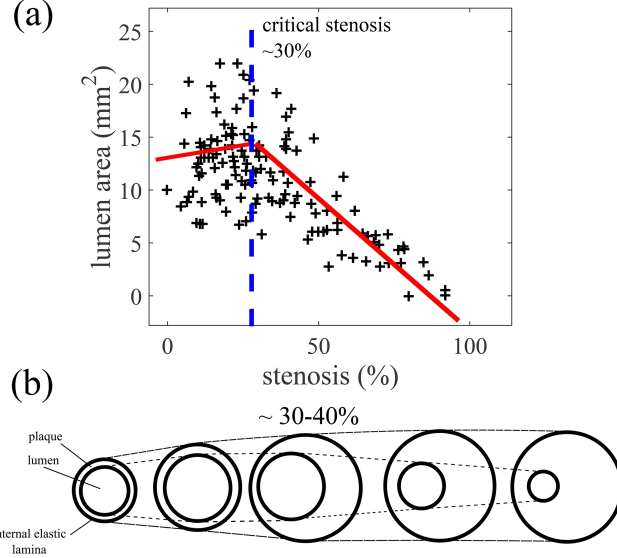


Figure 1.3: (a) Remodeling behavior depends on whether stenosis (eq. 1.1) is less than or greater than 30%. With the same data, Glagov et al. were also able to fit a piecewise linear curve with a jump in derivative at about 30% [34]. In this case, the curve gently increases when stenosis is less than 30% and decreased when the stenosis was more than 30%. (b) Schematic showing what happens to the vessel wall inferred from Glagov’s data.

Fok explored the growth in a 2D annulus subject to a uniform isotropic growth tensor [25]. Although these assumptions are not realistic, the results seem to follow the general characteristics of Glagov remodeling. In other words, it captures the compensation phase followed by an inward remodeling of the lumen at about 30% stenosis, see Figure 1.3.

Glagov phenomenon is crucial for diagnostic purposes. Since coronary angiography can only visualize the lumen, the extent of the plaque burden in the arterial wall might be underestimated during the compensation phase. In this phase, the intima-media interface, also known as internal elastic lamina (IEL), is pushed outward increasing the IEL area. This outward remodeling of IEL cannot be captured via angiography, see Figure 1.4. Therefore, understanding this attribute of the blood vessels is crucial for devising new methods for determining the severity of arterial diseases such as atherosclerosis. This phenomenon has been the subject of biological

and mathematical studies ever since [52, 53, 64, 25].

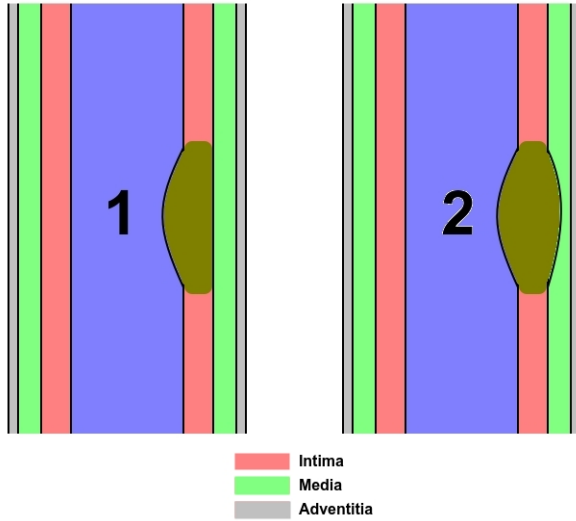


Figure 1.4: Angiography will not be able to distinguish between cases 1 and 2. However, according to formula (1.1) the stenosis in case 2 is larger than case 1.

### 1.3 Mechanical aspect and Morphoelasticity

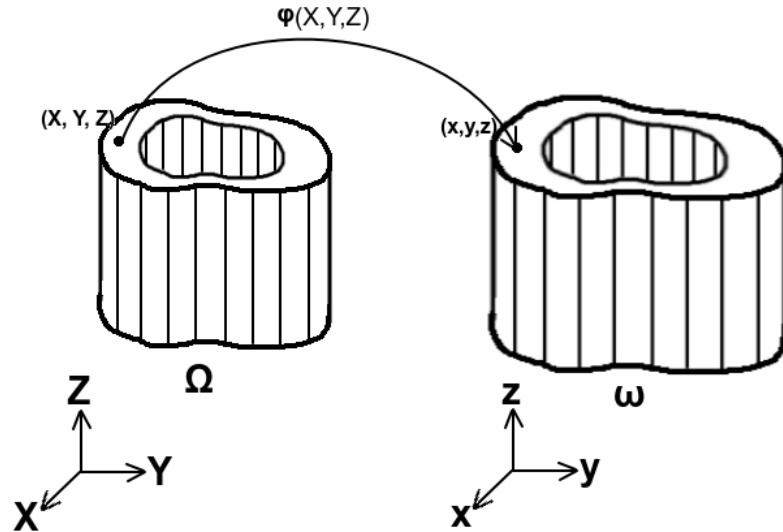


Figure 1.5: Deformation of domain  $\Omega$  via the deformation vector field  $\varphi(X, Y, Z)$ . Every point  $(X, Y, Z)$  in the reference domain gets mapped to a point in the deformed domain  $\omega$  by  $\varphi(X, Y, Z)$ .

In continuum mechanics, the deformation field  $\varphi$  is a vector field that maps every point in the reference domain to a point in the deformed domain, see Figure 1.5. We can define a displacement field  $\mathbf{u}$  corresponding to each deformation field:

$$\mathbf{u}(X, Y, Z) = \varphi(X, Y, Z) - (X, Y, Z) \quad (1.2)$$

Then the deformation of a solid is given by a tensor called the deformation gradient defined by:

$$\mathbf{F} = \nabla \varphi = \mathbf{I} + \nabla \mathbf{u} \quad (1.3)$$

where  $\mathbf{I}$  is the identity matrix.

In 1994, Rodriguez et al. proposed a mathematical framework for dealing with growth in elastic tissues [78]. This framework is what we now call morphoelasticity and has been used in many studies about growing elastic materials [84, 4, 6]. In this framework, if a tissue deformation is caused by growth the assumption is that it first undergoes a pure volumetric growth associated with a growth tensor ( $\mathbf{G}$ ) before being strained. The strain acts as an elastic response via an elastic tensor ( $\mathbf{F}_e$ ) to accommodate for the pure volumetric growth. In other words, if we consider the tissue consisting of smaller elements, first these element grow as a response to the pure growth. This might cause an “overlap” in neighboring elements which results in an incompatible configuration. The elastic response acts as a correction to accommodate the volumetric growth and creates a compatible continuous grown configuration, see Figure 1.6. This translates into the mathematical decomposition of (1.3) into the following matrix multiplication:

$$\mathbf{F} = \mathbf{F}_e \mathbf{G}. \quad (1.4)$$

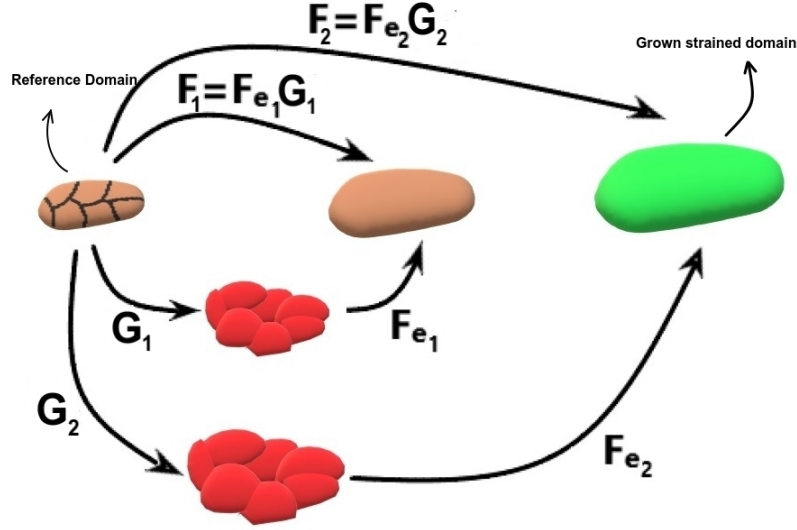


Figure 1.6: Deformation gradient decomposition based on morphoelasticity. Configurations in red are incompatible due to overlapping elements.

This treatment of deformation by growth has some limitations: 1) Morphoelasticity is not compatible with growth from a grown domain because of the non-commutativity of elastic and growth tensors. 2) Growth must happen from the reference domain and in the case of a large growth the numerical method may not converge to a solution. We elaborate on both of these issues below.

Ideally, we would want to grow from a grown domain, but this is not generally possible as we now discuss. Elastic tensors do not necessarily commute with the growth tensors which is required to get a single equation like (1.4) for morphoelasticity. The final configuration 3 (acquired by growing from the reference domain) is not in general the same as configuration 2 (acquired by growing from the grown domain 1), see Figure 1.7.

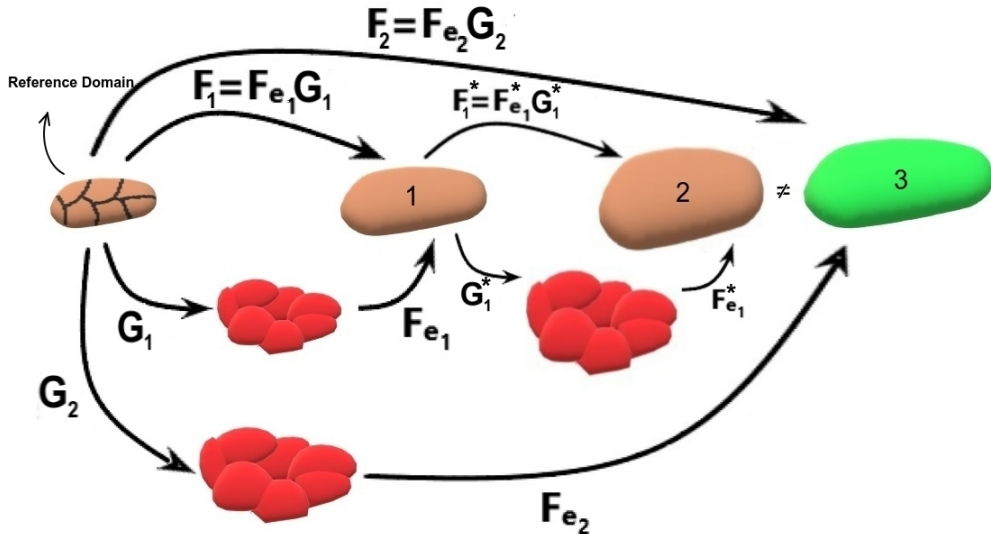


Figure 1.7: Going from the reference state to state 2 we apply  $\mathbf{F}_1^* \mathbf{F}_1 = \mathbf{F}_{e_1}^* \mathbf{G}_1^* \mathbf{F}_{e_1} \mathbf{G}_1$ . However,  $\mathbf{F}_{e_1}^*$  and  $\mathbf{G}_1$  do not necessarily commute. Therefore, in general  $\mathbf{F}_1^* \mathbf{F}_1 = \mathbf{F}_{e_1}^* \mathbf{G}_1^* \mathbf{F}_{e_1} \mathbf{G}_1$  cannot be written as  $\mathbf{F}_2 = \mathbf{F}_{e_2} \mathbf{G}_2$  which is required in the Morphoelasticity framework.

In the case when all the elastic and growth tensors are diagonal, incremental growth can be implemented. In the case that  $\mathbf{G}_1^*$  and  $\mathbf{F}_{e_1}$  do commute we will have  $\mathbf{F}_1^*\mathbf{F}_1 = \mathbf{F}_{e_1}^*\mathbf{F}_{e_1}\mathbf{G}_1^*\mathbf{G}_1$ . Therefore, by letting  $\mathbf{F}_{e_2} = \mathbf{F}_{e_1}^*\mathbf{F}_{e_1}$  and  $\mathbf{G}_2 = \mathbf{G}_1^*\mathbf{G}_1$  we get  $\mathbf{F}_1^*\mathbf{F}_1 = \mathbf{F}_2$ .

Now consider a simple problem of a growing domain in a Cartesian coordinate system with the growth tensor

$$\mathbf{G} = \text{diag}(1 + \Sigma, 1 + \Sigma, 1 + \Sigma)$$

where  $\Sigma$  is a constant. Diagonal entries correspond to growth in the  $X$ ,  $Y$  and  $Z$  direction and  $\mathbf{G} = \mathbf{I}$  corresponds to no growth. Since for finite element simulation we use Newton's method, a good initial guess is necessary. For small deformations, the reference configuration provides a good initial guess. However, in the case of a large deformation the reference configuration is not a good initial guess and can cause the numerical iteration to diverge.

A general sketch of our algorithm that gives us the deformed domain is as follows:

---

```

1: procedure
2:   Let  $\mathbf{u}_{guess} = 0$ 
3:   Let  $\Psi(\nabla u, \det(\mathbf{G}))$  be the energy of the elastic solid. (see next chapter)
4:   for  $\langle i = 1, 2, \dots, n \rangle$  do
5:     let  $G = \mathbf{I} + (i/n) * \Sigma$ 
6:     Find the displacement  $\mathbf{u}$  that makes  $\Psi(\nabla u, \det(\mathbf{G}))$  stationary for every test
      function using Newton's method and initial guess  $\mathbf{u}_{guess}$ 
7:     Let  $\mathbf{u}_{guess} = \mathbf{u}$ 
8:     Let  $i = i + 1$ 

```

---

Each of the intermediate steps (where  $i \leq n$ ) are acquired by growing from the reference domain but using the solution from the previous step as the guess ( $\mathbf{u}_{guess}$ ). Therefore, taking smaller steps improves the convergence of the Newton iteration since the next step displacement is close to  $\mathbf{u}_{guess}$  acquired from the previous step.

## 1.4 Aim of this thesis

In this thesis we use a finite element method based on morphoelasticity to study the growth of atherosclerotic plaques. The three layers of the vessel wall are modeled with HGO-type strain energy functions with different mechanical parameters. All of our numerical simulations are carried out in a FEniCS framework [55].

Although there are various studies involving arterial growth in two dimensions, anisotropic growth in 3D has not been explored in much detail. Therefore, most of our results are new and consider a three dimensional arterial domain. First we provide results that show isotropic growth is not the most energetically favorable case and produces results that are not close to Glagov's result qualitatively. On the other hand, anisotropic treatment of the problem matches Glagov's data better (Figure 1.3(a)). After establishing a method to get the most energetically favorable anisotropic growth, we investigate the effect of growth on the opening angle and the strain. Finally, we

include the biology of plaque in our model. We propose a method to couple morphoe-lastic growth in the arterial wall to the presence of a growth factor such as PDGF and we explore its effect on the histology and formation of the necrotic core.

## Chapter 2

### ATHEROSCLEROSIS MODEL IN CYLINDRICAL COORDINATES

In this chapter, we consider a three layered three dimensional axisymmetric arterial domain. As mentioned in section 1.2, morphoelasticity is our mathematical framework, and it allows us to decompose the deformation gradient  $\mathbf{F}$  into a pure growth tensor  $\mathbf{G}$  (which we prescribe) and an elastic response  $\mathbf{F}_e$  (which has to be found), as in equation (1.4).

We start with a functional that accounts for the total energy due to the volumetric deformation caused by growth and external boundary loading (blood pressure) [26]:

$$E = \underbrace{\sum_{i=1}^3 \left( \int_{\Omega_i} J_{g_i} W_i \, dV \right)}_{\text{Energy due to volumetric strain caused by growth}} + \underbrace{\frac{p}{3} \int_{\partial\Omega_1} J \mathbf{F}^{-T} \mathbf{N} \cdot \mathbf{u} \, dS}_{\text{Energy due to blood pressure}}, \quad (2.1)$$

where  $\Omega_i$  for  $i = 1, 2, 3$  corresponds to the intima, media and adventitia respectively. The boundary  $\partial\Omega_1$  is the endothelium and  $\mathbf{N}$  is its unit outward normal vector, see Figure 2.1. The vector  $\mathbf{u}$  is the displacement defined by (1.2) and  $p$  is the blood pressure. We have the following Jacobians

$$J = \det(\mathbf{F}) \quad (2.2)$$

$$J_{e_i} = \det(\mathbf{F}_{e_i}) \quad (2.3)$$

$$J_{g_i} = \det(\mathbf{G}_i). \quad (2.4)$$

Growth here is a volumetric growth that occurs only inside the intima. Therefore,  $J_{g_i} = 1$  for  $i = 2, 3$ . Deformation of the arteries causes change in strain energy  $W_i$  in

each layer. This strain energy is the sum of energy stored due to the isotropic ( $\Psi_{\text{iso}}$ ) and the anisotropic ( $\Psi_{\text{aniso}}$ ) changes in each of the layers [44]:

$$W_i = \Psi_{\text{iso}}^i + \Psi_{\text{aniso}}^i \quad (2.5)$$

$$\Psi_{\text{iso}}^i = \frac{\mu_i}{2}(I_1 - 3) + \frac{\nu}{1 - 2\nu}\mu_i(J_e - 1)^2 - \mu_i \ln J_e \quad (2.6)$$

$$\Psi_{\text{aniso}}^i = \frac{\eta_i}{\beta_i} \left\{ e^{\beta_i [\rho_i(I_4 - 1)_+^2 + (1 - \rho_i)(I_1 - 3)^2]} - 1 \right\} \quad (2.7)$$

where  $i = 1, 2, 3$  corresponds to intima, media and adventitia;  $\mu_i$ ,  $\eta_i$  are stress-like parameters; and  $\beta_i$ ,  $\rho_i$  are dimensionless. Arterial tissue is a nearly incompressible material due to its high water content. Incompressibility condition in mechanics is equivalent to  $J_e = 1$ . By taking the Poisson ratio  $\nu$  close to 0.5, we are significantly increasing the contribution of the second term in (2.6). Therefore, when minimizing the total energy (2.1) the minimization will strongly penalize  $J_e \neq 1$  which enforces the near incompressibility of the material. We also define

$$I_1 = \text{Tr}(\mathbf{C}_e) = \text{Tr}(\mathbf{F}_e^T \mathbf{F}_e) \quad (2.8)$$

$$I_4 = \mathbf{b}(R, Z)^T \mathbf{C}_e \mathbf{b}(R, Z) \quad (2.9)$$

where  $\mathbf{C}_e = \mathbf{F}_e^T \mathbf{F}_e$  is the right Cauchy-Green tensor<sup>1</sup> and  $I_1$  is its first invariant. The right Cauchy-Green tensor is a symmetric positive definite tensor. It is then independent of the frame and all of its eigenvalues are positive<sup>2</sup>. To incorporate the direction for which the collagen fibers are aligned in each of the layers we use  $\mathbf{b}(R, Z)$  which is a unit vector. The value of  $I_4$  represents the normalized length of deformed fibers ( $I_4 = 1$  means the fibers are unstretched). Because of the crimped structure of collagen it is regarded as not being able to support compressive stresses [45]. The role

<sup>1</sup> The reason it is called the right Cauchy-Green tensor is because  $\mathbf{F}_e$  is on the right side of the formula.

<sup>2</sup> The Cauchy-Green tensor for the elastic response being characterized by a positive definite tensor has a great advantage. This will prevent the material vector differentials from rotating more than 90 degrees.

of the collagen fibers is included in the  $(I_4 - 1)_+^2$  term in equation (2.7) which will be triggered only if  $I_4 > 1$ :

$$(I_4 - 1)_+^2 = \begin{cases} (I_4 - 1)^2 & \text{if } I_4 > 1 \\ 0 & \text{if } I_4 \leq 1 \end{cases} \quad (2.10)$$

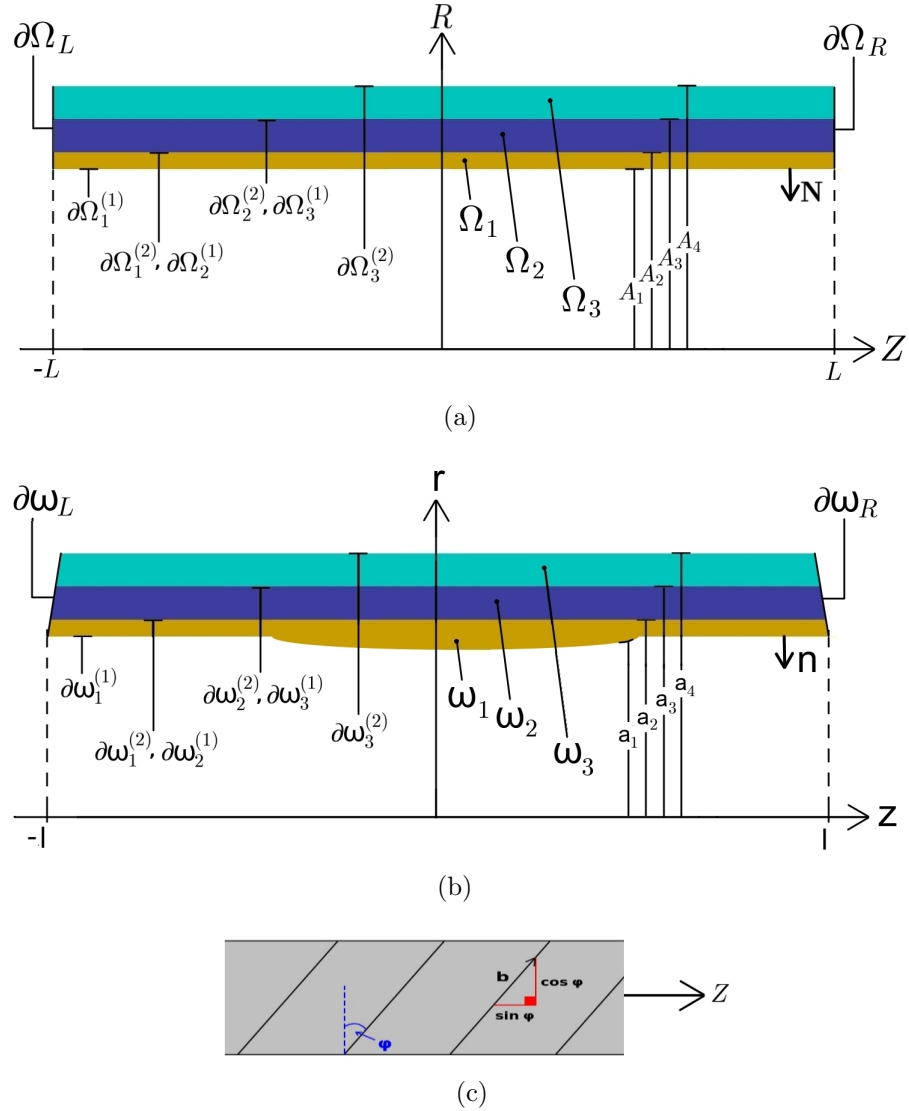


Figure 2.1: (a) Mathematical reference domain with subdomains and boundary labels. (b) Mathematical deformed domain with subdomains and boundary labels. We use lower case letters for the deformed domain. (c) Plan view of the artery and the orientation of representative fibers. Vector  $\mathbf{b}$  is defined for each layer by (2.30) and the values of  $\varphi$  for each layer are given in Table 2.1.

We are interested in finding a solution to the following boundary value problem

$$\nabla \cdot \boldsymbol{\sigma} = -\hat{\mathbf{f}}, \quad \text{on } \omega \quad (2.11)$$

$$\boldsymbol{\sigma}\mathbf{n} = -p\mathbf{n}, \quad \text{on } \partial\omega_1^{(1)} \quad (2.12)$$

$$\boldsymbol{\sigma}\mathbf{n} = 0, \quad \text{on } \partial\omega_3^{(2)} \quad (2.13)$$

$$\boldsymbol{\sigma}\mathbf{n}|_{\partial\omega_1^{(2)}} + \boldsymbol{\sigma}\mathbf{n}|_{\partial\omega_2^{(1)}} = 0, \quad (2.14)$$

$$\boldsymbol{\sigma}\mathbf{n}|_{\partial\omega_2^{(2)}} + \boldsymbol{\sigma}\mathbf{n}|_{\partial\omega_3^{(1)}} = 0. \quad (2.15)$$

where the tensor  $\boldsymbol{\sigma}$  is the Cauchy stress tensor,  $\hat{\mathbf{f}}$  is the body force,  $\omega = \bigcup_{i=1}^3 \omega_i$  for  $i = 1, 2, 3$  is the three layered domain after deformation and  $\partial\omega_i^{(1)}$  is the inner boundary and  $\partial\omega_i^{(2)}$  is the outer boundary of the  $i$ -th layer after the deformation. We consider  $p$  to be the only boundary load, which in our case is the blood pressure. We denote the outward unit normal vector to the deformed boundary by  $\mathbf{n}$ , see Figure 2.1(b). Given that stenotic coronary arteries generally experience very little axial pre-stretch [29, 85] we add two traction free boundary conditions for the end surfaces

$$\boldsymbol{\sigma}\mathbf{n} = 0, \quad \text{on } \partial\omega_L \quad (2.16)$$

$$\boldsymbol{\sigma}\mathbf{n} = 0. \quad \text{on } \partial\omega_R \quad (2.17)$$

Even though (2.11)-(2.17) seem like a typical boundary value problem, since morphoeelasticity is not compatible with growth from a grown domain (refer to section 1.3), we prefer working with the reference domain,  $\Omega$ . Thus, we use a system that utilizes  $\partial\Omega$  for its boundary condition rather than  $\partial\omega$ , see Figure 2.1(a). Therefore, by applying Nanson's pull back formula [44] and using the first Piola-Kirchoff stress tensor, (2.11)-(2.17) turn into

$$\nabla \cdot \mathbf{T} = -\mathbf{f}, \quad \text{on } \Omega_1, \Omega_2, \Omega_3 \quad (2.18)$$

$$\mathbf{T}\mathbf{N} = -pJ\mathbf{F}^{-T}\mathbf{N}, \quad \text{on } \partial\Omega_1^{(1)} \quad (2.19)$$

$$\mathbf{T}\mathbf{N} = 0, \quad \text{on } \partial\Omega_3^{(2)} \quad (2.20)$$

$$\mathbf{T}\mathbf{N}|_{\partial\Omega_1^{(2)}} + \mathbf{T}\mathbf{N}|_{\partial\Omega_2^{(1)}} = 0, \quad (2.21)$$

$$\mathbf{T}\mathbf{N}|_{\partial\Omega_2^{(2)}} + \mathbf{T}\mathbf{N}|_{\partial\Omega_3^{(1)}} = 0, \quad (2.22)$$

$$\mathbf{T}\mathbf{N} = 0, \quad \text{on } \partial\Omega_L \quad (2.23)$$

$$\mathbf{T}\mathbf{N} = 0, \quad \text{on } \partial\Omega_R \quad (2.24)$$

where the first Piola-Kirchoff stress is

$$\mathbf{T} = J_g \frac{\partial W}{\partial \mathbf{F}_e} \mathbf{G}^{-T}, \quad (2.25)$$

see [1, 102]. Also  $\mathbf{f}(X, Y, Z) = J\hat{\mathbf{f}}$  [38] and  $\mathbf{N}$  is the outward unit normal vector to the reference boundary, see Figure 2.1(a). For solving this problem we use a weak form that is equivalent to (2.18)-(2.24).

## 2.1 Weak formulation in cylindrical coordinates

In this chapter, we consider an axisymmetric cylindrical domain  $\Omega$  with three subdomains  $\Omega_i$  for  $i = 1, 2, 3$  to represent the artery. Let  $R$ ,  $\Theta$  and  $Z$  be the radius, polar angle and axial distance of a point in the reference domain in cylindrical coordinates and  $r, \theta$  and  $z$  be the corresponding quantities in the deformed domain. We consider  $(R, \Theta, Z)$  as a generic point in the reference domain and  $(r, \theta, z)$  as the one in the deformed domain. Suppose  $\varphi$  is the deformation field that maps the reference domain into the deformed domain and  $\mathbf{u}$  is the corresponding displacement field given in (1.2). Then, from equation (1.3), the deformation gradient is

$$\mathbf{F} = \mathbf{I} + \nabla \mathbf{u} \quad (2.26)$$

where

$$\mathbf{F} = \begin{bmatrix} \frac{\partial r}{\partial R} & \frac{1}{R} \frac{\partial r}{\partial \Theta} & \frac{\partial r}{\partial Z} \\ r \frac{\partial \theta}{\partial R} & r \frac{\partial \theta}{\partial \Theta} & r \frac{\partial \theta}{\partial Z} \\ \frac{\partial z}{\partial R} & \frac{\partial z}{\partial \Theta} & \frac{\partial z}{\partial Z} \end{bmatrix} \quad (2.27)$$

However, in the axisymmetric case  $r$  and  $z$  are independent of  $\Theta$  and  $\theta$  is independent of  $R$  and  $Z$ , which simplifies the deformation gradient into

$$\mathbf{F} = \begin{bmatrix} \frac{\partial r}{\partial R} & 0 & \frac{\partial r}{\partial Z} \\ 0 & \frac{r}{R} & 0 \\ \frac{\partial z}{\partial R} & 0 & \frac{\partial z}{\partial Z} \end{bmatrix} \quad (2.28)$$

hence

$$J = \det(\mathbf{F}) = \frac{r}{R} \left( \frac{\partial r}{\partial R} \frac{\partial z}{\partial Z} - \frac{\partial r}{\partial Z} \frac{\partial z}{\partial R} \right) \quad (2.29)$$

The fiber direction vectors in each undeformed layer take the form

$$\mathbf{b}_i(R, Z) = \cos(\varphi_i) \hat{\mathbf{e}}_\Theta + \sin(\varphi_i) \hat{\mathbf{e}}_Z \quad (2.30)$$

where  $i = 1, 2, 3$  corresponds to intima, media and adventitia and  $\varphi_i$  is the angle from Figure 2.1(c) for each layer. Also  $\hat{\mathbf{e}}_\Theta$  and  $\hat{\mathbf{e}}_Z$  are the circumferential and axial basis vectors in the reference configuration. Furthermore,  $\mathbf{T}_i = J_{g_i} \frac{\partial W_i}{\partial \mathbf{F}_{e_i}} \mathbf{G}_i^{-T}$  for  $i = 1, 2, 3$ .

Using (2.5)-(2.9) and (2.29)-(2.30) we have:

$$\begin{aligned} \frac{\partial W_i}{\partial \mathbf{F}_{e_i}} &= \mu_i \mathbf{F}_{e_i} + \frac{2\mu_i \nu (J_{e_i} - 1) J_{e_i}}{1 - 2\nu} \mathbf{F}_{e_i}^{-T} - \mu_i \mathbf{F}_{e_i}^{-T} \\ &+ 4\eta_i \left\{ \rho_i \mathbf{F}_{e_i} \mathbf{b}_i \mathbf{b}_i^T (I_4 - 1)_+ + (1 - \rho_i) \mathbf{F}_{e_i} (I_1 - 3) \right\} e^{\beta_i [\rho_i (I_4 - 1)_+^2 + (1 - \rho_i) (I_1 - 3)^2]} \end{aligned} \quad (2.31)$$

The biology of our problem suggests that the growth occurs only inside the intima. Therefore,  $\mathbf{G}_i = \mathbf{I}$  and  $J_{g_i} = 1$  when  $i = 2, 3$  (in the media and adventitia). On the other hand we consider  $\mathbf{G}_1 = \text{diag}(g_\alpha(t, Z), g_\beta(t, Z), g_\gamma(t, Z))$  with

$$g_\alpha(t, Z) = 1 + \alpha t \exp(-aZ^2) \quad (2.32)$$

$$g_\beta(t, Z) = 1 + \beta t \exp(-aZ^2) \quad (2.33)$$

$$g_\gamma(t, Z) = 1 + \gamma t \exp(-aZ^2) \quad (2.34)$$

corresponding to radial, circumferential and axial growth respectively. The variable  $t$  is time which is in years throughout this chapter. We include the exponential functions in  $Z$  to model the effect of local growth in the axial direction. Furthermore, we want growth to increase linearly in time but at different rates and this is the reason for including  $\alpha, \beta$  and  $\gamma$ . In other words, these parameters  $\alpha, \beta$  and  $\gamma$  allow us to explore the effect of anisotropic growth on Glagov remodeling and in the case of isotropic growth we will have  $\alpha = \beta = \gamma$ . The parameter  $a$  determines the locality of growth. We denote the radii of the boundaries between the lumen, intima, media, adventitia and the external tissue in the reference domain by  $A_1, A_2, A_3$  and  $A_4$  respectively. Also the value  $L$  specifies the half-length of the artery cross section such that  $-L < Z < L$ . See Table 2.1. We are now ready to propose a weak form for (2.18)-(2.24).

**Theorem 1.** Suppose a constant pressure load  $p$  is applied to the inner boundary  $\partial\Omega_1^{(1)}$  of a three layered arterial domain  $\Omega = \bigcup_{i=1}^3 \Omega_i$  with piecewise smooth boundaries. For simplicity we denote the outward unit normal vectors  $\mathbf{N}|_{\partial\Omega_i^{(k)}}, \mathbf{N}|_{\partial\Omega_L}$  and  $\mathbf{N}|_{\partial\Omega_R}$  by  $\mathbf{N}_i^{(k)}, \mathbf{N}_L$  and  $\mathbf{N}_R$  for  $i = 1, 2, 3$  and  $k = 1, 2$ , respectively. Assume that the domain has a finite length  $2L$  and is traction free at both ends and  $\mathbf{f} \in L^2(\Omega)$  and  $\mathbf{G}_i$  for  $i = 1, 2, 3$  are growth tensors defined on the intima, media and adventitia respectively. Then defining  $J_{g_i} = \det(\mathbf{G}_i)$ , the displacement field  $\mathbf{u} \in C^2(\Omega)$  that solves (2.18)-(2.24) also satisfies

$$2\pi \sum_{i=1}^3 \int_{-L}^L \int_{A_i}^{A_{i+1}} \left[ \left( J_{g_i} \frac{\partial W_i}{\partial \mathbf{F}_{e_i}} \mathbf{G}_i^{-T} : \nabla \mathbf{v} \right) - \mathbf{f} \cdot \mathbf{v} \right] R \, dR \, dZ + 2\pi p A_1 \left( \int_{-L}^L J \mathbf{F}^{-T} \mathbf{N}_1^{(1)} \cdot \mathbf{v} \, dZ \right) = 0 \quad (2.35)$$

for every  $\mathbf{v} \in C^2(\Omega)$ , where  $\frac{\partial W_i}{\partial \mathbf{F}_{e_i}}$  is defined in (2.31),  $J$  is defined in (2.29) and  $\mathbf{F}$  is defined by (2.26) and (2.28).

*Proof.* Let  $\mathbf{v} \in C^2(\Omega)$ . By multiplying both sides of (2.18)-(2.24) by  $\mathbf{v}$  and integrating

over their respective domains we get the following

$$\int_{\Omega} (\nabla \cdot \mathbf{T}) \cdot \mathbf{v} d\mathbf{x} = - \int_{\Omega} \mathbf{f} \cdot \mathbf{v} d\mathbf{x}, \quad (\text{I})$$

$$\int_{\partial\Omega_1^{(1)}} \mathbf{T}\mathbf{N}_1^{(1)} \cdot \mathbf{v} ds = - \int_{\partial\Omega_1^{(1)}} pJ\mathbf{F}^{-T} \mathbf{N}_1^{(1)} \cdot \mathbf{v} ds, \quad (\text{II})$$

$$\int_{\partial\Omega_3^{(2)}} \mathbf{T}\mathbf{N}_3^{(2)} \cdot \mathbf{v} ds = 0, \quad (\text{III})$$

$$\int_{\partial\Omega_1^{(2)}} \mathbf{T}\mathbf{N}_1^{(2)} \cdot \mathbf{v} ds + \int_{\partial\Omega_2^{(1)}} \mathbf{T}\mathbf{N}_2^{(1)} \cdot \mathbf{v} ds = 0, \quad (\text{IV})$$

$$\int_{\partial\Omega_2^{(2)}} \mathbf{T}\mathbf{N}_2^{(2)} \cdot \mathbf{v} ds + \int_{\partial\Omega_3^{(1)}} \mathbf{T}\mathbf{N}_3^{(1)} \cdot \mathbf{v} ds = 0, \quad (\text{V})$$

$$\int_{\partial\Omega_L} \mathbf{T}\mathbf{N}_L \cdot \mathbf{v} ds = 0, \quad (\text{VI})$$

$$\int_{\partial\Omega_R} \mathbf{T}\mathbf{N}_R \cdot \mathbf{v} ds = 0. \quad (\text{VII})$$

Adding equations (I)-(VII) and using  $\Omega = \bigcup_{i=1}^3 \Omega_i$  gives us

$$\begin{aligned} & - \sum_{i=1}^3 \left[ \int_{\Omega_i} (\nabla \cdot \mathbf{T}_i) \cdot \mathbf{v} d\mathbf{x} \right] - \int_{\Omega} \mathbf{f} \cdot \mathbf{v} d\mathbf{x} + \int_{\partial\Omega_1^{(1)}} pJ\mathbf{F}^{-T} \mathbf{N}_1^{(1)} \cdot \mathbf{v} d\mathbf{x} + \int_{\partial\Omega_1^{(1)}} \mathbf{T}\mathbf{N}_1^{(1)} \cdot \mathbf{v} ds \\ & + \int_{\partial\Omega_2^{(1)}} \mathbf{T}\mathbf{N}_2^{(1)} \cdot \mathbf{v} ds + \int_{\partial\Omega_3^{(1)}} \mathbf{T}\mathbf{N}_3^{(1)} \cdot \mathbf{v} ds + \int_{\partial\Omega_1^{(2)}} \mathbf{T}\mathbf{N}_1^{(2)} \cdot \mathbf{v} ds + \int_{\partial\Omega_2^{(2)}} \mathbf{T}\mathbf{N}_2^{(2)} \cdot \mathbf{v} ds \\ & + \int_{\partial\Omega_3^{(2)}} \mathbf{T}\mathbf{N}_3^{(2)} \cdot \mathbf{v} ds + \int_{\partial\Omega_L} \mathbf{T}\mathbf{N}_L \cdot \mathbf{v} ds + \int_{\partial\Omega_R} \mathbf{T}\mathbf{N}_R \cdot \mathbf{v} ds = 0. \end{aligned} \quad (2.36)$$

Now using the divergence theorem on the sum results in

$$\begin{aligned} & - \sum_{i=1}^3 \left[ \int_{\Omega_i} (\nabla \cdot \mathbf{T}_i) \cdot \mathbf{v} d\mathbf{x} \right] = \sum_{i=1}^3 \left[ \int_{\Omega_i} (\mathbf{T}_i : \nabla \mathbf{v}) d\mathbf{x} \right] - \int_{\partial\Omega_1^{(1)}} \mathbf{T}\mathbf{N}_1^{(1)} \cdot \mathbf{v} ds - \int_{\partial\Omega_2^{(1)}} \mathbf{T}\mathbf{N}_2^{(1)} \cdot \mathbf{v} ds \\ & - \int_{\partial\Omega_3^{(1)}} \mathbf{T}\mathbf{N}_3^{(1)} \cdot \mathbf{v} ds - \int_{\partial\Omega_1^{(2)}} \mathbf{T}\mathbf{N}_1^{(2)} \cdot \mathbf{v} ds - \int_{\partial\Omega_2^{(2)}} \mathbf{T}\mathbf{N}_2^{(2)} \cdot \mathbf{v} ds \\ & - \int_{\partial\Omega_3^{(2)}} \mathbf{T}\mathbf{N}_3^{(2)} \cdot \mathbf{v} ds - \int_{\partial\Omega_L} \mathbf{T}\mathbf{N}_L \cdot \mathbf{v} ds - \int_{\partial\Omega_R} \mathbf{T}\mathbf{N}_R \cdot \mathbf{v} ds. \end{aligned} \quad (2.37)$$

Then we replace (2.37) in (2.36) to get

$$\sum_{i=1}^3 \left[ \int_{\Omega_i} (\mathbf{T}_i : \nabla \mathbf{v}) d\mathbf{x} \right] - \int_{\Omega} \mathbf{f} \cdot \mathbf{v} d\mathbf{x} + \int_{\partial\Omega_1^{(1)}} p J \mathbf{F}^{-T} \mathbf{N} \cdot \mathbf{v} ds = 0. \quad (2.38)$$

Finally, we switch to cylindrical coordinates

$$2\pi \sum_{i=1}^3 \left[ \int_{-L}^L \int_{A_i}^{A_{i+1}} [(\mathbf{T}_i : \nabla \mathbf{v}) - \mathbf{f} \cdot \mathbf{v}] R dR dZ \right] + 2\pi \left( \int_{-L}^L p J \mathbf{F}^{-T} \mathbf{N} \cdot \mathbf{v} R dZ \right) \Big|_{R=A_1} = 0.$$

Notice that since there is no dependence on  $\Theta$  due to axisymmetry we have integrated with respect to  $\Theta$  producing the  $2\pi$  coefficients. Using the definition  $\mathbf{T}_i = J_{g_i} \frac{\partial W_i}{\partial \mathbf{F}_{e_i}} \mathbf{G}_i^{-T}$  we get (2.35) for every  $\mathbf{v} \in C^2(\Omega)$ .  $\square$

**Note:** In this thesis, we assume that the body forces are negligible. Therefore, (2.35) becomes

$$2\pi \sum_{i=1}^3 \int_{-L}^L \int_{A_i}^{A_{i+1}} \left( J_{g_i} \frac{\partial W_i}{\partial \mathbf{F}_{e_i}} \mathbf{G}_i^{-T} : \nabla \mathbf{v} \right) R dR dZ + 2\pi \left( p \int_{-L}^L J \mathbf{F}^{-T} \mathbf{N} \cdot \mathbf{v} R dZ \right) \Big|_{R=A_1} = 0 \quad (2.39)$$

for every  $\mathbf{v} \in C^2(\Omega)$ .

We use Table 2.1 for parameter values. All the values are proposed by [46] as a result of experimenting on 13 hearts from 3 women and 10 men post mortem.

Symbol	Units	Value
$\mu_1$	kPa	27.9
$\mu_2$	kPa	1.27
$\mu_3$	kPa	7.56
$\nu$	Dimensionless	0.49
$\eta_1$	kPa	263.66
$\eta_2$	kPa	21.60
$\eta_3$	kPa	38.57
$\beta_1$	Dimensionless	170.88
$\beta_2$	Dimensionless	8.21
$\beta_3$	Dimensionless	85.03
$\rho_1$	Dimensionless	0.51
$\rho_2$	Dimensionless	0.25
$\rho_3$	Dimensionless	0.55
$\varphi_1$	Degrees	60.3
$\varphi_2$	Degrees	20.61
$\varphi_3$	Degrees	67
$A_1$	mm	1.26
$A_2$	mm	1.47
$A_3$	mm	1.89
$A_4$	mm	2.31
$L$	cm	3.36

Table 2.1: List of parameter values used in this thesis.

Ultimately, we need to find a displacement field  $\mathbf{u}$  that gives us a deformation gradient  $\mathbf{F}$  in (2.26) and (2.28) which gives us the elastic tensors  $\mathbf{F}_{e_i} = \mathbf{F}\mathbf{G}^{-1}$  for each layer by (1.4) which leads to the first Piola-Kirchoff stress tensors  $\mathbf{T}_i$  for each layer that satisfies (2.39) for sufficiently smooth  $\mathbf{v}$ .

We use FEniCS as our computing platform for finite element simulations in this thesis. FEniCS is a powerful open source package that can be utilized by languages such as C++ and Python [55]. For this problem, we use a 2D mesh in  $(R, Z)$  with about 11000 triangles, see Fig 2.2. In our codes, we use a nonlinear Newton solver which uses a GMRES linear solver with an incomplete LU preconditioner for each iteration. A relative and absolute error of  $10^{-9}$  is defined for all of the codes used in this thesis.

Shear locking is a phenomenon in finite element simulation that is caused due to the use of linear elements. The linear elements are unable to capture the curvature caused by bending. These kinds of elements increase the effective stiffness of the problem. In other words, the simulation ends up with less displacement than it should. We believe that in some cases the growth in the intima can impose a weak bending effect on the media which might lead to shear locking. Therefore, to be safe we used quadratic elements. This is a common remedy for shear locking. This way, we approximate the displacement field by second order Lagrangian elements which leads to a linear approximation for the strain. Also increasing the number of elements along the thickness of the domain is another common remedy for shear locking [103].

Although the problem is computationally intensive, the University of Delaware's Caviness cluster was able to find solutions in about 12 hours. Caviness is a distributed-memory linux cluster with 126 compute nodes (4536 cores, 24.6 TB memory) and a Lustre storage of approximately 200 TiB of usable space. Thanks to access to a high performance computing resource, we were able to simulate growth for values of  $t$  as large as 3 decades in (2.32)-(2.34).

In the special case where  $\eta = 0$  in (2.6) for each layer, validation was done by comparing the results of our Fenics code with a 1D solution (solved using Matlab), see the appendix in [26].

## 2.2 Assumptions

For the rest of this chapter, we consider the blood pressure to be the average value between systolic and diastolic blood pressure with  $p = 16 \text{ kPa} = 120 \text{ mmHg}$ . Atherosclerosis is always associated with hypertension and our choice is equivalent to hypertension stage II blood pressure according to the American Heart Association, see Table 2.2. We assume that the artery is in the pressurized state at  $t = 0$ , see Figure 2.2. The blood pressure causes the vessel to dilate and the length of the artery decreases to conserve volume. Signs of coronary artery disease rarely occur in young adults (age  $< 40$ ) [93] and stenosis larger than 50% is often observed in adults older than 60 [33]. Therefore, we assume in our model atherosclerosis starts around age 35 and continues until 65, and we run our simulations from  $t = 0$  to  $t = 30$  years accordingly.

Blood pressure category	Systolic (mm Hg)	Diastolic (mm Hg)
Normal	$< 120$	$< 80$
Elevated	$120 - 129$	$< 80$
High blood pressure (Hypertension) Stage I	$130 - 139$	$80 - 89$
High blood pressure (Hypertension) Stage II	$\geq 140$	$\geq 90$
Hypertensive crisis	$\geq 180$	$\geq 120$

Table 2.2: Blood pressure category by American Heart Association.

## 2.3 The effect of pure growth in each direction

First we start with investigating the effect of pure growth in each of the radial, circumferential and axial directions. We can roughly see in Figure 2.3 the effect of such growth. We believe that their different behaviors will give insight on how each component of the growth tensor contributes to the overall process of remodeling. We

provide graphs such as lumen area as a function of stenosis and lumen area as a function of time using the spatially dependent version of (1.1):

$$\text{Stenosis}(Z) = \frac{\text{Intima Area}(Z)}{\text{Intima Area}(Z) + \text{Lumen Area}(Z)} \quad (2.40)$$

where  $\text{Stenosis}(Z)$ ,  $\text{Intima Area}(Z)$  and  $\text{Lumen Area}(Z)$  correspond to the stenosis, intima area and lumen area at axial position  $Z$  respectively. In addition, we explore changes in the fiber angles and total energy.

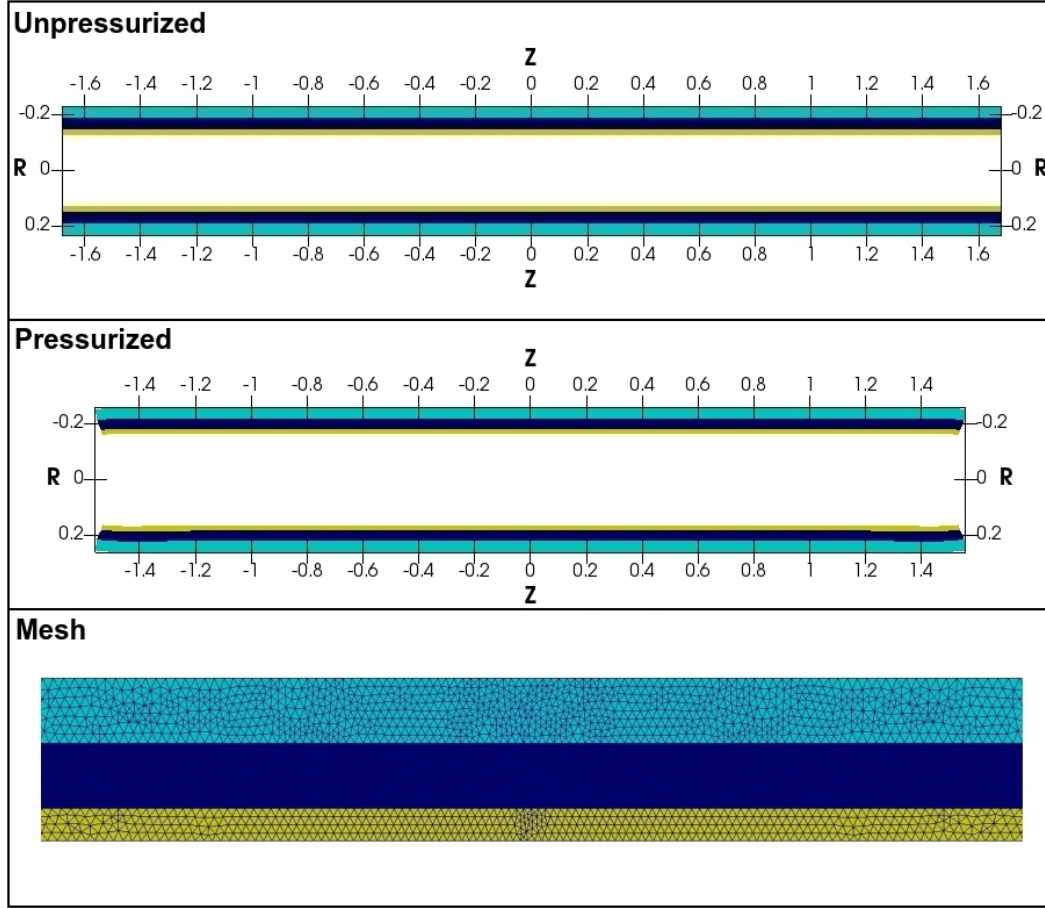


Figure 2.2: *Top*: The unpressurized reference domain. *Middle*: The reference domain after applying the blood pressure of 16 kPa. *Bottom*: Mesh sample for  $-0.58 \leq Z \leq 0.58$ . Mesh is denser where growth is larger.

### 2.3.1 Pure radial growth

Let us assume that the intima grows according to the growth tensor  $\mathbf{G}_\alpha = \text{diag}(g_\alpha(t, Z), 1, 1)$ . This means that the intima grows radially by  $g_\alpha(t, Z)$  from (2.32)

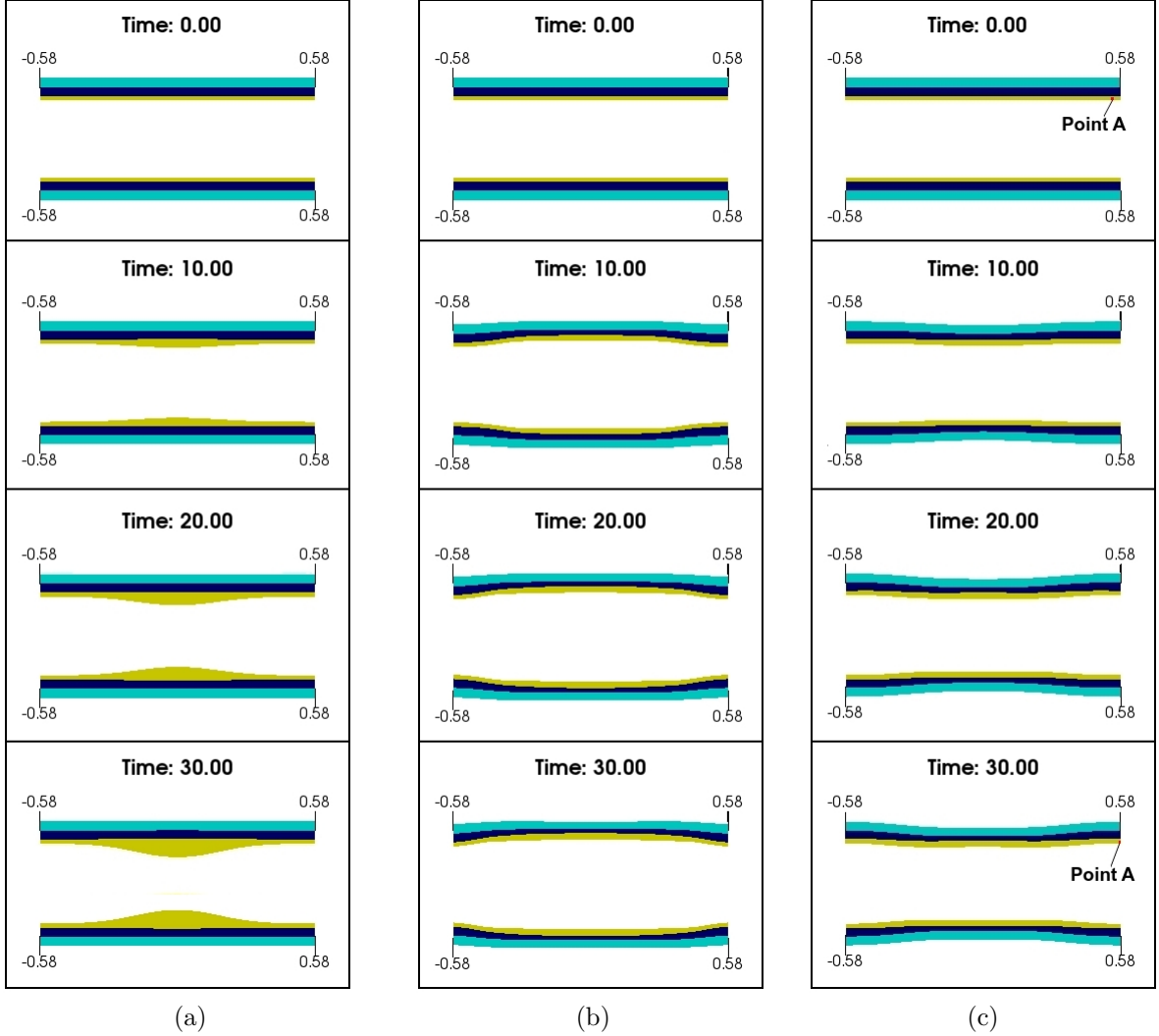


Figure 2.3: Evolution of the domain for  $-0.58 \leq Z \leq 0.58$  subject to (a) pure radial growth with  $(\alpha, \beta, \gamma) = (1, 0, 0)$ , (b) pure circumferential growth with  $(\alpha, \beta, \gamma) = (0, 1, 0)$  and (c) pure axial growth with  $(\alpha, \beta, \gamma) = (0, 0, 1)$ . The material point at A moves to the right under the effect of axial growth. Parameter  $a$  in (2.32)-(2.34) is taken to be 14.29.

and there is no growth in the circumferential and radial direction.

According to Figure 2.3(a), the radial growth almost exclusively contributes to inward thickening of the intima. As expected, the inward remodeling is greater when closer to the center of growth  $Z = 0$  and consequently the artery undergoes more stenosis there, see Figure 2.4. We refrained from including more cross sections since far away from  $Z = 0$  the growth function has little to no effect and therefore the lumen area stays the same. We will also see that pure radial growth does not greatly affect the total energy, see section 2.4.

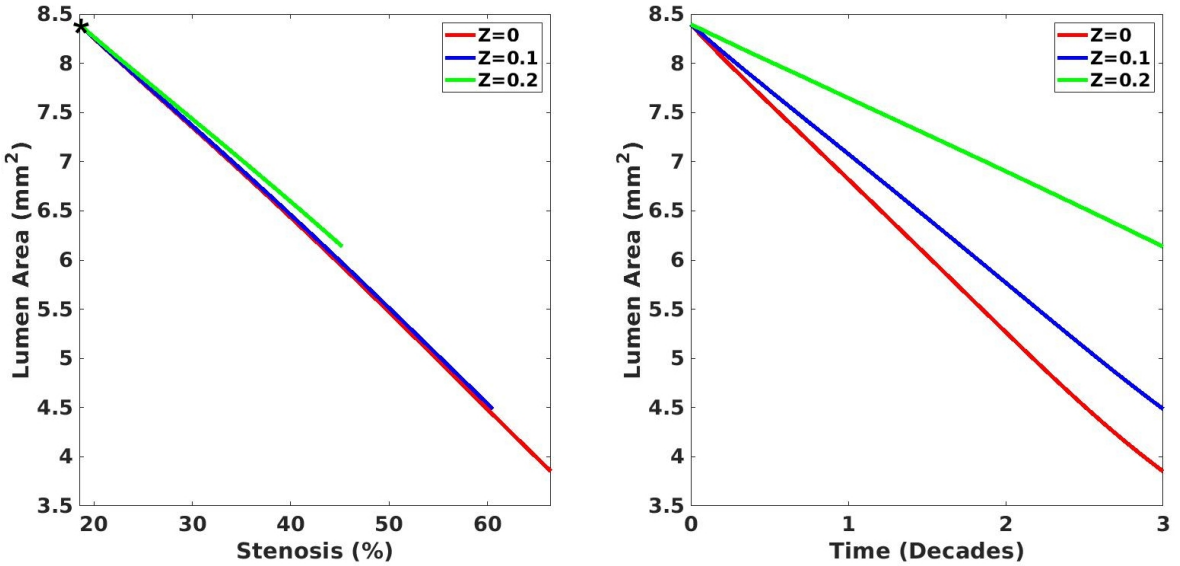


Figure 2.4: *Left:* Lumen area against stenosis. Star denotes the time  $t = 0$ . *Right:* Lumen area in time. With pure radial growth close to the center of growth  $Z = 0$  the remodeling is strictly inward.

### 2.3.2 Pure circumferential growth

Now we assume that growth is purely in the circumferential direction. Therefore the growth tensor takes the form  $\mathbf{G}_\beta = \text{diag}(1, g_\beta(t, Z), 1)$ .

According to Figure 2.3(b), pure circumferential growth mostly contributes to the outward remodeling of the vessel. There is a slight intimal thickening and increase in stenosis but compared to the radial growth it is negligible, see Figure 2.5. Also one can see that the lumen area plateaus in Figure 2.5 for large  $t$  which may be due to

the effect of stiffening collagen fibers. The intima slightly thickens in this case which explains the oscillation in Figure 2.5.

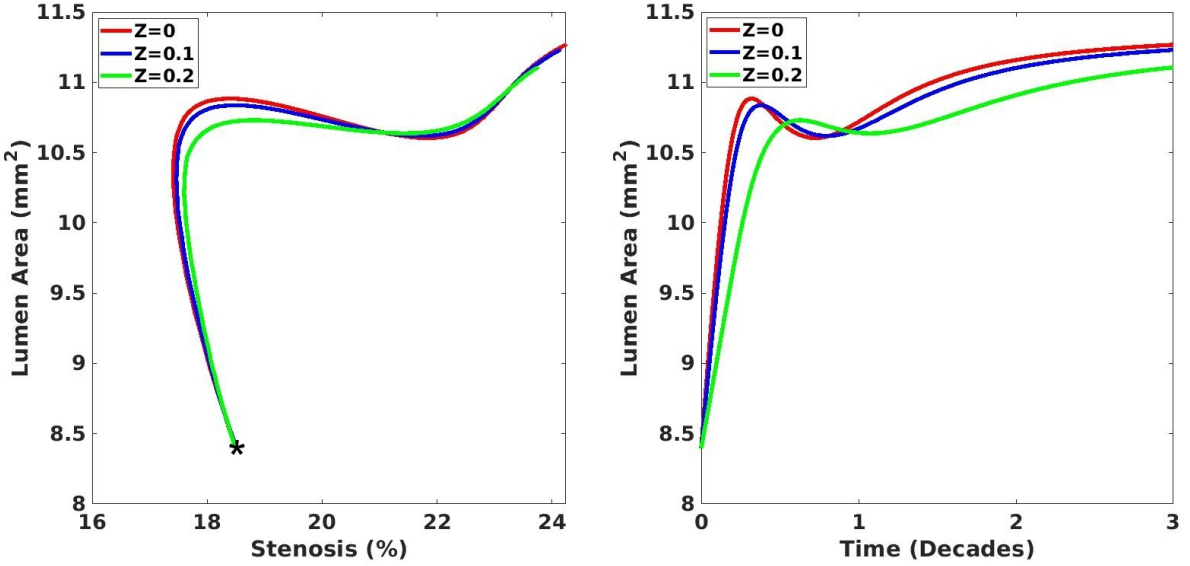


Figure 2.5: *Left:* Lumen area against stenosis. Star denotes the time  $t = 0$ . *Right:* Lumen area in time. With pure circumferential growth close to the center of growth  $Z = 0$  the remodeling is mostly outward.

### 2.3.3 Pure axial growth

Finally, we do the same investigation when growth is purely in the axial direction. Therefore, we take the growth tensor to be  $\mathbf{G}_\gamma = \text{diag}(1, 1, g_\gamma(t, Z))$ .

Pure axial growth mainly contributes to axial elongation, see Figure 2.3(c). We see a short outward remodeling followed by a significant inward remodeling for this type of growth, see Figure 2.6. However, unlike the pure radial growth, remodeling is not exclusively a result of intimal thickening. As one can see in Figure 2.3(c), the intima thickness is not significant but we can see a mild inward buckling of the arterial wall which reduces the lumen area.

We have seen the effects of growth in the radial, circumferential and axial directions. Now we explore the energy change associated with each of these growth modes.

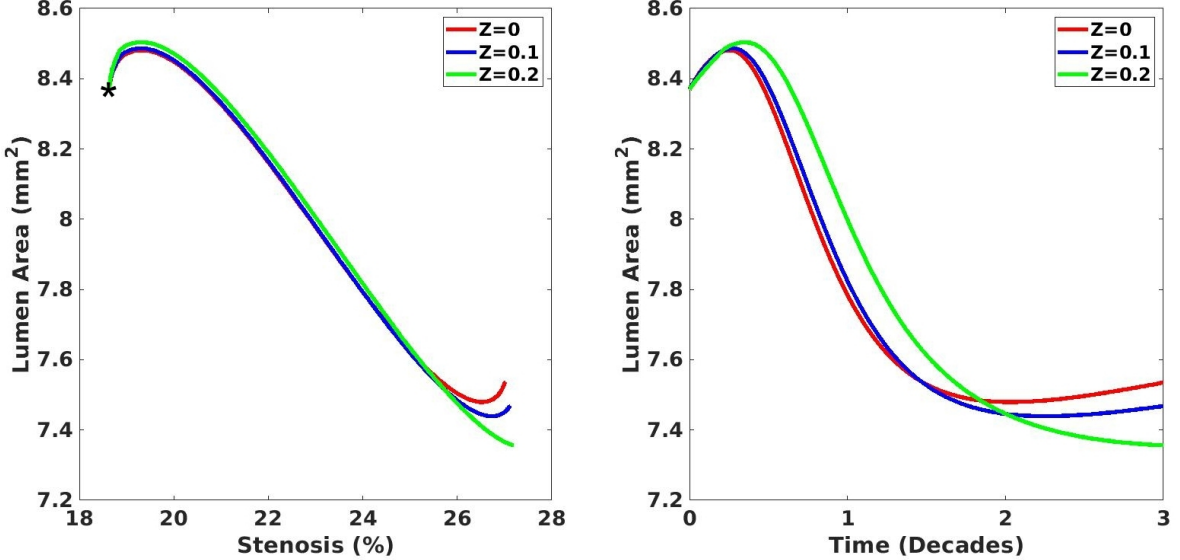


Figure 2.6: *Left:* Lumen area against stenosis. Star denotes the time  $t = 0$ . *Right:* Lumen area in time. With pure axial growth close to the center of growth  $Z = 0$  the remodeling is mostly outward with no significant increase in stenosis.

## 2.4 Growth and energy change

In this section, we are interested in calculating the energy change in the artery due to each growth direction. We want to see which growth direction is more energetically favorable. We revisit the equation (2.1) but in cylindrical coordinates

$$E = \underbrace{2\pi \sum_{i=1}^3 \int_{-L}^L \int_{A_i}^{A_{i+1}} J_{g_i} W_i R dR dZ}_{\text{Energy due to volumetric strain caused by growth}} + \underbrace{2\pi A_1 \frac{p}{3} \int_{-L}^L J \mathbf{F}^{-T} \mathbf{N}_1^{(1)} \cdot \mathbf{u} dZ}_{\text{Energy due to blood pressure}}. \quad (2.41)$$

In Theorem 1, we showed how to derive the variational form (2.35) from the strong forms (2.18)-(2.24). The following theorem establishes a relationship between the variational form (2.35) and the energy functional (2.41).

**Theorem 2.** *The displacement field  $\mathbf{u} \in C^2(\Omega)$  that satisfies the weak equation*

$$2\pi \sum_{i=1}^3 \int_{-L}^L \int_{A_i}^{A_{i+1}} \left( J_{g_i} \frac{\partial W_i}{\partial \mathbf{F}_{e_i}} \mathbf{G}_i^{-T} : \nabla \mathbf{v} \right) R dR dZ + 2\pi p A_1 \left( \int_{-L}^L J \mathbf{F}^{-T} \mathbf{N}_1^{(1)} \cdot \mathbf{v} dZ \right) = 0 \quad (2.42)$$

for every  $\mathbf{v} \in C^2(\Omega)$  also makes (2.41) stationary. Note that equation (2.42) is just equation (2.35) in the special case when  $\mathbf{f} = 0$ .

*Proof.* For a proof refer to [26].  $\square$

Now to observe the change in energy purely imposed by growth in each direction, we compute the total energy (2.41) for the three cases in sections 3.1.1, 3.1.2 and 3.1.3. The result is shown in Figure 2.7. We extract the energies induced by each growth direction at times  $t = 5, 10, 15, 20, 25, 30$  from Figure 2.7, and show them in Table 2.3 Assuming that intima growth stems from cell division, the amount of energy needed for the cells to divide in the radial direction is much less than the energy in the circumferential and axial directions. In other words, it takes about 3 years for the axial growth to produce the same energy as the radial growth does in 30 years. For circumferential growth, it is 5 years. Therefore, growing in the axial direction is energetically the least favorable while growing in the radial direction is energetically the most favorable. This observation motivates the need for an anisotropic treatment of the growth process.

Direction \ Time	t=5	t=10	t=15	t=20	t=25	t=30	Average
Radial	0.3669	0.3670	0.3670	0.3671	0.3671	0.3672	0.3670
Circumferential	0.3671	0.4648	0.7930	1.452	2.435	3.701	1.5355
Axial	0.4075	0.6262	1.1760	2.1140	3.3940	4.9520	2.1116

Table 2.3: Energy in  $\mu J$  for 6 time values.

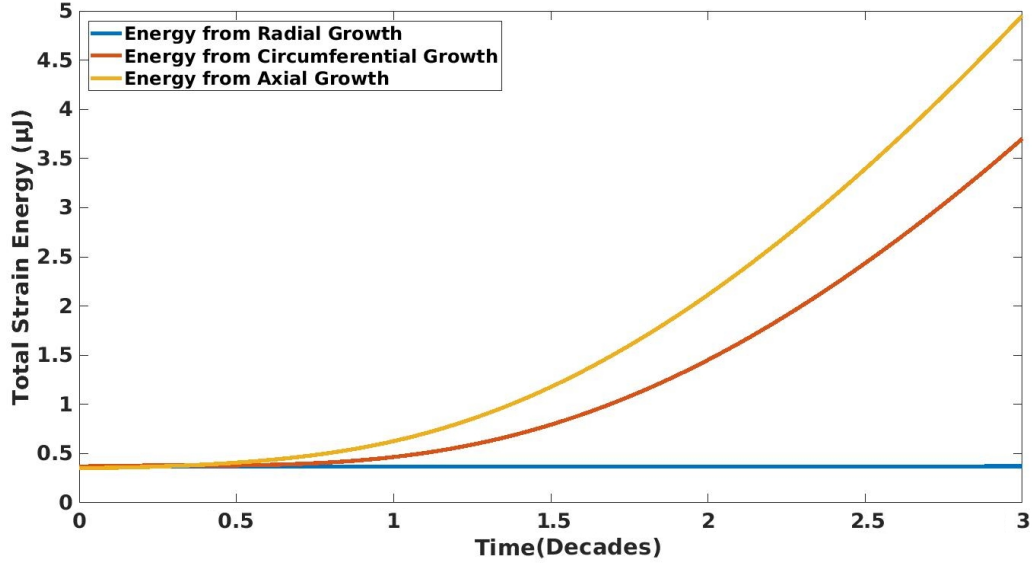


Figure 2.7: The changes in total strain energy for growth in each direction.

## 2.5 Isotropic Growth vs General Anisotropic Growth

Finite element simulation of a fully incompressible material is not possible using the strain energy with  $\Psi_{iso}$  from (2.6). Since  $\nu = 0.5$  for fully incompressible materials, the second term in (2.6) will be undefined. Instead, it is common to use a two field method for such problems. In this method the coefficient  $\frac{\nu}{1-2\nu}\mu_i$  is replaced by a variable  $p$  which in solid mechanics is called “hydrostatic pressure”. In mathematics, it is nothing but a Lagrange multiplier that enforces  $J_e = 1$  in the minimization. Therefore, not only does this method solve for displacement but it also finds a hydrostatic pressure, thus the name two field method [70].

Motivated by the previous section, here we discuss a method to choose an anisotropic growth that is energetically most favorable. We hypothesize that such method will give a growth tensor that has a large weight in the radial component. Our method is inspired by the aforementioned two field minimization for incompressible materials. However, instead of minimizing for a displacement and pressure field we minimize with respect to displacement and growth. Mathematically, we want to find

$\mathbf{u}$  and  $(\alpha_t, \beta_t, \gamma_t)$  that minimizes (2.41) subject to

$$J_{g1} = f(t), \quad \text{at } Z = 0 \quad (2.43)$$

where  $\alpha_t, \beta_t, \gamma_t$  are the parameters in (2.32), (2.33), (2.34). The subscript  $t$  is to emphasize that the minimization happens at each time-step to produce a displacement vector field and three growth parameters. The constraint (2.43) can be imposed by letting  $\gamma_t$  be a function of  $\alpha_t$  and  $\beta_t$  as follows

$$\gamma_t = \frac{\frac{f(t)}{(1+\alpha_t t)(1+\beta_t t)} - 1}{t}, \quad (2.44)$$

This ensures that (2.43) will hold. The function  $f(t)$  is set by the user in this scheme to determine the desired volumetric growth at each step (in our simulations we use  $f(t) = 1 + 2.7t$ ).

After this, we show the importance of using an anisotropic growth scheme as opposed to an isotropic scheme. For the isotropic growth tensor  $\text{diag}(1 + \xi_t t \exp(-aZ^2), 1 + \xi_t t \exp(-aZ^2), 1 + \xi_t t \exp(-aZ^2))$  we choose  $\xi_t$  such that

$$\xi_t = \frac{\sqrt[3]{f(t)} - 1}{t} \quad (2.45)$$

This choice of  $\xi_t$  will ensure that the Jacobian of the growth tensor for both cases are equal at  $Z = 0$  at each time  $t$ . Figure 2.8 shows  $1 + \xi_t t$  as well as  $1 + \alpha_t t, 1 + \beta_t t$  and  $1 + \gamma_t t$  acquired from the two field minimization problem conditional on (2.43).

From Figure 2.8, one can see that this minimization scheme produces a growth regime in which the radial component is dominant. This is not surprising since the energy is very insensitive to radial growth, see Figure 2.7. The axial direction, as expected from Figure 2.7, is the most strictly controlled growth direction.

Now using the growth parameters from Figure 2.8 at each time step, we acquire the evolution of the domain in time, see Figure 2.9. We observe a mild buckling effect in the isotropic case which can be due to the axial stress in each layer. In addition, the intima is thickened but the narrowing of the lumen is not completely a result of intimal thickening in this case. It is clear that buckling contributes to the narrowing

process. On the other hand, for anisotropic growth with approximately the same  $J_g$ , we can clearly observe an intimal thickening close to the center of growth as the main contributor to the encroachment. Figure 2.10 shows that the isotropic growth induces much less stenosis compared to the anisotropic growth. On the other hand, the behavior of the lumen area vs stenosis curves in the anisotropic case (specifically at  $Z = 0$ ) look very similar to Glagov's original data [34]. Finally, a comparison between the energies from the isotropic and anisotropic growth shows that the latter is much more energetically favorable, see Figure 2.11.

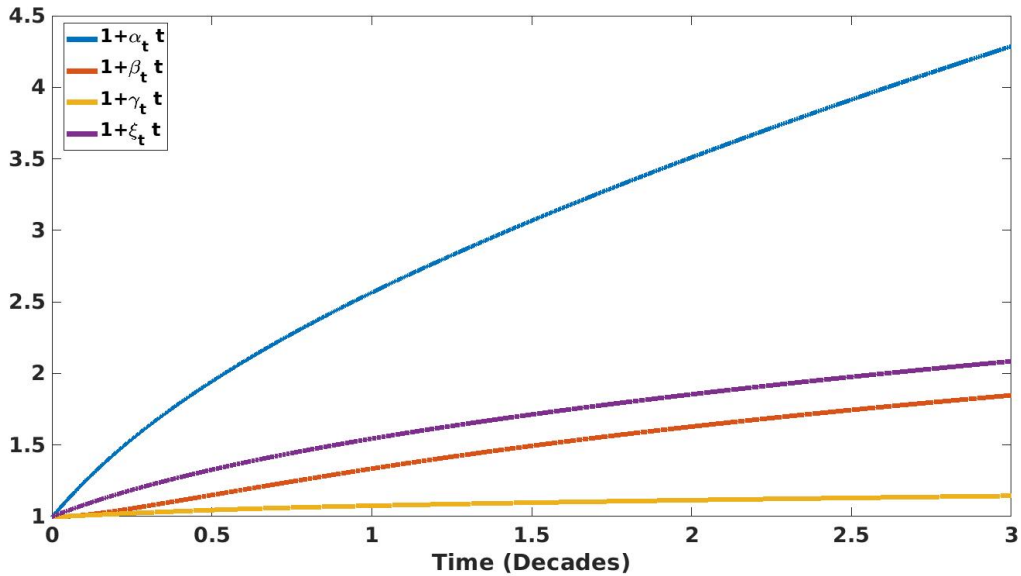


Figure 2.8: Changes in anisotropic growth parameters  $\alpha_t, \beta_t, \gamma_t$  and isotropic growth parameter  $\xi_t$ .

In addition, we investigate the changes in the fiber angles and values of  $I_4$  in (2.9). The latter can be thought as a measurement of stiffness for each layer. In both isotropic and anisotropic cases, the fiber angle in the intima increases the most, see Figure 2.12(a) and (c). However, Figures 2.12 (b) and (d) show that  $I_4$  does not change significantly in the intima in both cases. Physically, this means the fibers do not change their length in the intima, only their orientation. In addition, Figures 2.12 (b) and (d) show that the isotropic case eventually has a stiffer adventitia but a more compliant media than the anisotropic case. Therefore, the intima in the anisotropic case finds it

easier growing inward than pushing against a stiffer media to grow outward. Therefore, the intima in the anisotropic case finds it easier growing inward than pushing against a stiffer media to grow outward. This is supported by the difference in the sizes of the inward bulges in the two cases in Figure 2.9.

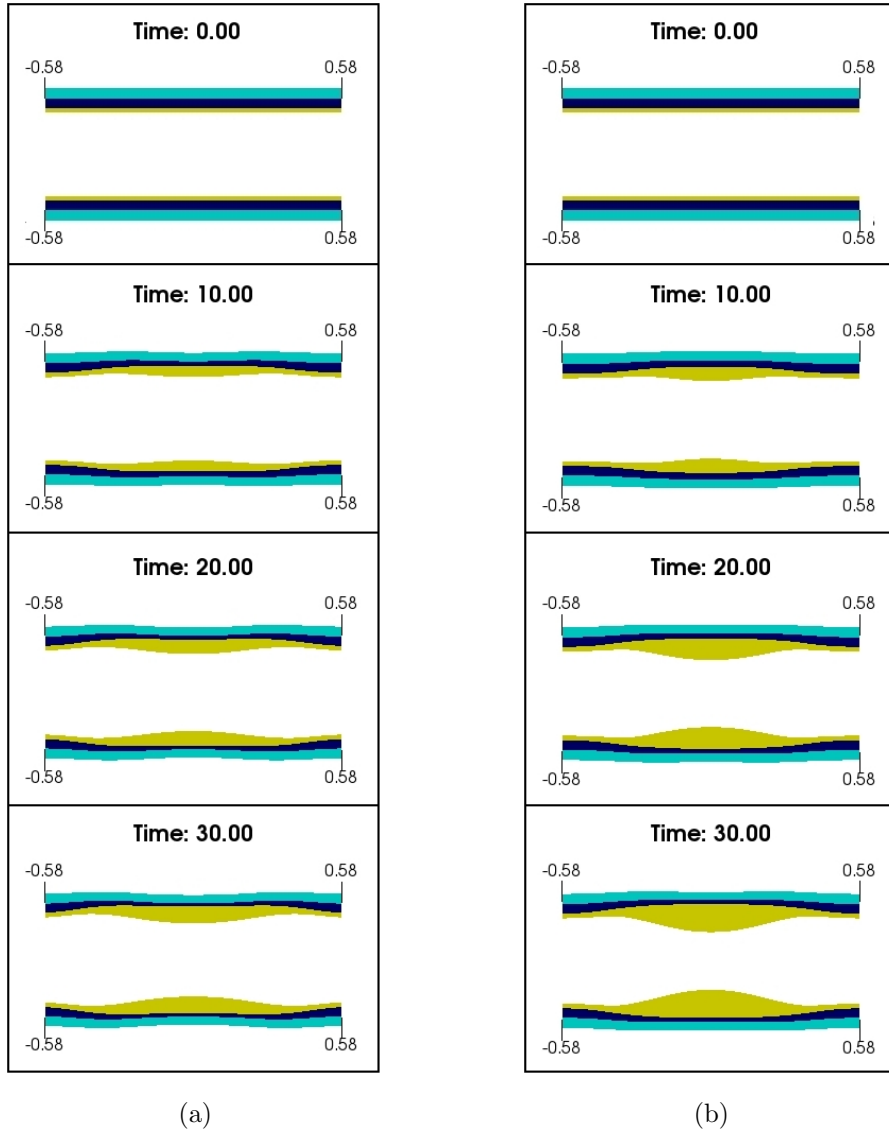


Figure 2.9: Evolution of the domain for  $-0.58 \leq Z \leq 0.58$  subject to (a) isotropic growth with  $\xi_t$  from Fig. 2.8, (b) general anisotropic growth with  $(\alpha_t, \beta_t, \gamma_t)$  from Fig. 2.8. Parameter  $a$  in (2.32)-(2.34) is taken to be 14.29.

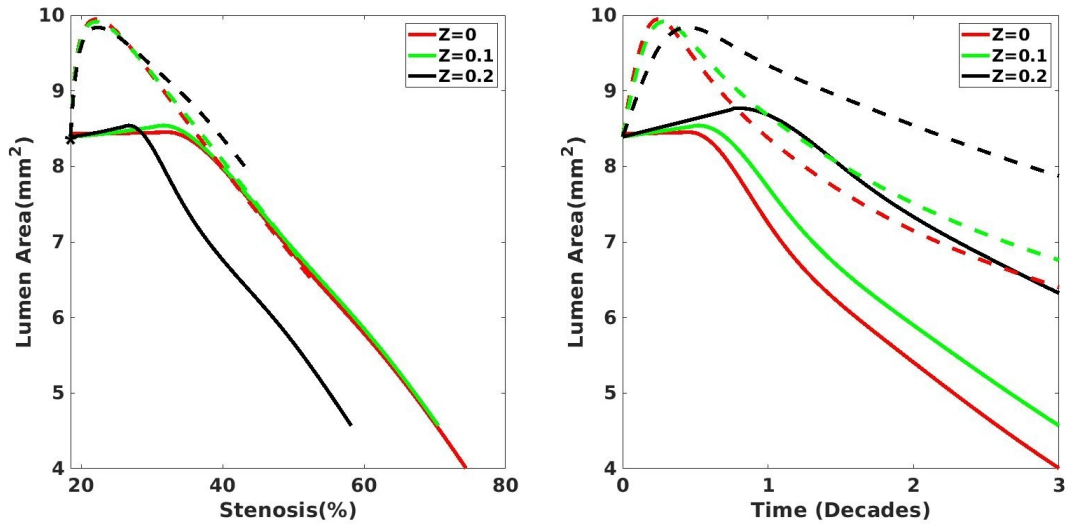


Figure 2.10: *Left:* Comparison between the lumen area against stenosis for both isotropic and anisotropic growth. Star denotes the time  $t = 0$ . *Right:* Comparison between the lumen area in time for both isotropic and anisotropic growth. *Dashed* lines correspond to isotropic and *solid* lines correspond to anisotropic growth.

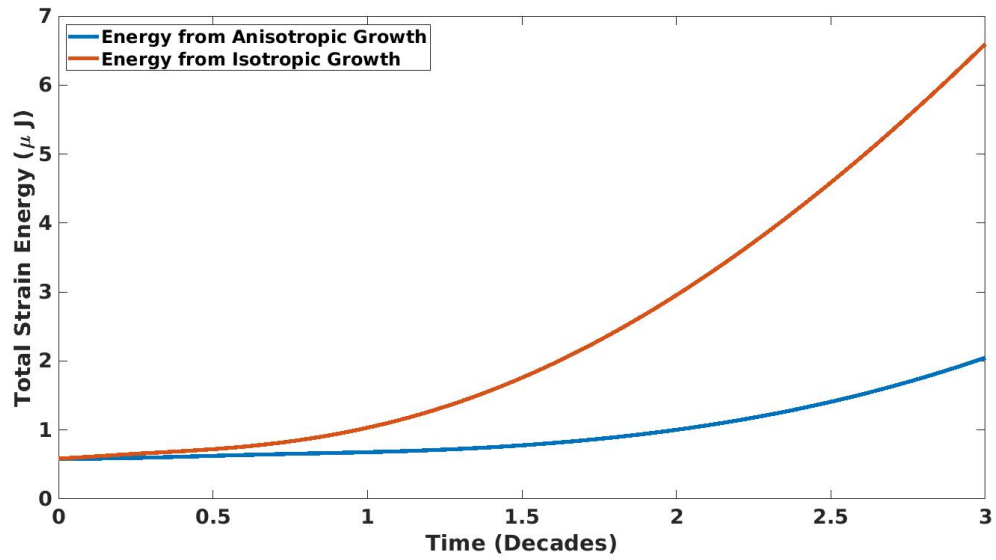
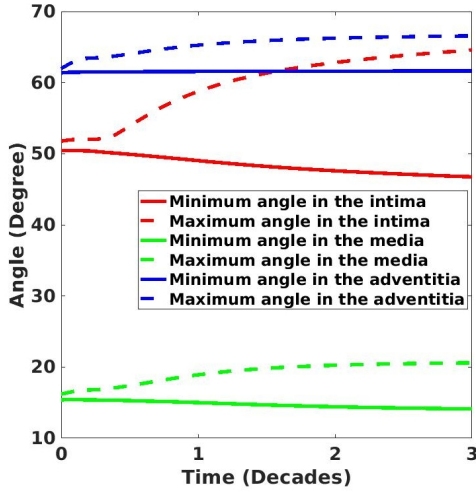
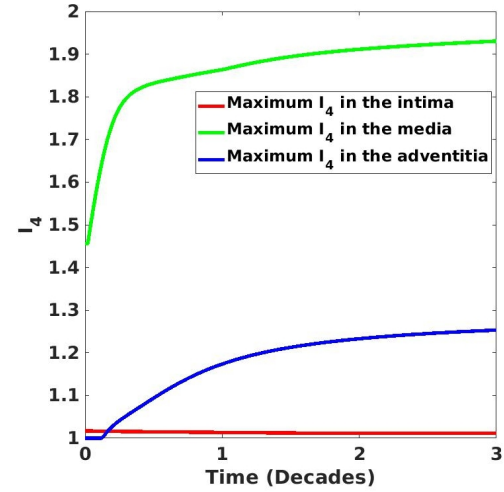


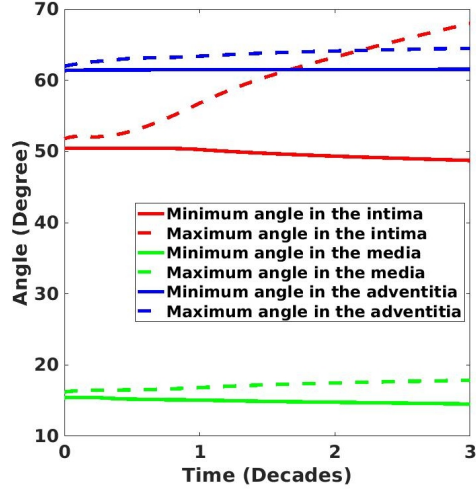
Figure 2.11: Changes in the strain energy produced by isotropic and anisotropic growth in time.



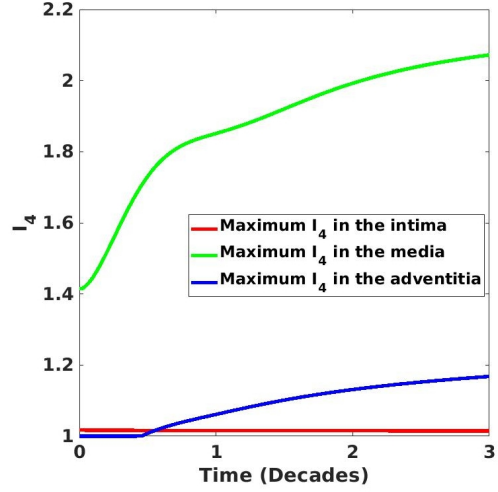
(a)



(b)



(c)



(d)

Figure 2.12: *Top:* These graphs belong to the case of isotropic growth with  $\xi_t$  from Fig. 2.8. (a) Changes in the minimum and maximum fiber angles. (b) Changes in the maximum of  $I_4$  in each layer.

*Bottom:* These graphs correspond to the anisotropic growth with  $(\alpha_t, \beta_t, \gamma_t)$  from Fig. 2.8. (c) Changes in the minimum and maximum fiber angles. (d) Changes in the maximum of  $I_4$  in each layer.

## 2.6 Conclusion

In this chapter, we investigated an axisymmetric growing artery using morphoelasticity. First, we were curious to see the effect of growth in each direction separately. This allowed us to associate each aspect of the Glagov remodeling phenomenon with growth in a certain direction. We observed that the radial growth is the main culprit in encroachment of the vessel while circumferential growth is responsible for the outward remodeling. In the case of axial growth, we saw both types of remodeling. However, the inward remodeling was partly a result of arterial wall buckling. We also saw that radial growth thickens the intima without changing the thickness of the other two layers. The circumferential growth thins the media and thickens the intima slightly, and the axial growth slightly thickens the intima, thins the media and stretches the artery axially.

We hypothesized that if the growth tensor is determined by an energy minimization, radial growth would emerge to become dominant. We suggested a displacement-growth two field minimization framework to test our hypothesis. As we expected, due to the large energy produced by axial and circumferential growth, this prescription suppresses the effect of these growth directions. In other words, for the growth tensor

$$\mathbf{G} = \text{diag}(1 + \alpha_t t \exp(-aZ^2), 1 + \beta_t t \exp(-aZ^2)), 1 + \gamma_t t \exp(-aZ^2))$$

the parameters  $\alpha_t$ ,  $\beta_t$  and  $\gamma_t$  follow  $\alpha_t > \beta_t > \gamma_t$  for the most part.

To further enforce the need for an anisotropic treatment of our problem, we investigated an isotropic growth with the growth tensor

$$\mathbf{G} = \text{diag}(1 + \xi_t t \exp(-aZ^2), 1 + \xi_t t \exp(-aZ^2)), 1 + \xi_t t \exp(-aZ^2))$$

The parameter  $\xi_t$  is chosen such that the maximum Jacobian of growth (which happens at  $Z = 0$ ) for both cases is exactly the same for each time step  $t$ . Our result is that, the anisotropic growth is much more energetically favorable than the isotropic case for the same amount of volumetric growth. Furthermore, on a plot of lumen area vs stenosis, we saw more stenosis for the most energetically favorable anisotropic growth than isotropic growth. This was expected due to the dominance of growth in the radial direction and the increased effective stiffness of the media layer in the anisotropic case.

Many studies have shown that smooth muscle cell (SMC) proliferation is the reason for intimal thickening ([37], [89], [27] and [68]). In addition, there are studies that suggest that SMC proliferation is regulated by changes in the circumferential stress in the vessel wall [101] or changes in wall shear stress induced by blood flow ([94] and [39]). Although it is acknowledged that atherosclerosis proceeds because of growth in the intima, few authors have studied the nature of the anisotropy in the growth tensor when they model this phenomenon. Our approach was to choose an anisotropic growth tensor based on minimizing the strain energy. The result was a radially dominant growth, consistent with experiments on radial construction in arterial walls [36]. According to [36], smooth muscle cells (SMCs) have to re-orient themselves to become “bricks” in the vessel wall. Cells in different layers re-orient themselves at different times, so that there is a re-orientation wave that radiates outwards. This radial patterning is probably due to a platelet derived growth factor (PDGF) wave that itself has a strong radial component. In chapter 4, we will use a simple model for the distribution of PDGF and we use it to define a growth tensor. However, it would be more interesting to compute the effective growth tensor from experiments [36] and compare them with our model predictions.

Even though our growth tensor was found using the mathematical tool of energy minimization, we hope that biological experiments can also motivate specific choices for the form of  $\mathbf{G}$  and therefore the functional form of  $\alpha_t$ ,  $\beta_t$  and  $\gamma_t$ . With advances in nanospring technology, it may eventually be possible to measure the energy associated with growth in radial, circumferential and axial directions [49]. We believe that finding a practical way to control or change the anisotropy of growth might be the key to slow down or even reverse inward remodeling which is responsible for affecting local hemodynamics and promoting medical conditions such as angina.

## Chapter 3

### ATHEROSCLEROSIS MODEL IN THREE DIMENSIONS

In biomechanics, residual stress and strain are the stress and strain that still remain within an artery even after all the external forces have been removed. It is known that residual stress/strain plays an important role in studying atherosclerosis. For example, Ohayon et al. 2007 showed that without residual stress the maximum strain for the fibrous cap is overestimated, [71]. Also as mentioned in the introduction, the distribution of shear stress in the vessel wall can cause endothelial dysfunction which triggers the plaque formation inside the intima. However, residual stress can reduce the stress concentration (due to deformation) at the inner wall of the vessel *in-vivo*, [17]. These and many other studies attest to the importance of residual stress/strain.

For a long time, the arterial cross sections excised from a subject were considered to be stress free. However, Vaishnav and Vossoughi, showed that by creating a radial cut on an arterial cross section it springs open [95]. This shows that arterial rings are still under stress even after boundary loadings such as blood pressure have been removed. Later in 1989, Fung and Liu defined the opening angle for an annular arterial cross section to be the angle between the two lines that join the midpoint of the inner arc and its tips [28], see Figure 3.1.

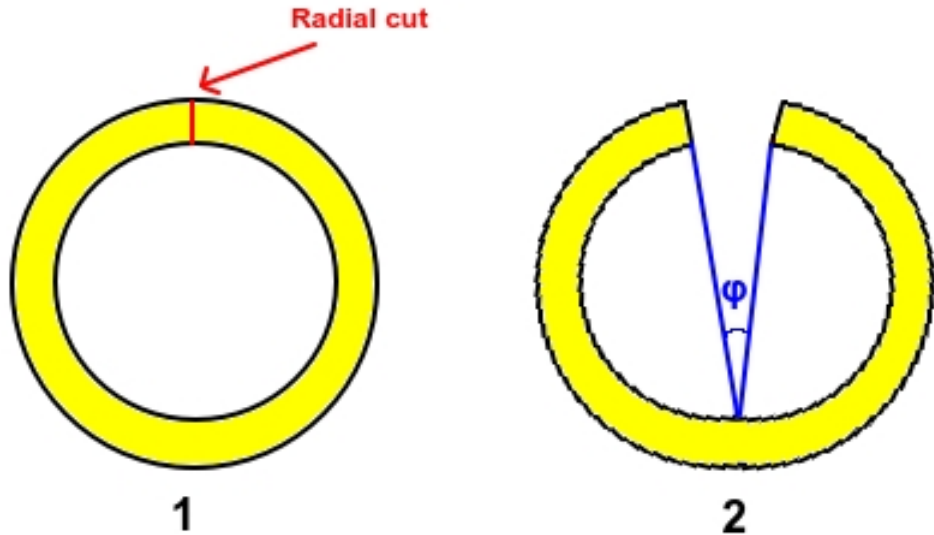


Figure 3.1: A radial cut on an annular arterial cross section causes it to spring open. This is evidence for residual stress. The angle shown in 2 is the opening angle.

There is not a lot known about the source of residual stress/strain. However, in this chapter, we will show that intimal growth can directly affect the opening angle for an artery.

### 3.1 Assumptions and methods

In this chapter we focus on a general 3D model of a growing artery in Cartesian coordinate system. The geometry of the intima is extracted from Kubo's intravascular ultrasound (IVUS) images<sup>1</sup> [54]. Then we add a media and adventitia layer (with realistic thicknesses [46]) to construct a three layered arterial wall, see Figure 3.2. The height of the domain is 1 centimeter so that  $-0.5 \leq Z \leq 0.5$ . We further assume that our simulation starts from a stress free configuration even though the intima is already thickened, see Figure 3.2. This is because we do not have any information about stress distribution in Kubo's baseline IVUS images.

---

<sup>1</sup> This choice is solely to avoid too many different domains throughout this thesis and also maintain a visual connection with the next chapter

Since our domain is not symmetric, we cannot use cylindrical coordinates like chapter 2. Therefore, Cartesian coordinates system is the natural choice. There is no reason to assume growth in a general 2D cross section is aligned with the x and y directions. To overcome this issue, we will use a transformation which we will discuss later.

We consider  $(X, Y, Z)$  to be a generic point in the reference domain and  $(x, y, z)$  as the one in the deformed domain. Now supposing  $\mathbf{u}$  is the displacement vector that maps the reference domain into the deformed domain, the deformation gradient from (2.26) takes the form

$$\mathbf{F} = \begin{bmatrix} \frac{\partial x}{\partial X} & \frac{\partial x}{\partial Y} & \frac{\partial x}{\partial Z} \\ \frac{\partial y}{\partial X} & \frac{\partial y}{\partial Y} & \frac{\partial y}{\partial Z} \\ \frac{\partial z}{\partial X} & \frac{\partial z}{\partial Y} & \frac{\partial z}{\partial Z} \end{bmatrix} \quad (3.1)$$

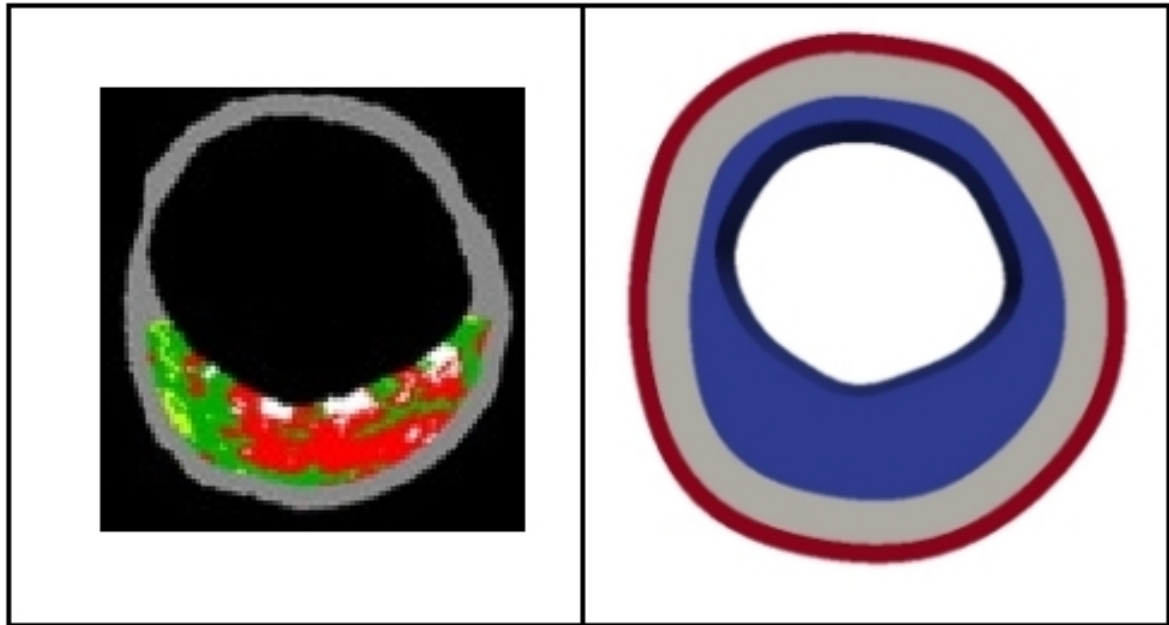


Figure 3.2: *Left:* IVUS image of a coronary artery cross section. *Right:* Our three-layer domain.

We also have to give a formula for the fiber direction  $\mathbf{b}(X, Y, Z)$  in Cartesian coordinates. We follow the procedure proposed by Fok and Gou [26]. Wang et al.

also use a similar approach to find the fiber direction in the human left ventricle [99]. Suppose  $\mathbf{b}(X, Y)$  is the projection of the fiber direction onto the  $XY$ -plane. If  $(X, Y)$  is a point on any of the boundaries then  $\mathbf{b}(X, Y)$  is the unit tangent vector at  $(X, Y)$ . If  $(X, Y)$  is an inner point of a layer, we take  $\mathbf{b}(X, Y)$  to be a weighted average of the tangents on the inner ( $\mathbf{v}_A$ ) and outer ( $\mathbf{v}_C$ ) boundary of the layer, see Figure 3.3.

$$(b_1, b_2) = \frac{|BA|\mathbf{v}_C + |BC|\mathbf{v}_A}{|BA| + |BC|} \quad (3.2)$$

where point A is the closest point to B on the inner boundary and point C is the closest point to B on the outer boundary. After acquiring the X and Y coordinates from (3.2) to get  $\mathbf{b}(X, Y, Z)$ , we use the following formula

$$\mathbf{b}(X, Y, Z) = \frac{(b_1, b_2, \sqrt{b_1^2 + b_2^2} \tan \varphi)}{\sqrt{(b_1^2 + b_2^2)(1 + \tan^2 \varphi)}} \quad (3.3)$$

where  $\varphi$  is given in Table 2.1 for each layer, see Figure 3.3. Furthermore, we use the Cartesian version of (2.35) without any body forces or blood pressure loading:

$$\begin{aligned} & \text{Find } \mathbf{u} \in C^2(\Omega) \text{ such that} \\ & \sum_{i=1}^3 \iiint_{\Omega_i} \left( J_{g_i} \frac{\partial W_i}{\partial \mathbf{F}_{e_i}} \mathbf{G}_i^{-T} : \nabla \mathbf{v} \right) dV = 0 \quad \forall \mathbf{v} \in C^2(\Omega) \end{aligned} \quad (3.4)$$

and the energy associated with the growth and deformation (2.41) will be

$$E = \sum_{i=1}^3 \iiint_{\Omega_i} J_{g_i} W_i dV \quad (3.5)$$

where  $J_{g_i} = \mathbf{G}_i$  and  $\mathbf{G}_i$  is the identity tensor when  $i = 2, 3$ , since there is no growth in the media and adventitia. The formula for  $\frac{\partial W_i}{\partial \mathbf{F}_{e_i}}$  is still (2.31) and  $\Omega_i$  corresponds to intima, media and adventitia for  $i = 1, 2, 3$ . We use the same parameters from Table 2.1, except  $A_1$ - $A_4$  are now described by parametric functions  $f_1(\Theta)$ - $f_4(\Theta)$  measured in mm and  $L = 1$  cm. To see how we acquire these functions from the IVUS images refer to the appendix. The number of tetrahedron elements in this chapter is 25500 (see Figure 3.4) and we use quadratic basis elements to avoid locking. Mesh is finer in the intima than media and adventitia, since the growth is located in the intima and it undergoes the most deformation.

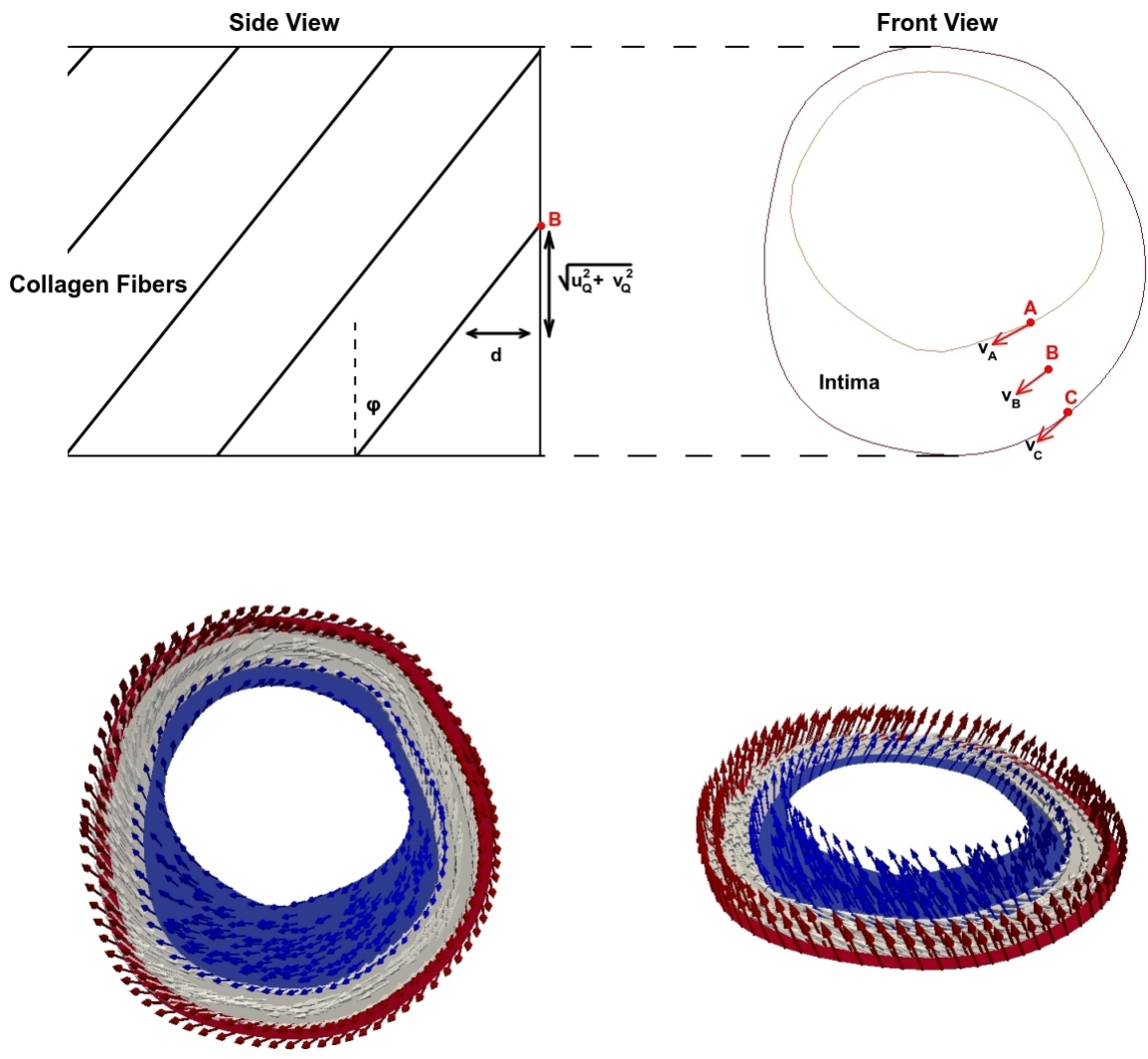


Figure 3.3: *Top:* Side view and front view of a family of fibers. The fiber direction at an inner point  $B$  is the average of inner and outer boundary unit tangent vectors at the points closest to  $B$ . The weight is determined by the distance between points. *Bottom:* The fiber orientations in each layer at a cross section of our 3D domain.

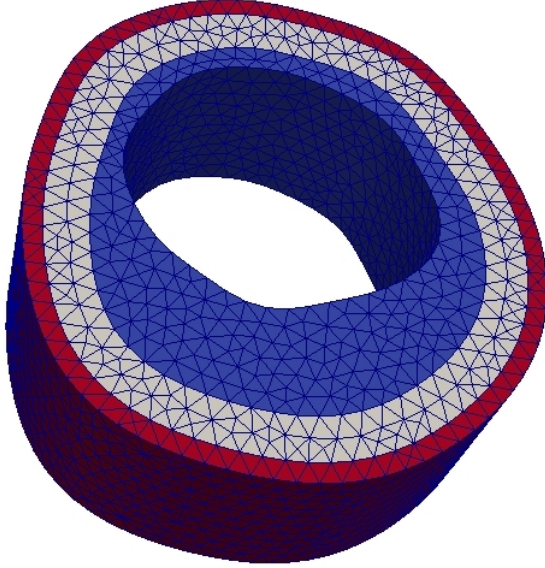


Figure 3.4: A sample mesh.

### 3.1.1 Coordinate system transformation

Since our domain is not axisymmetric, we cannot use cylindrical coordinates in the same way we did in chapter 2. However, there is a similar coordinate system which is point-wise defined and is common in mechanical engineering. This coordinate system is called the fiber coordinate system  $(\mathcal{R}, \Phi, \mathcal{Z})$  with basis vectors  $\mathbf{e}_{\mathcal{R}}(X, Y, Z), \mathbf{e}_{\Phi}(X, Y, Z), \mathbf{e}_{\mathcal{Z}}$  [32, 56, 100]. The vector  $\mathbf{e}_{\mathcal{Z}}$  is parallel to the axial direction and it is spatially independent,  $\mathbf{e}_{\Phi}(X, Y, Z)$  is parallel to the projection of the fiber onto the  $XY$  plane at each point  $(X, Y, Z)$  and  $\mathbf{e}_{\mathcal{R}}(X, Y, Z)$  is in the direction of  $\mathbf{e}_{\Phi}(X, Y, Z) \times \mathbf{e}_{\mathcal{Z}}^2$ . In this chapter, we refer to  $\mathbf{e}_{\mathcal{R}}$ ,  $\mathbf{e}_{\Phi}$  and  $\mathbf{e}_{\mathcal{Z}}$  as radial, fiber and axial direction, see Figure 3.5.

---

<sup>2</sup> for convenience, from now on we refrain from stating the dependence of  $\mathbf{e}_{\mathcal{R}}$  and  $\mathbf{e}_{\Phi}$  on  $(X, Y, Z)$ .

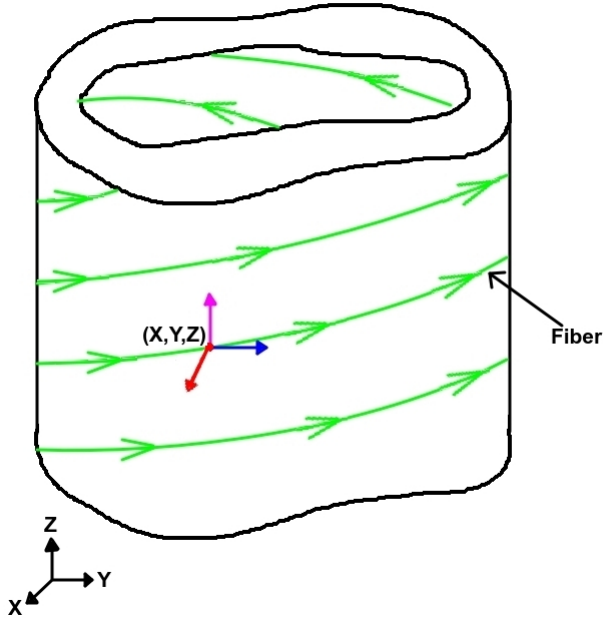


Figure 3.5: Fiber coordinate system at a point  $(X, Y, Z)$ . Red arrow pointing outside of the domain is  $\mathbf{e}_R$ , blue arrow is  $\mathbf{e}_\Phi$  and the purple arrow is  $\mathbf{e}_Z$ .

Since growing in the  $X$  and  $Y$  direction for a tube shaped domain like ours is not intuitive, we prefer to describe our growth tensor in a way that fits our geometry better. We utilize the fiber coordinate system for this purpose. We introduce a growth parameter tensor in the fiber coordinate system as follows:

$$\mathbf{M} = \begin{bmatrix} \alpha_t & 0 & 0 \\ 0 & \beta_t & 0 \\ 0 & 0 & \gamma_t \end{bmatrix} \quad (3.6)$$

with  $\alpha_t$ ,  $\beta_t$  and  $\gamma_t$  being time dependent growth parameters in radial, fiber and axial direction. We need to construct the corresponding growth tensor in Cartesian coordinates using (3.6). The transformation tensor uses the fiber direction (3.2) and has the form

$$\mathbf{T} = \begin{bmatrix} \cos(\theta(X, Y)) & -\sin(\theta(X, Y)) & 0 \\ \sin(\theta(X, Y)) & \cos(\theta(X, Y)) & 0 \\ 0 & 0 & 1 \end{bmatrix} \quad (3.7)$$

where  $\theta(X, Y) = \arctan\left(\frac{b_2}{b_1}\right)$  for  $b_1$  and  $b_2$  from (3.2). Now we have a growth tensor in Cartesian coordinates, which is used in (3.4) in the intima:

$$\mathbf{G} = \mathbf{I} + (\mathbf{TMT}^T) * f(X, Y, Z)t \quad (3.8)$$

where  $\mathbf{I}$  is the identity tensor and  $f(X, Y, Z)$  is given by

$$f(X, Y, Z) = \exp\left\{-a[(X - X_0)^2 + (Y - Y_0)^2 + (Z - Z_0)^2]\right\} \quad (3.9)$$

For this chapter, we take  $a = 4.5$  and  $(X_0, Y_0, Z_0) = (0, -0.8, 0)$ . Figure 3.6 shows where the growth is located.

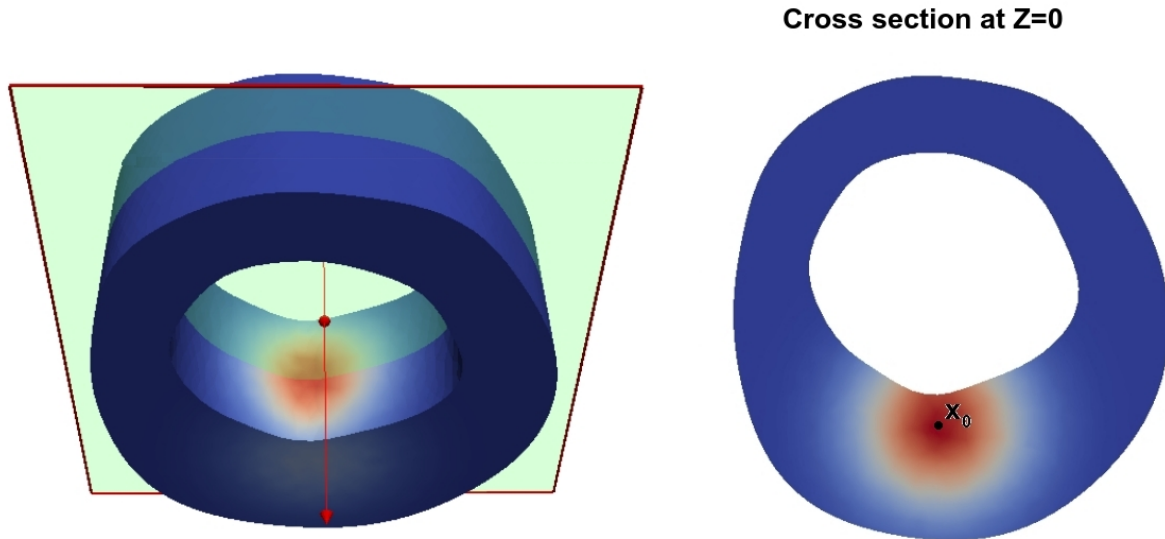


Figure 3.6: Local growth centered at  $(X_0, Y_0, Z_0) = (0, -0.8, 0)$ .

### 3.1.2 Results

First, we investigate the effect of growth on the opening angle in each fiber coordinate direction. We create radial cuts directly on the opposite side of where the growth is centered, see Figure 3.7. To get a purely radial growth, all we have to do is to let  $\mathbf{M} = \text{diag}(\alpha_t, 0, 0)$  and then use formula (3.8). Similarly, by  $\mathbf{M} = \text{diag}(0, \beta_t, 0)$

and  $\mathbf{M} = \text{diag}(0, 0, \gamma_t)$  in (3.8), we acquire growth in fiber and axial directions. For simplicity, we take  $\alpha_t$ ,  $\beta_t$  and  $\gamma_t$  to be 1 for each case. Also we take  $J_g = 1 + 2.7t$ . Figure 3.7 shows deformed arterial sections after 3 decades of growth.

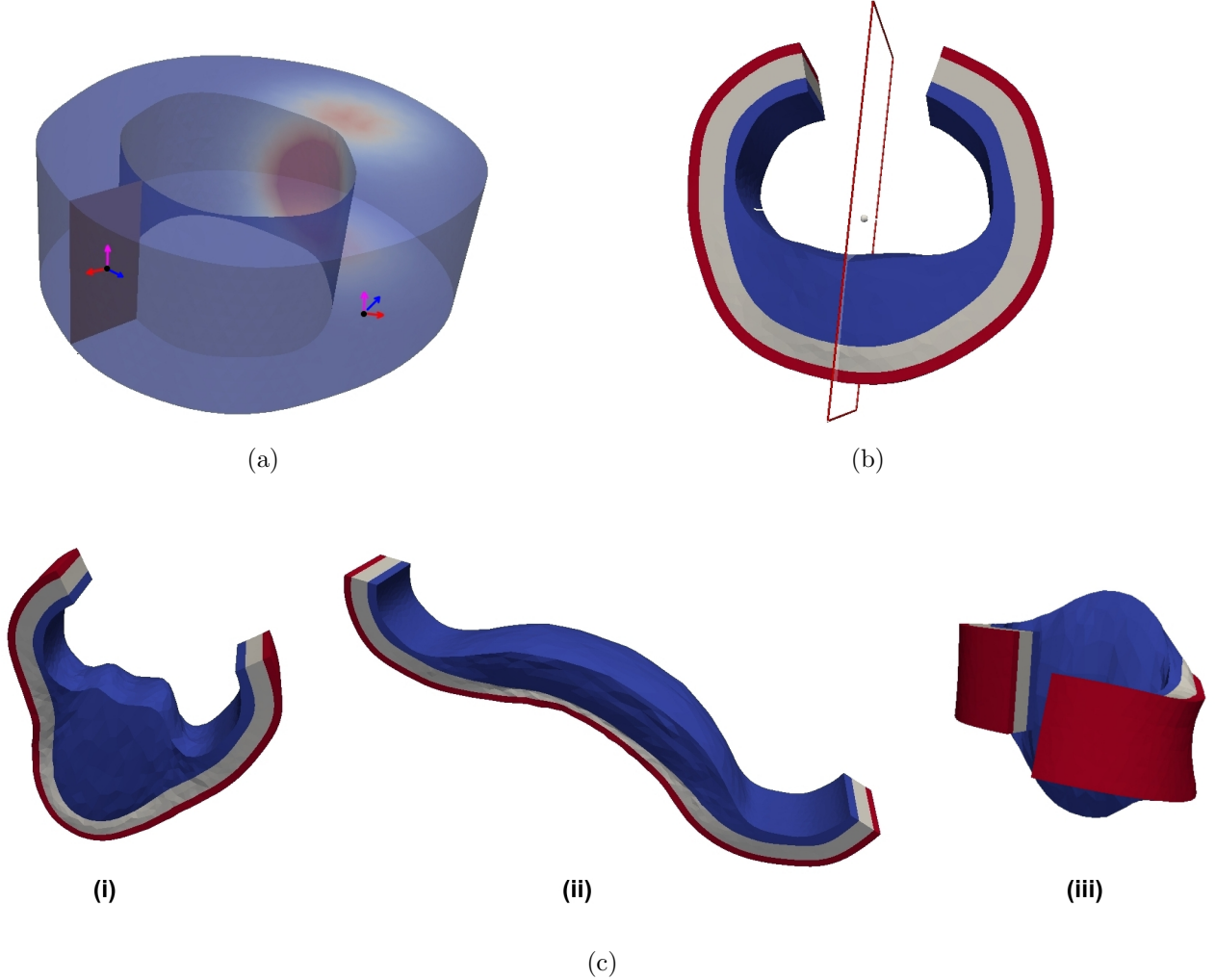


Figure 3.7: (a) Schematic of the fiber coordinate system in the reference uncut domain at a random point and a point on the site of the radial cut. Red, blue and purple arrows correspond to radial, fiber and axial directions in the fiber coordinate system. (b) The hinge of the opening angle is at the intersection of the endothelium with the plane  $x = 0$ . (c) Deformed arterial sections due to growth in the (i) radial direction, (ii) fiber direction and (iii) axial direction.

According to Figure 3.7, one can see that growth in the fiber direction has the biggest effect on the opening angle. Axial growth, on the other hand, does not change

the opening angle significantly. This was expected since mathematically the radial cut is created via a plane that belongs to  $\text{span}\{\mathbf{e}_R(X, Y, Z), \mathbf{e}_Z\}$ , see Figure 3.7(a). Maybe an analogy between opening angles and opening doors can illustrate our point. Opening a door is much easier when the force exerted and the surface of the door are orthogonal. The smaller the angle between these two, the more difficult it is to move the door. Now for all  $(X, Y, Z)$ , the fiber direction creates the biggest angle with the cut surface and therefore creates the biggest opening angle, see Figure 3.7(b). According to this argument, one might expect the axial and radial growth to create much less opening (probably none), but we should not forget that the radial direction is spatially dependent, the growth is localized and the geometry is not symmetric. All of these factors contribute to the opening angle in the axial and radial directions.

Using the two field method from chapter 2, we minimize (3.5) to find a displacement field  $\mathbf{u}$  and a triple  $(\alpha_t, \beta_t, \gamma_t)$  for the growth tensor in (3.8) with Jacobian constraint of  $J_g = 1 + 2.7t$ . In addition, we compute the corresponding isotropic parameter  $\xi_t$  using (2.45). Using the triple  $(\alpha_t, \beta_t, \gamma_t)$  and  $\xi_t$  (refer to (2.45)), the maximum growth tensor entries for isotropic and anisotropic growth are shown in Figure 3.8. The radial growth is once again the dominant direction of growth. However, we must keep in mind that the geometry in this chapter is very different from the one in chapter 2. A shorter artery requires less energy to grow axially, thus  $1 + \gamma_t t$  looks more significant than the one in chapter 2, see Figure 2.8.

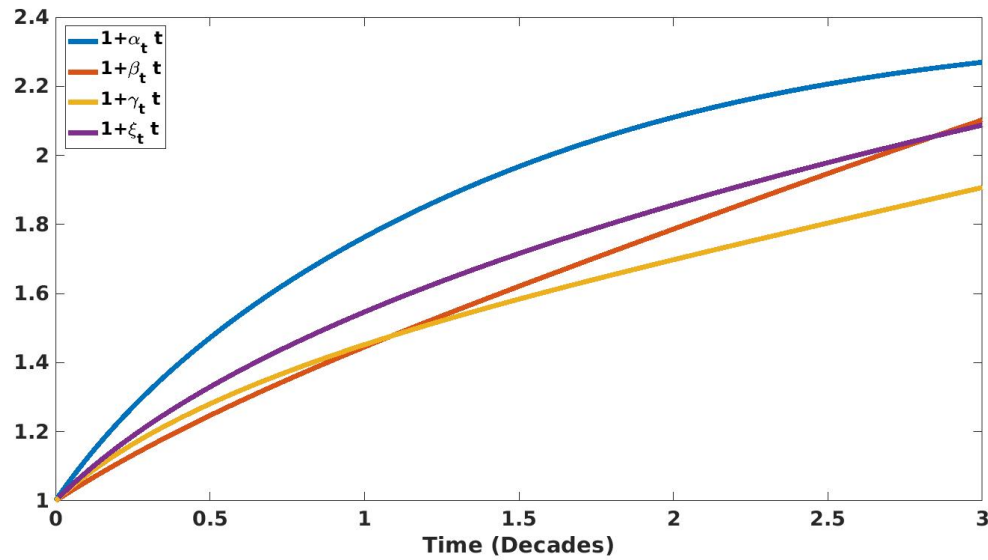


Figure 3.8: Changes in growth tensor entries in time.

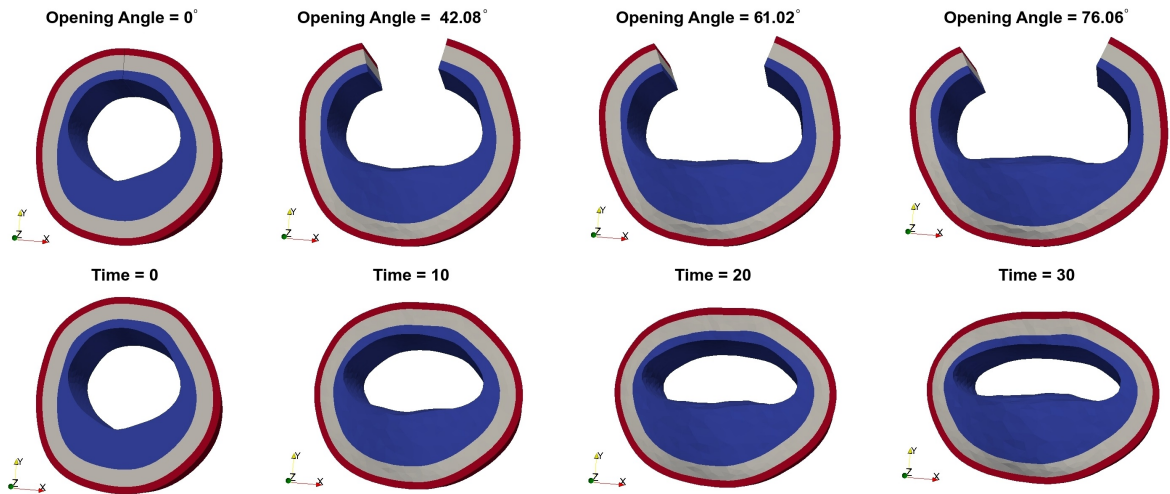


Figure 3.9: Anisotropic growth. *Top:* Changes in the opening angle. *Bottom:* Evolution of the intact domain. The hinge of the opening angle is the intersection of the endothelium with the plane  $x = 0$ , see Figure 3.7(b)

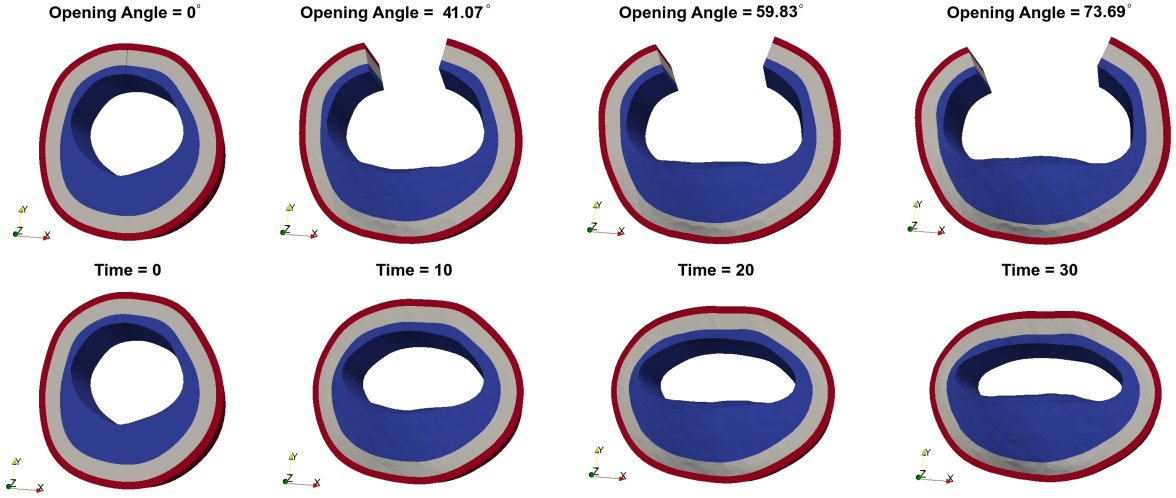


Figure 3.10: Isotropic growth. *Top*: Changes in the opening angle. *Bottom*: Evolution of the intact domain. The hinge of the opening angle is the intersection of the endothelium with the plane  $x = 0$ , see Figure 3.7(b).

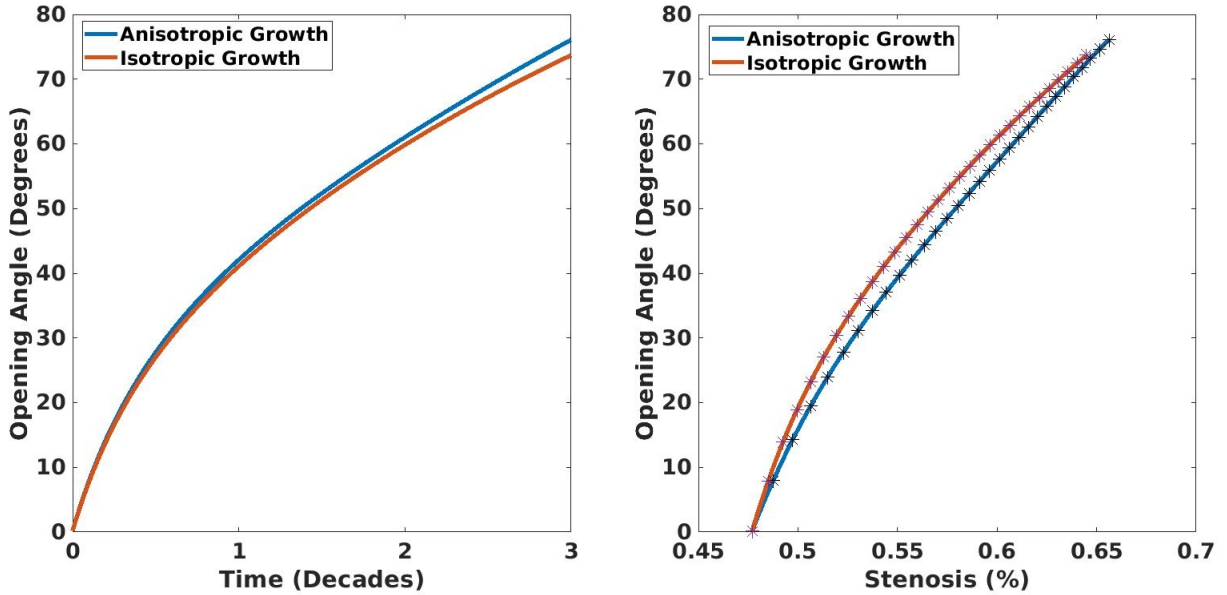


Figure 3.11: *Left*: The opening angle as a function of time. *Right*: The opening angle as a function of stenosis. Stars mark every 0.1 decade.

Figures 3.9 and 3.10 show the opening angle for four time steps and their intact counterparts in 3D. The anisotropic growth opens the angle slightly more than the

isotropic growth. Figure 3.11 shows the opening angle as a function of time and stenosis for anisotropic and isotropic cases. Kubo's IVUS image baseline has a thickened intima and that is why stenosis in Figure 3.11 starts around 47%. These results show that not only does the most energetically favorable anisotropic growth cause more stenosis with less energy, but it also leads to a slightly bigger opening angle. A longer domain is going to result in a more significant difference. In that case, our method will suppress the axial growth more strictly in the anisotropic case (like in chapter 2). Therefore, the  $1 + \xi_t t$  in Figure 3.8 will look less like the average of  $1 + \alpha_t t$ ,  $1 + \beta_t t$  and  $1 + \gamma_t t$ .

So far, we have seen the effect of anisotropic and isotropic growth regimes on the opening angle. Now we want to compare the strains for each case. It is a natural choice in experiments to compute the strains in fiber coordinate system. We use the components of  $\mathbf{T}^T \mathbf{F}_e \mathbf{T}$  as the strain measures in each direction in the fiber coordinate system. Tensor  $\mathbf{T}$  is the transformation in (3.7) and  $\mathbf{F}_e$  is the elastic response tensor from (1.4). The entries  $(\mathbf{T}^T \mathbf{F}_e \mathbf{T})_{11}$ ,  $(\mathbf{T}^T \mathbf{F}_e \mathbf{T})_{22}$  and  $(\mathbf{T}^T \mathbf{F}_e \mathbf{T})_{33}$  correspond to the strain in the radial, fiber and axial direction respectively.

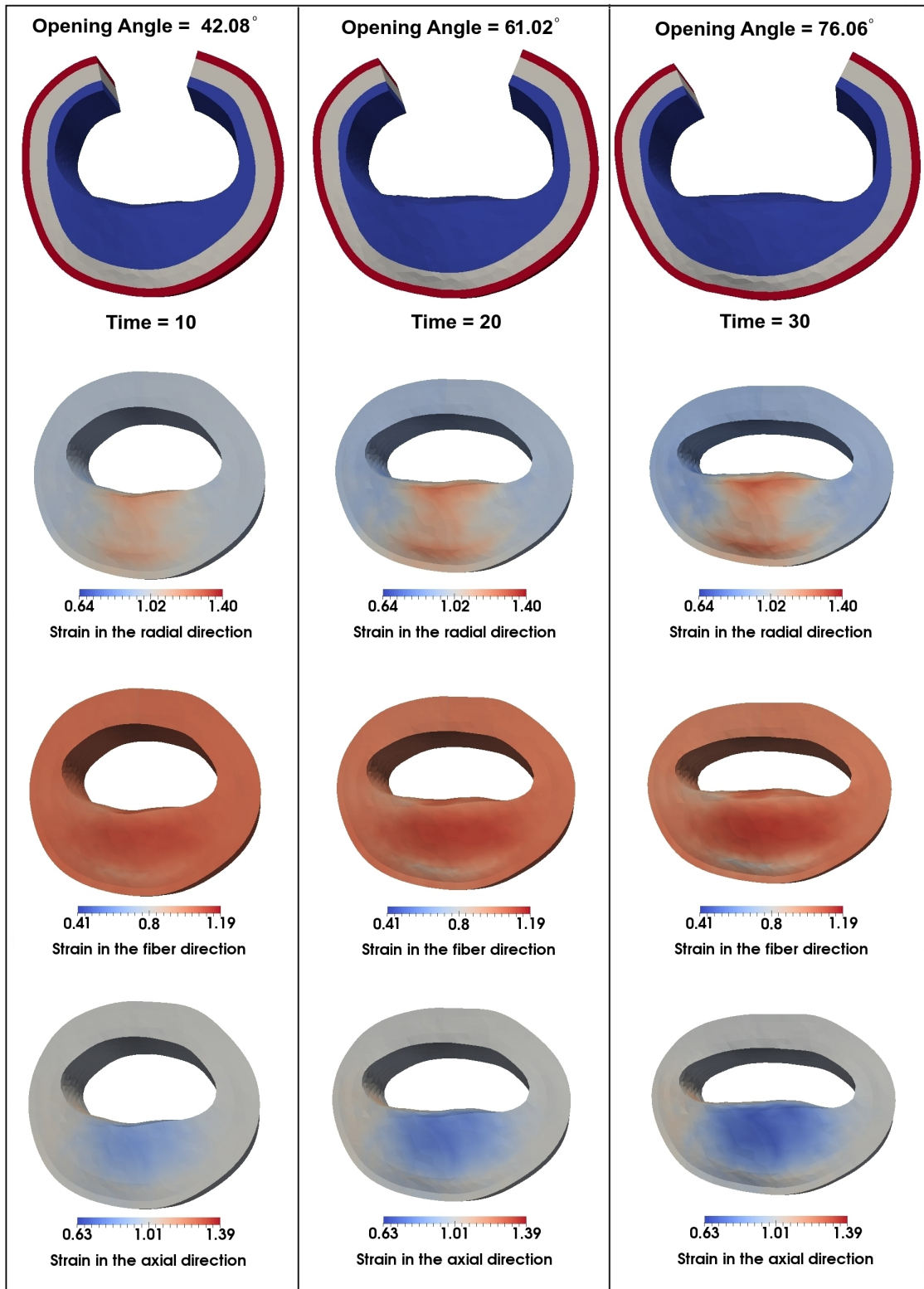


Figure 3.12: Strains in radial, fiber and axial directions for anisotropic growth.

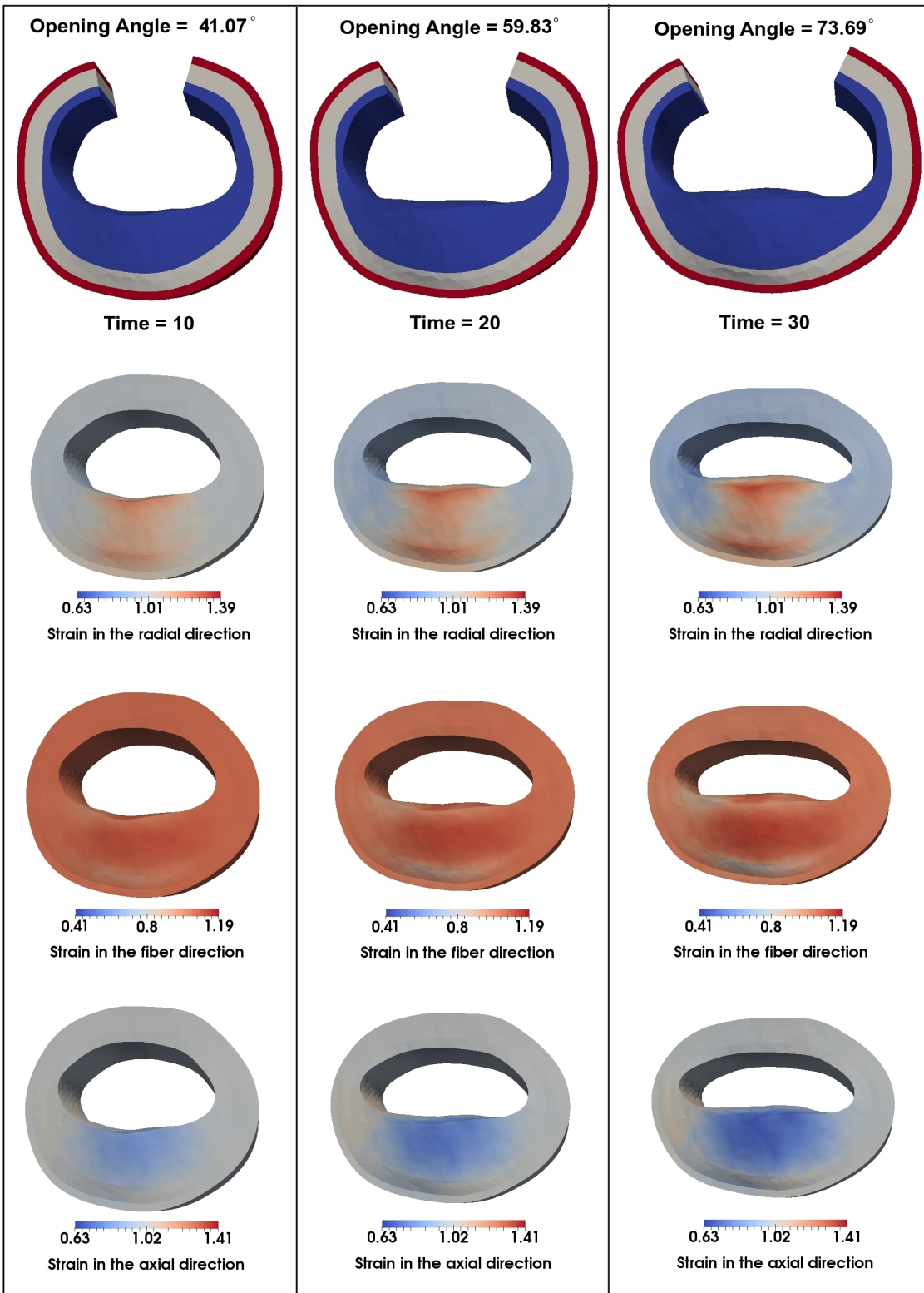


Figure 3.13: Strains in radial, fiber and axial directions for isotropic growth.

Figures 3.12 and 3.13 show the strain in each direction for the anisotropic and isotropic growth respectively. Both figures show that strain in the fiber direction engages the whole domain while in the radial and axial directions higher strains are more localized. Figure 3.14 compares the maximum strain as a function of the opening angle in each direction for anisotropic and isotropic case. One can see that strain in the fiber direction is the smallest in both cases. This might be due to the collagen fibers resisting the strain. In addition, isotropic growth generally results in slightly larger strains. This agrees with intuition since anisotropic growth occurred as a result of minimizing the total energy.

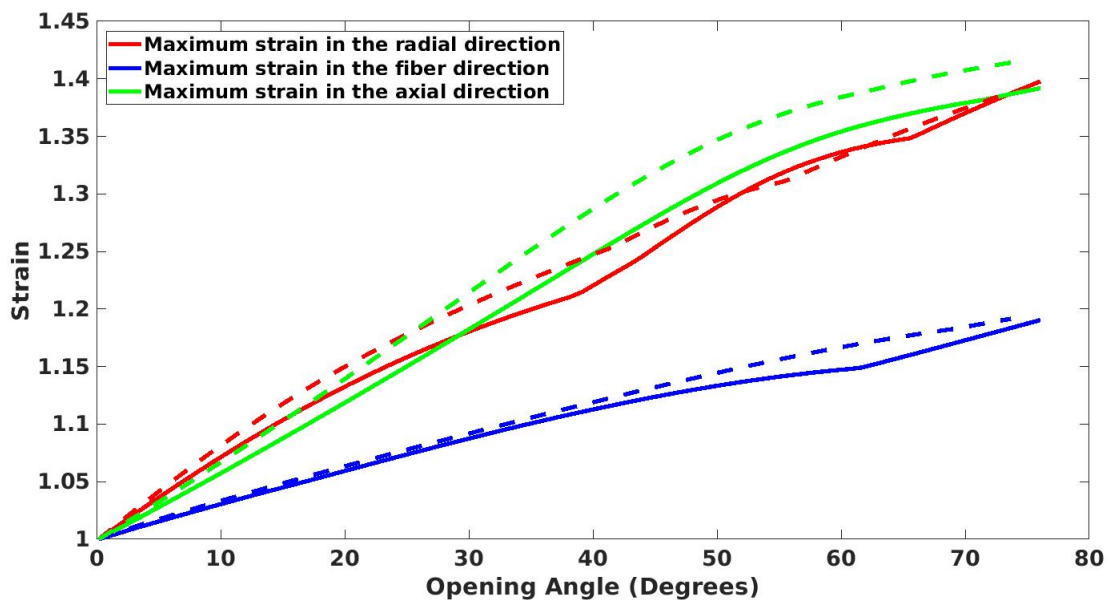


Figure 3.14: Maximum strains in radial, fiber and axial directions for anisotropic (solid) and isotropic (dashed) growth.

### 3.2 Conclusion

In this chapter, we investigated the effect of growth on residual stain. Residual strain/stress has attracted many researchers and ignoring it could lead to inaccurate predictions for when plaque caps can rupture. The opening angle is a well-known experimental method to measure the residual stress/strain. The cross sectional rings

of arteries spring open after a radial cut is made, even after excision and removing all the external loads. This attests to the existence of residual stress/strain inside load free sections. The opening angle is measured as the angle of the opened sector and there are numerous studies that estimate residual stress/strain using this angle. In our study, we used a general domain that is extracted from real IVUS images to show the effect of growth on the opening angle. With the use of fiber coordinate system, we first studied the effect of growth in a single direction on the opening angle. We noticed that growth in the fiber direction had the most significant effect on the opening angle while growth in the axial direction had the least effect. Thereafter, we compared an energetically optimal anisotropic growth acquired from displacement-growth minimization method to an isotropic growth with the same Jacobian. We observed the effect of growth for both cases by plotting the opening angle against time and stenosis. For the anisotropic case, the opening angle went from 0 to about 76 degrees when the stenosis went from 47% to about 66% and for the isotropic case it went from 0 to 73 degrees for a change of stenosis from 47% to 64%. Then we calculated the strain for both cases in the fiber coordinates direction. We realized that the strain in the fiber direction engages the whole domain while the strain in the radial and axial direction is more localized. Furthermore, the strain in the isotropic case is slightly larger than the anisotropic case which confirms the fact that the anisotropic growth is more energetically favorable. However, all of our results such as strains and the opening angle for the anisotropic growth and isotropic growth were very close. This was due to the geometry we studied. Specifically, due to the short length of the arterial cross section, our minimization scheme did not suppress the axial growth significantly which led to a growth regime that was similar to the isotropic case.

The results in this chapter can help experimentalists estimate the amount of residual strain at different stages of atherosclerosis by measuring the stenosis. The limitation for us however, was the mechanical information about the reference domain. It is rather unrealistic to assume that our already thickened domain is at zero-strain state (or starts with zero opening angle). However, there is no reason that this method

cannot be applied to a numerically pre-stressed domain.

Ruptured plaques introduce many medical challenges and they account for 55-60% of luminal thrombosis occurrences [98], when the thin fibrous cap overlying the necrotic core yields. The residual strain/stress plays an important role in determining the yield stress/strain for the fibrous cap. The findings of this study suggest that by controlling the growth in the vessel wall, one can significantly suppress the accumulation of residual strain in the arteries and possibly postpone the luminal thrombosis.

## Chapter 4

### ATHEROSCLEROSIS IN 3D WITH HISTOLOGY

In this chapter, we study the effect of growth on histology of atherosclerotic plaques with an emphasis on the formation of the necrotic core. Understanding the evolution of the necrotic core is very important in controlling and preventing acute coronary syndromes caused by ruptured plaques. During rupture a luminal thrombosis forms as a result of direct contact between platelets in the bloodstream and the thrombogenic content of necrotic core. According to an analysis on ruptured plaques, 80% of necrotic cores were larger than  $1.0 \text{ mm}^2$  and occupied more than 10% of the plaque area in 90% of lesions. In fact, in 65% of the cases, the necrotic core can occupy up to 25% of the lesion [98]. Not only does the necrotic core contribute to advanced stages of atherosclerosis such as rupture, but also its presence in earlier stages such as Thin-cap fibroatheroma and fibrous cap atheroma is significant, see Table 4.1.

Dimension	Plaque Type		
	Fibrous Cap Atheroma	Thin-cap Fibroatheroma	Acute Plaque Rupture
Necrotic Core Area ( $\text{mm}^2$ )	$1.2 \pm 2.2$	$1.7 \pm 1.1$	$3.8 \pm 5.5$
Percentage of the lesion occupied by Necrotic Core	$15 \pm 20$	$23 \pm 17$	$34 \pm 17$

Table 4.1: Size of necrotic core in advanced plaques. See pages 22 and 39 of [98] for diagrams.

In chapter 1, we illustrated the histology of atherosclerosis. In this chapter, we introduce a mathematical model that helps us simulate the dynamics of macrophages,

chemoattractants such as MCP-1, oxygen, oxidized LDLs (Ox-LDL) and the necrotic core. Even though atherosclerosis is more intricate and involves more cellular and chemical interactions, we will see that our model will produce results consistent with medical scans.

To connect the histology with the mechanical growth, we introduce a growth factor called platelet derived growth factor (PDGF). This growth factor can be produced by endothelial cells or the platelets in the bloodstream. Endothelial dysfunction or injury can stimulate endothelial cells to produce PDGF [81]. Platelets in the blood stream can attach themselves to a lesion site and release PDGF. This will promote the smooth muscle cell recruitment at the site of the injury and, as a result, growth. This chemical is also known to be responsible for directed cell movement in the arterial wall [82, 36].

Intravascular ultrasound (IVUS) imaging is a method that helps clinicians see inside the arteries. It is done via a catheter with an ultrasound transducer attached to the end of it. By sending this end to the desired location, they acquire visual data pertinent to the arterial wall. This method can provide images of the intima, media and the external elastic membrane (media-adventitia interface). This technology is even able to recognize plaque composition by doing spectral analysis on backscattered ultrasound [11]. The data gathered is later compared against the spectrum of plaques where the histology was determined independently by a clinician [67], see Figure 4.1. There are other technologies such as magnetic resonance imaging (MRI) [42], radionuclide imaging [72] and intravascular thermography [97] that can help with the detection of coronary diseases. However, we focus on IVUS images in this thesis.

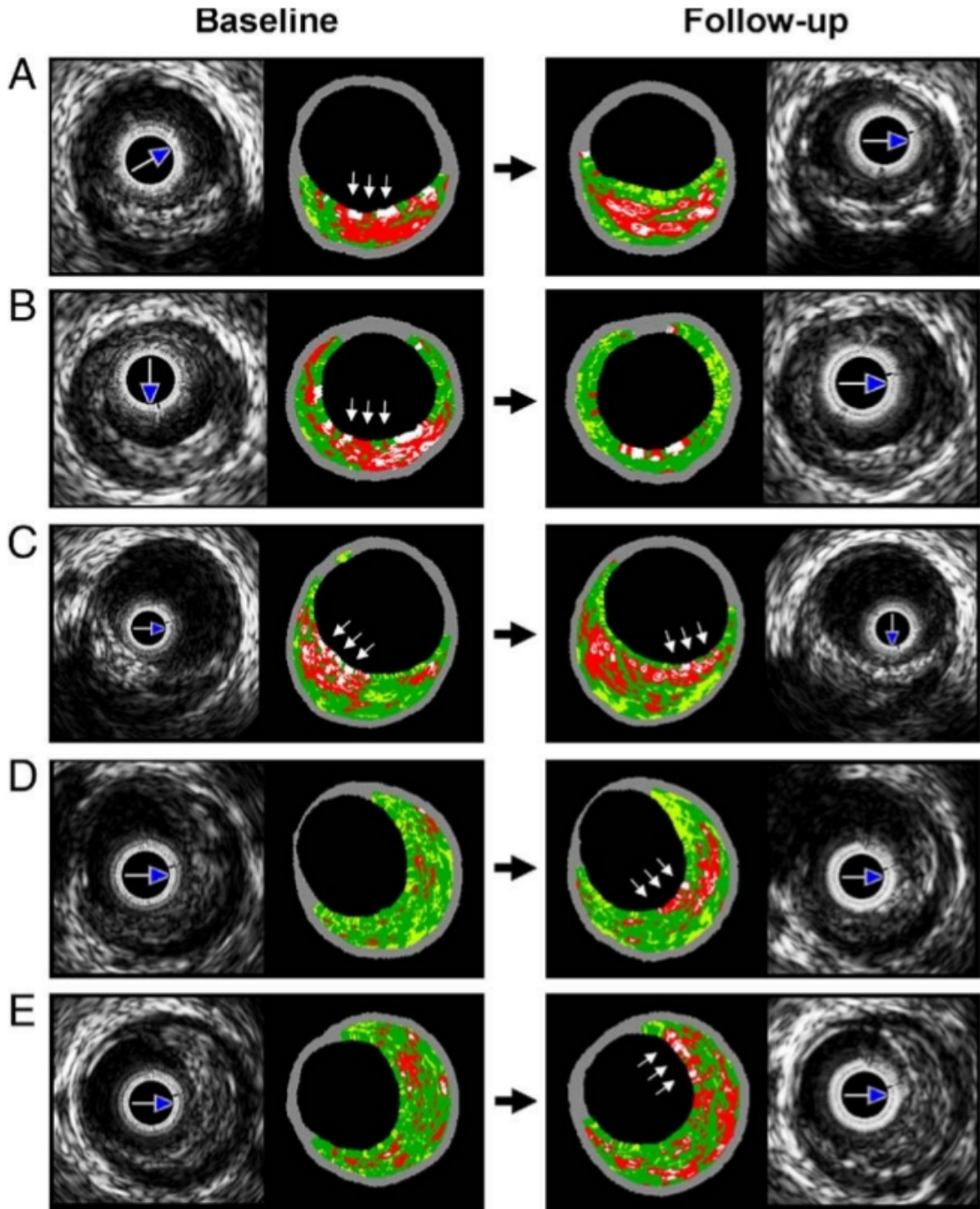


Figure 4.1: IVUS images taken from Kubo et al. 2010 [54]. The baseline and follow-up images were acquired within a year of each other. Gray scale images are the original IVUS images and the colored ones are acquired after spectrum classification of plaque structure. The red corresponds to necrotic regions and the white speckles are signs of calcification. Green shows fibrotic regions free of necrosis and calcification and yellow represents the fibrofatty regions. Blue arrows show the orientation of the catheter head. White arrows mark the location of Thin Cap Fibroatheromas (TCFA).

Despite being useful, there are some disadvantages to using IVUS. The price of a disposable catheter alone can be between \$600 and \$1000 and taking IVUS images requires an invasive procedure. These reasons coupled with the side effects patients may experience, generally, prevents doctors from acquiring multiple images. This means that there is a large time span between images and we do not have a clear picture of what is happening to the plaque during this time. Mathematical models, specifically those that take into account both the histology of the plaque and the arterial wall deformation, can help us bridge this gap.

In this chapter, we will provide a mathematical framework based on histology driven morphoelasticity to show the effect of growth on necrosis and other cell and chemical dynamics. Then we propose 4 biological mechanisms to explain the progression of plaque in each case of Figure 4.1.

## 4.1 Methods and assumptions

We work with five domains which correspond to 5 baseline domains in Figure 4.1. Refer to the appendix for more information about the method we used to create these domains. Since the IVUS images only include the intima layer for each case, similar to chapter 3<sup>1</sup>, we added medial and adventitial layers with fixed thicknesses to each domain, see Figure 4.2.

For all of our simulations, we used the same blood pressure as chapters 2,3 ( $p = 120$  mmHg). Blood pressure is the reason that some of the lumina in Figure 4.2 are larger. In other words, the computer generated domains are picked in a way that after imposing the blood pressure the result still looks fairly similar to the IVUS baselines<sup>2</sup>. However, this is not precise and some of the simulated lumen areas are larger than the ones in the IVUS images.

---

<sup>1</sup> The domain A in Figure 4.1 is the same domain we used through out chapter 3.

<sup>2</sup> IVUS images are taken *in-vivo* and in the presence of blood pressure.

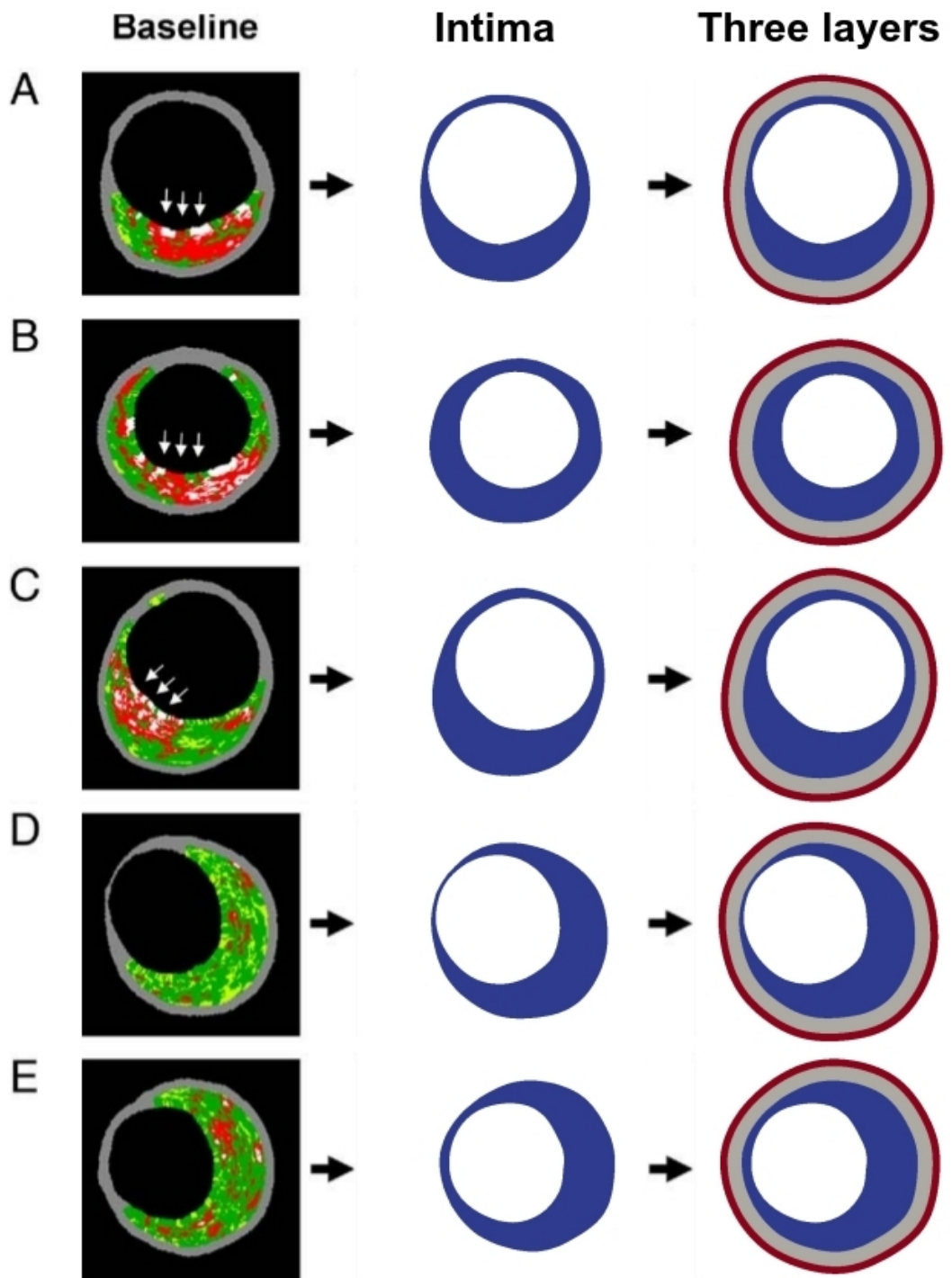


Figure 4.2: First column: IVUS images. Second and third columns: computer generated domains.

### 4.1.1 System of PDEs

Now we define a system of PDEs that governs the dynamics of macrophages, chemoattractants (such as MCP-1), oxygen and the necrotic core, see Figure 1.2. In addition, we use a combination of Gaussian functions that describes the distribution of Ox-LDLs and a separate PDE that models the distribution of PDGF. It is known that macrophages produce growth factors that contain at least two forms of PDGF [88]. Also PDGF is responsible for SMC proliferation and the intimal growth happens as a consequence of that [77, 91]. In our model, we do not consider SMCs as a separate variable. Instead, we connect the distribution of PDGF to the growth tensor directly. Theoretically, our model can expand to include more PDEs that govern more aspects of atherosclerosis but computationally it can become very costly. One solution might be the use of parallel algorithms which is a future plan for this study.

The model that we use in this thesis is

$$\frac{\partial N}{\partial t} = D_1 \Delta N + \gamma(C)M - d_1 N \quad (4.1)$$

$$\frac{\partial M}{\partial t} = D_2 \Delta M - \nabla \cdot (\chi M \nabla(L + Q)) - \gamma(C)M \quad (4.2)$$

$$\frac{\partial Q}{\partial t} = D_3 \Delta Q - d_2 Q + \lambda_1 LM \quad (4.3)$$

$$\frac{\partial C}{\partial t} = D_4 \Delta C - d_3 C - \lambda_2 CM + f(\mathbf{x}, t) \quad (4.4)$$

$$L(\mathbf{x}, t) = \sum_{i=1}^K L_i(t) \exp \left( -s_i |\mathbf{x} - \mathbf{x}_0^{(i)}(t)|^2 \right) \quad (4.5)$$

which is solved in the grown domain with the boundary conditions:

$$\frac{\partial N}{\partial \mathbf{n}_1} = 0 \quad \text{on } \partial \omega_1 \quad (4.6)$$

$$M = M_0(t) \quad \text{on } \partial \omega_1 \quad (4.7)$$

$$\frac{\partial Q}{\partial \mathbf{n}_1} = 0 \quad \text{on } \partial \omega_1 \quad (4.8)$$

$$C = C_0(t) \quad \text{on } \partial \omega_1 \quad (4.9)$$

$$(4.10)$$

$$\frac{\partial N}{\partial \mathbf{n}_2} = 0 \quad \text{on } \partial\omega_2 \quad (4.11)$$

$$\frac{\partial M}{\partial \mathbf{n}_2} = \kappa M \quad \text{on } \partial\omega_2 \quad (4.12)$$

$$\frac{\partial Q}{\partial \mathbf{n}_2} = 0 \quad \text{on } \partial\omega_2 \quad (4.13)$$

$$\frac{\partial C}{\partial \mathbf{n}_2} = 0 \quad \text{on } \partial\omega_2 \quad (4.14)$$

where  $N, M, Q, C$  correspond to the density of necrosis, macrophages, chemoattractants and oxygen respectively. Constants  $D_1 - D_4$  are their diffusivities,  $d_1-d_3$  are decay rates,  $\chi$  is the chemotactic coefficient for macrophages,  $\lambda_1$  is the rate of production of chemoattractants as a result of Ox-LDL consumption by macrophages and  $\lambda_2$  is the rate at which macrophages consume oxygen. We denote the endothelium and IEL by  $\partial\omega_1$  and  $\partial\omega_2$  respectively and let  $\mathbf{n}_1$  and  $\mathbf{n}_2$  represent their outward unit normal vectors, see Figure 4.5. The parameter  $\kappa$  is the rate of outflux of macrophages through boundary  $\partial\omega_2$ . The function  $f(\mathbf{x}, t)$  corresponds to sources of oxygen within the intima at the point  $\mathbf{x} = (x, y, z)$ . This models the development of vasa vasora which we will elaborate on. We assume the dynamics of (4.1)-(4.4) is very fast but the dynamics in (4.5), (4.7), (4.9) and  $f(\mathbf{x}, t)$  is slow in comparison. The time scale for relaxation to mechanical equilibrium is also assumed to be very short. Therefore, we solve equations (4.1)-(4.4) to steady state and we do not provide any initial conditions. For information about the values of  $f(\mathbf{x}, t)$ ,  $L_i(t)$ ,  $s_i$ ,  $\mathbf{x}_0(t)$ ,  $M_0(t)$  and  $C_0(t)$  and all the other parameters see Tables 4.2-4.6 and 4.7.

Equation (4.5) is given in terms of Gaussians to give the author freedom in changing the level and location of Ox-LDLs. The first terms on the right hand side of equations (4.1)-(4.4) model the diffusion of their corresponding variable. The second term in (4.1) and the last term in (4.2) relate the death of macrophages to the formation of the necrotic core. The rate of death is  $\gamma(C)$  which is a function of  $C$  given by

$$\gamma(C) = \gamma_{min} + (\gamma_{max} - \gamma_{min}) \left( \frac{C_{crit}^m}{C_{crit}^m + C^m} \right), \quad (4.15)$$

where  $m$  is the Hill coefficient and  $C_{crit}$  is a parameter that determines the resilience

of macrophages to low arterial oxygen tension<sup>3</sup>. Equation (4.15) models the death of macrophages due to hypoxia<sup>4</sup> [24]. The normoxic death rate  $\gamma_{min}$  is the death rate for macrophages in an oxygen-sufficient environment and  $\gamma_{max}$  is the hypoxic death rate in an oxygen-limited environment. It has been observed that oxygen saturation in the intima plays an essential role in progression of atherosclerotic plaques [48, 90]. Because oxegyn is significantly consumed by many cells (including tissue cells and macrophages), oxygen distribution is not deeply diffused in the intima. Bjornheden et al. show that tissue hypoxia is present in deep portions of the atherosclerotic plaque [8], see Figure 4.3. By solving equations (4.1)-(4.4) on a thin (intimal thickness  $< 30 \mu\text{m}$ ) and thick (intimal thickness  $> 30 \mu\text{m}$ ) domain, we were able to show regions of necrosis form when local intimal thickness is more than  $30 \mu\text{m}$  (the diffusive lengthscale of molecular oxygen) and macrophage density in the intima is larger than about  $10^5 \text{ cells/cm}^3$ , see Figure 4.4.

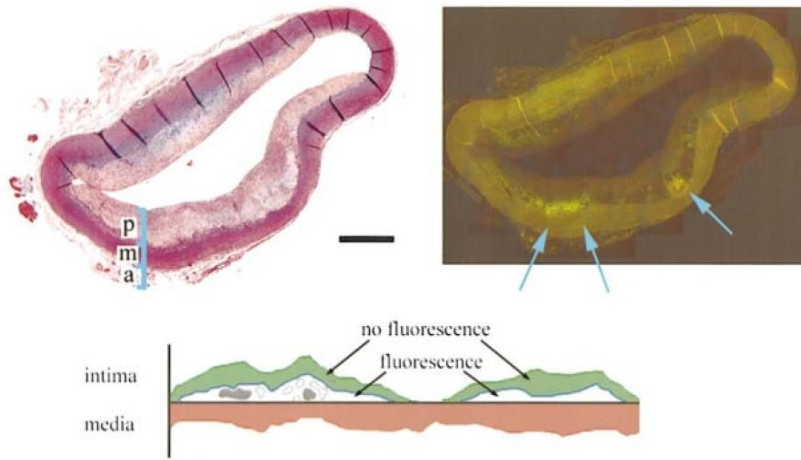


Figure 4.3: Arrows show the areas with the most intense fluorescence, indicating the presence of NITP, a marker of hypoxia, [8].

We consider equations (4.1)-(4.4) to be in steady state. This is because the

---

<sup>3</sup> Partial pressure of oxygen in arteries is directly related to oxygenation.

<sup>4</sup> Hypoxia in atherosclerosis pertains to the death of cells such as macrophages due to lack of oxygen.

PDEs have to be solved at each mechanical growth step and the timescale for mechanical growth of the domain is much larger than the timescale of cell and chemical dynamics. Also atherosclerotic processes such as changes in Ox-LDL density (governed by equation (4.5)), inflammation ( $M_0(t)$ ), oxygenation ( $C_0(t)$ ) and formation of vasa vasora<sup>5</sup> ( $f(\mathbf{x}, t)$ ) are chronic events, occurring very slowly over many years or decades, [5, 57, 65].

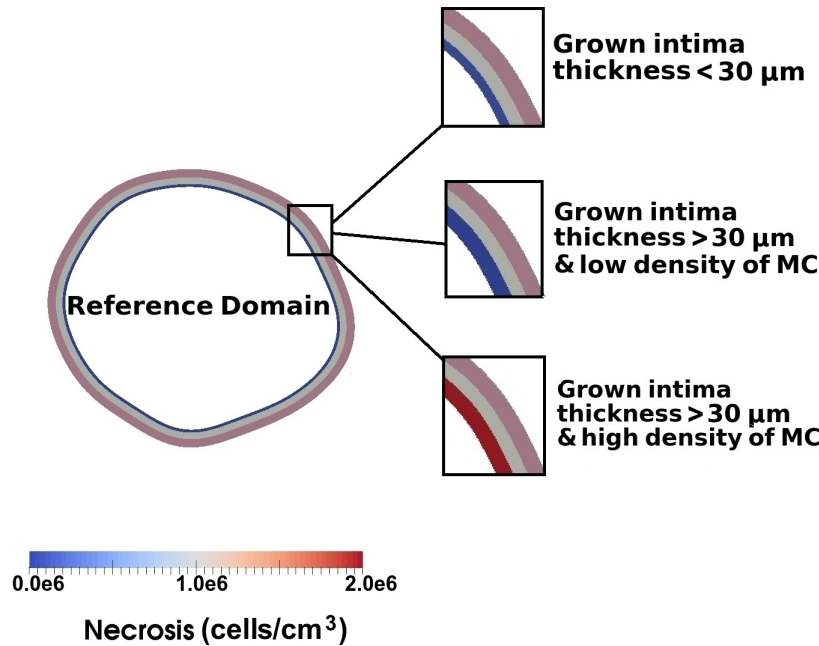


Figure 4.4: (MC = Macrophage Cells). A simulation showing the effect of macrophage density and intima thickness on necrosis. The parameters used for this simulation are similar to the parameters from case B in Table 4.7 except low density of MC corresponds to  $M_0(t) = 4.6 \times 10^3 \text{ cells}/\text{cm}^3$  and high density of MC corresponds to  $M_0(t) = 4.6 \times 10^5 \text{ cells}/\text{cm}^3$ . We have manually changed the thickness of the domain to show the effect of intimal thickening on necrosis.

*Top:* No necrosis in the intima with thickness  $< 30 \mu\text{m}$  and macrophage density  $10^5 \text{ cells}/\text{cm}^3$ . *Middle:* No necrosis in the intima with thickness  $> 30 \mu\text{m}$  and macrophage density  $< 10^5 \text{ cells}/\text{cm}^3$ . *Bottom:* Necrotic intima with thickness  $> 30 \mu\text{m}$  and macrophage density  $> 10^5 \text{ cells}/\text{cm}^3$ .

---

<sup>5</sup> Vasa vasora are small microvessels inside the walls of thick arteries which provide oxygen and nutrition supplies for the arterial wall.

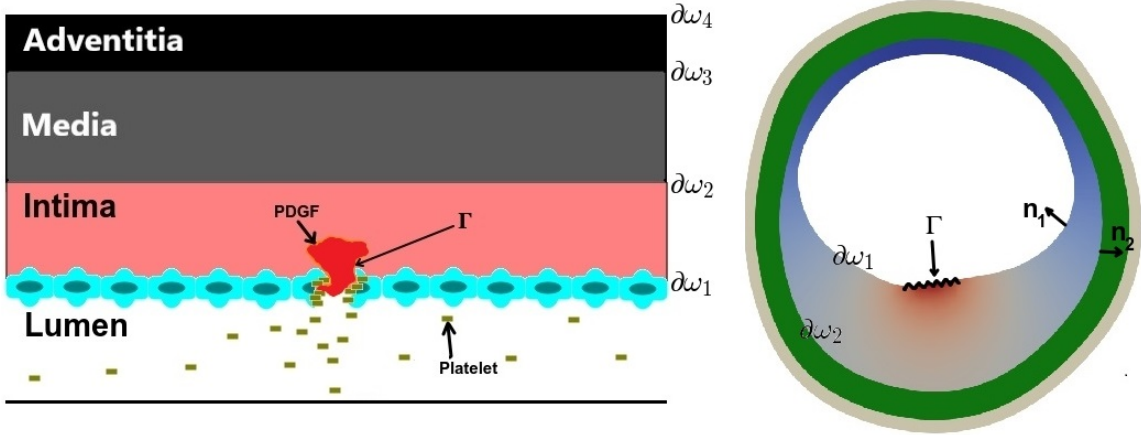


Figure 4.5: PDGF produced by platelets of endothelial cells promote cell proliferation at the site of an injury or endothelial dysfunction.

#### 4.1.2 PDGF equation

For the distribution of PDGF, we use a separate PDE. The decoupling of the PDGF from the rest of the cells and chemicals is done to reduce the computation time. We consider a simple PDE for the distribution of PDGF which is solved in the grown domain:

$$\frac{\partial P}{\partial t} = D_5 \Delta P - d_4 P \quad (4.16)$$

where  $D_5$  is the diffusivity and  $d_4$  is the natural decay rate of PDGF. We use the following Dirichlet boundary conditions:

$$P = \begin{cases} P_0 & \text{On } \Gamma \subset \partial\omega_1 \\ 0 & \text{On } \partial\omega_1 \setminus \Gamma \end{cases} \quad (4.17)$$

where  $\partial\omega_1$  is the endothelium and  $\Gamma$  is the part of it which is dysfunctional or injured. PDGF can be produced by the endothelial cells or by platelets from the bloodstream that attach themselves to the site of injury, see Figure 4.5.

Like the other PDEs, equation (4.16) will be solved for the steady state, using the parameters in Table 4.7. After solving (4.16) in steady state, we define:

$$g_k = \exp \left( \alpha_k \int_0^t \frac{P^m}{P^m + P_0^m} dt' \right) \quad (4.18)$$

where  $\alpha_1 = 1$ ,  $\alpha_2 = 0.25$ ,  $m = 4$  and  $P_0 = 1.12 \times 10^{-5}$  mol/L (these constants were chosen for convenience). Then we will have the growth tensor in the fiber coordinate system defined as

$$\mathbf{G} = \begin{bmatrix} g_1 & 0 & 0 \\ 0 & g_2 & 0 \\ 0 & 0 & 1 \end{bmatrix} \quad (4.19)$$

We have decided to neglect the growth in the axial direction, because IVUS images which we aim to recreate are cross sections of the artery.

Using PDGF to construct the growth tensor is very subtle. In chapter 1, we mentioned that the growth tensor is always applied to the reference domain in order to satisfy the morphoelasticity requirement (1.4) and incremental growth is only possible if growth tensors can commute with the elastic tensors (which does not generally happen in our case). This can cause a problem, since the arterial wall is always grown with respect to the reference domain but equation (4.16) must be solved in the deformed domain. To overcome this issue, we first solve the PDGF equation to get the distribution in the deformed domain. Suppose the deformation vector field is  $\varphi(X, Y, Z)$ . Then the map  $\varphi^{-1}(x, y, z)$  imposed on the deformed domain will give us the reference domain. Next, we map the distribution of PDGF in each tetrahedron (triangle if in 2D) to a tetrahedron in the reference domain with the same cell index. This way, we will have a spatially dependent PDGF distribution in the reference domain that we can use to update (4.19) at each time.

Now that we have a growth tensor, we can set up the mechanical problem in the same way as chapter 3. Similarly, we find a  $\mathbf{u} \in C^2(\Omega)$  such that

$$\sum_{i=1}^3 \iiint_{\Omega_i} \left( J_{g_i} \frac{\partial W_i}{\partial \mathbf{F}_{e_i}} \mathbf{G}_i^{-T} : \nabla \mathbf{v} \right) dV + p \iint_A J \mathbf{F}^{-T} N_1^{(1)} \mathbf{v} dS = 0 \quad \forall \mathbf{v} \in C^2(\Omega) \quad (4.20)$$

and we solve (4.1)-(4.4) and (4.16) in the deformed domain for each growth time step. All of the tensors, vectors and constants are defined similar to those in chapter 3. Figure 4.6 shows a sketch of our algorithm.

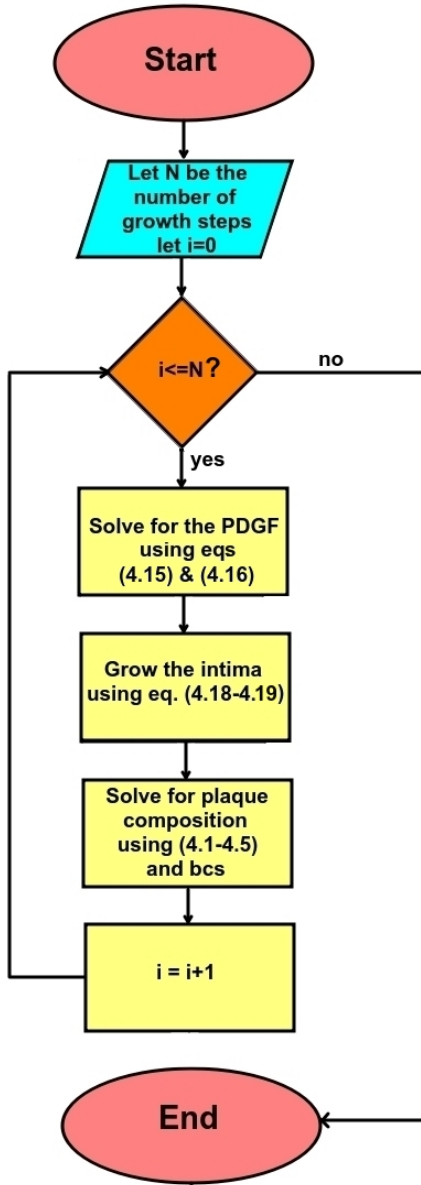


Figure 4.6: Flowchart of our algorithm.

## 4.2 Mechanisms

Before presenting the results, we discuss 4 mechanisms that pertain to the parameters in our problem. Although many factors are involved in producing the outcomes from Kubo's IVUS images, here, we focus on the following:

1. **Changes in Ox-LDL distribution,**  $L_0(t)$ ,  $\mathbf{x}_0(t)$ : It has long been hypothesized that modified LDLs are atherogenic, since they are mainly responsible for the appearance of the foam cell phenotype [12]. The Ox-LDL density and location inside a plaque are governed by (4.5) whose time evolution we control directly in the model.
2. **Changes in inflammation,**  $M_0(t)$ : We define inflammation in the endothelium as the density of macrophages adsorbed on the layer. Mathematically, we control this density by the Dirichlet boundary condition (4.7). Biologically, an increasing  $M_0(t)$  corresponds to an endothelium that becomes more inflamed over time.
3. **Development of vasa vasora,**  $f(\mathbf{x}, t)$ : Vasa vasora are a network of small vessels that supply the arterial walls with resources such as oxygen and glucose. Sources of oxygen are controlled in our model through the function  $f(\mathbf{x}, t)$  in equation (4.4).
4. **Increasing oxygenation,**  $C_0(t)$ : We use this mechanism in only one case. Arterial oxygenation can depend on intercirculatory mixing, hemoglobin concentration and other systemic factors [61]. For example, exercise can increase the blood flow to the tissues and hemoglobin concentration [9] and it has been shown to increase arterial oxygenation in patients with chronic heart failure [43, 83]. We control  $C_0(t)$  using the Dirichlet boundary condition (4.9).

For information about the values of the functions corresponding to each mechanism see Tables 4.2-4.6. To mimic the outcome of an IVUS image, we use thresholding, see Figure 4.7.

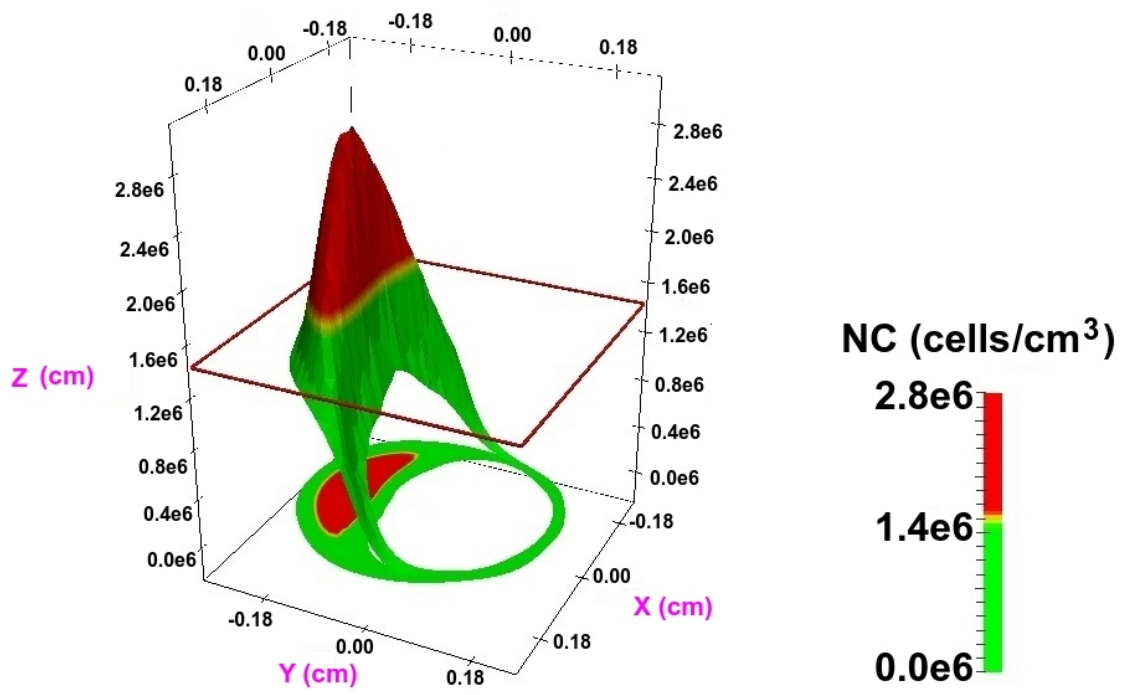


Figure 4.7: Threshold value  $1.4 \times 10^6$  cells/cm<sup>3</sup> represented by a plane. Densities above this value (above the plane) are considered necrotic.

#### 4.2.1 Case A

In this case, we try to match Figure 4.1 (A) qualitatively. Kubo et al. describes this case as transition from Thin Cap FibroAtheroma (TCFA) to Thick cap FibroAtheroma (ThCFA). One can see that the follow up state in 4.1 (A) has a thicker layer overlying the necrotic core. Figures 4.8 and 4.9 show the result of our simulations in baseline and follow-up states. Also the mesh is added to show the effect of PDGF on the element size.

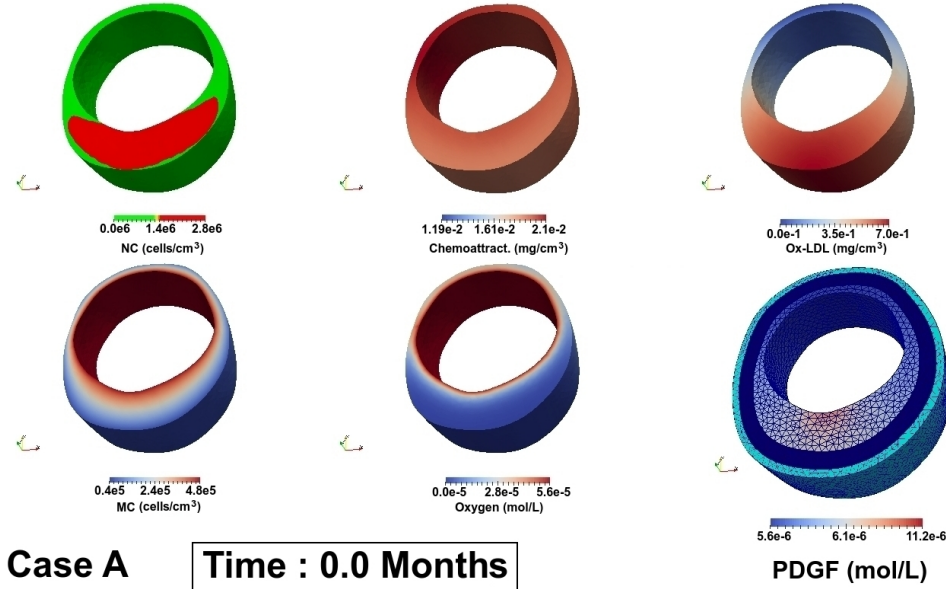


Figure 4.8: Typical 3D plaque model results. Baseline concentrations of NC, Chemoattractant, oxLDL, MC and and oxygen are outputted as spatially dependent fields distributed in the intima. For PDGF concentration, the media and adventitia are also indicated along with the finite element mesh.

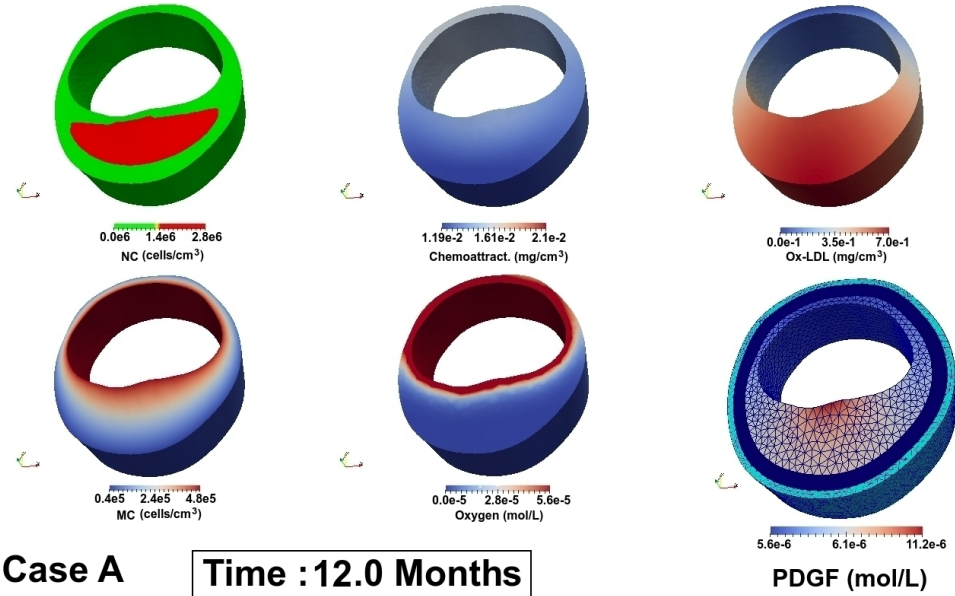


Figure 4.9: Typical 3D plaque model results. Follow-up concentrations of NC, Chemoattractant, oxLDL, MC and and oxygen are outputted as spatially dependent fields distributed in the intima. For PDGF concentration, the media and adventitia are also indicated along with the finite element mesh. See tables 4.2 - 4.7 for parameter values.

For better comparison, Figure 4.10 shows the cross section at  $Z = 0$  for the necrotic core in the baseline and follow-up state. We can see that in our simulation, TCFA has turned into ThCFA. These results are acquired using mechanisms 2 and 4. The inflammation is increasing and the macrophages chemotax towards sources of Ox-LDL and chemokine. But the intima close to the lumen is getting more oxygenated, see Figure 4.9. More oxygen in the intima will reduce the macrophage death from hypoxia and therefore, NC will be more isolated from the lumen. See Table 4.2 for the values of the time dependent parameters for this case.

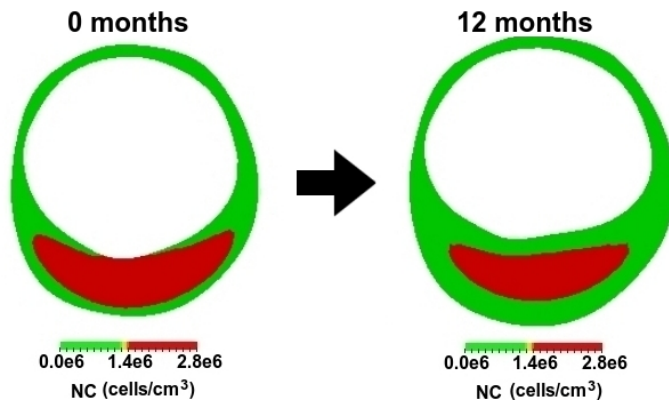


Figure 4.10: Necrotic core in baseline and follow-up state for the intimal cross section at  $Z = 0$ .

Function	Meaning	Value	Units
$L(x, y, z)$	Distribution of Ox-LDL	$2 \exp [-0.05 (x^2 + (y + 1.3)^2 + z^2)]$	mg/cm <sup>3</sup>
$M_0(t)$	Macrophage density in endothelium	Linear in $t$ and increases from $4.60 \times 10^5$ to $4.64 \times 10^5$	cells/cm <sup>3</sup>
$C_0(t)$	Oxygen Boundary Condition	Linear in $t$ and increases from $5.6 \times 10^{-5}$ to $11.2 \times 10^{-5}$	mol/L
$f(x, y, z)$	Oxygen Sources within intima	0	mol/L/day

Table 4.2: Time-dependent parameters for Case A. The time variable  $t$  changes from 0 to 12 months.

### 4.2.2 Case B

From now on, we focus on the 2D cross sections. Kubo et al. explains Figure 4.1 (B) as a TCFA that turns into a fibrous plaque. For our simulations, we assumed that the injury has been healed and the LDLs infiltration reduces in time ( $L_0(t)$  goes from 0.7 to 0). Consequently, the concentration of Ox-LDL will decrease. This will result in less macrophages entering the intima. All of these dynamics lead to a vanishing NC, see Figures 4.11 and 4.12. In summary, we used mechanisms 1 and 2. However, our model is unable to capture the thinning of the intima. We believe for such an outcome, one needs to consider the NC as a separate mechanical domain with its own mechanical properties. See Table 4.3 for the values of the time dependent parameters for this case.

Function	Meaning	Value	Units
$L(x, y, t)$	Distribution of Ox-LDL	$\left(0.7 - \frac{0.7t}{12}\right) \exp[-0.14((x - 0.1)^2 + (y + 1.2)^2)]$	mg/cm <sup>3</sup>
$M_0(t)$	Macrophage density in endothelium	Linear in $t$ and decreases from $5.2 \times 10^5$ to $1.2 \times 10^5$	cells/cm <sup>3</sup>
$C_0$	Oxygen Boundary Condition	$5.6 \times 10^{-5}$	mol/L
$f(x, y)$	Oxygen Sources within intima	0	mol/L/day

Table 4.3: Time-dependent parameters for Case B. The time variable  $t$  changes from 0 to 12 months.

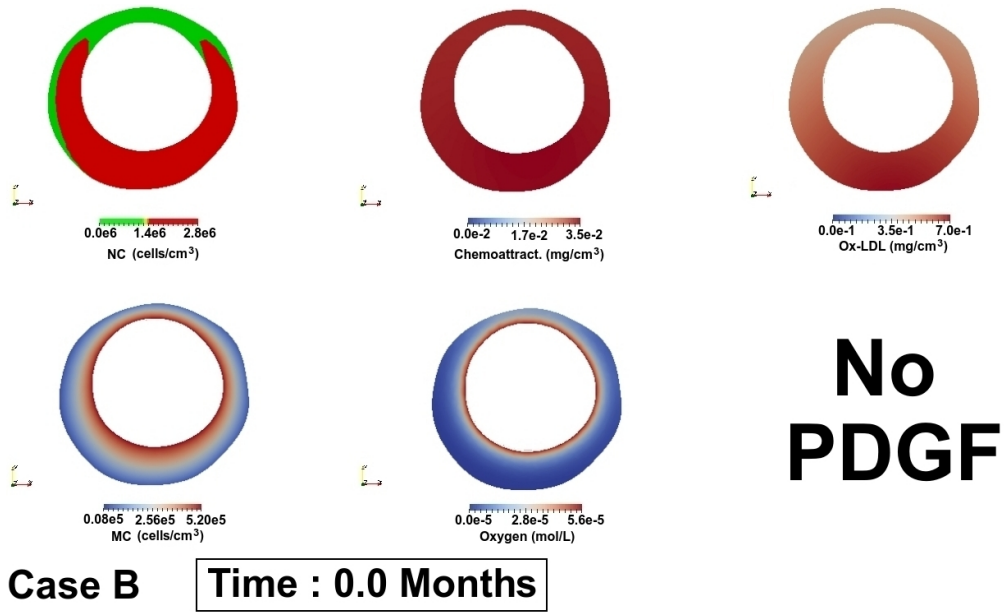


Figure 4.11: Typical 2D plaque model results. Baseline concentrations of NC, Chemoattractant, oxLDL, MC and and oxygen are outputted as spatially dependent fields distributed in the intima. No PDGF concentration has been considered for this case.

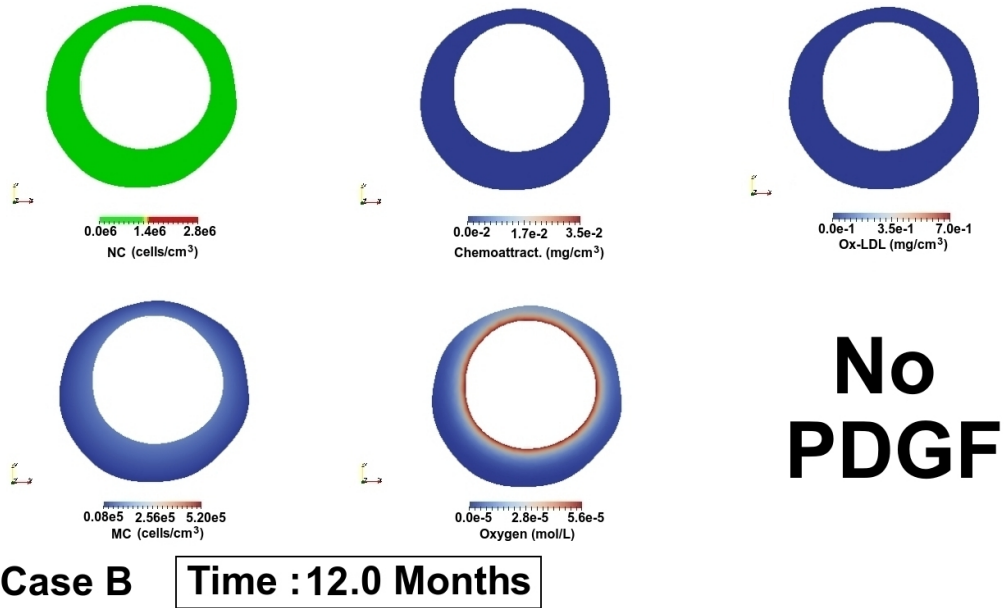


Figure 4.12: Typical 2D plaque model results. Follow-up concentrations of NC, Chemoattractant, oxLDL, MC and and oxygen are outputted as spatially dependent fields distributed in the intima. PDGF is absent for this case. See tables 4.3-4.7 for parameter values.

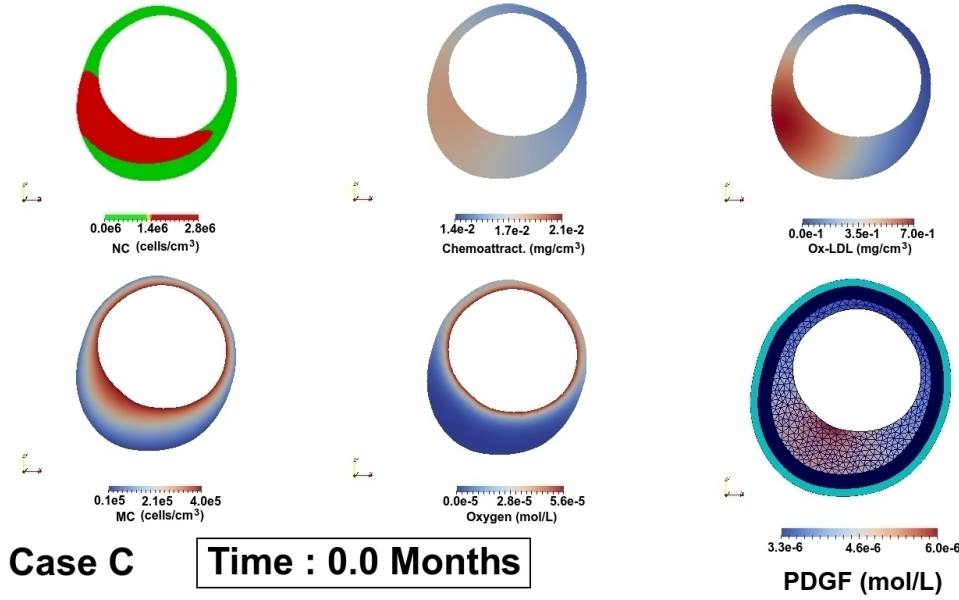


Figure 4.13: Typical 2D plaque model results. Baseline concentrations of NC, Chemoattractant, oxLDL, MC and and oxygen are outputted as spatially dependent fields distributed in the intima. For PDGF concentration, the media and adventitia are also indicated along with the finite element mesh.

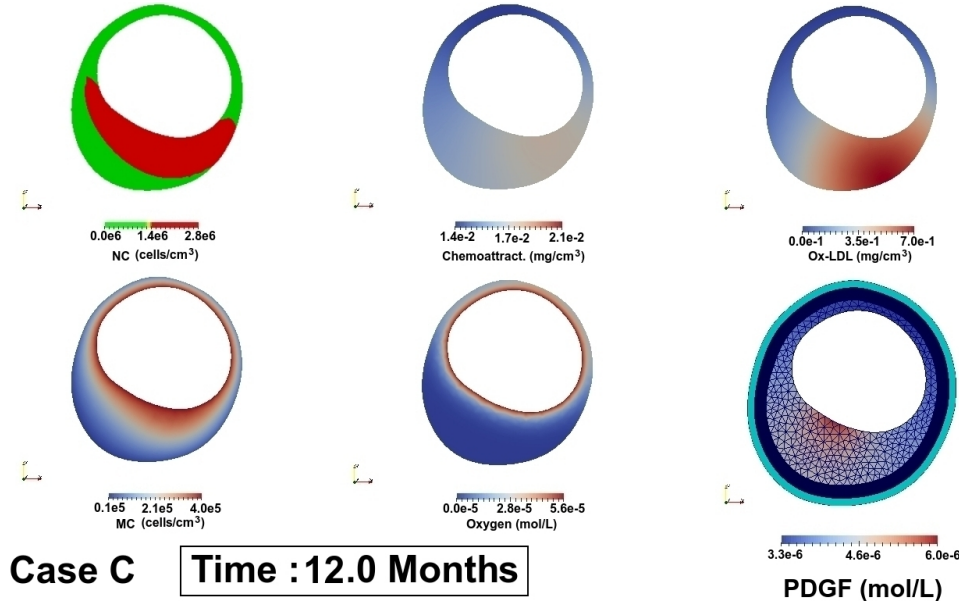


Figure 4.14: Typical 2D plaque model results. Follow-up concentrations of NC, Chemoattractant, oxLDL, MC and and oxygen are outputted as spatially dependent fields distributed in the intima. For PDGF concentration, the media and adventitia are also indicated along with the finite element mesh. See tables 4.4-4.7 for parameter values.

### 4.2.3 Case C

Kubo et al. describes this case as a TCFA remaining unchanged, although the location of the necrotic core in contact with the lumen changes. The arrows in Figure 4.1 (C) show the locations of TCFAs. We only use mechanism 1 to mimic this behavior. By changing  $\mathbf{x}_0(t)$  from equation (4.5), we can change the location of Ox-LDL concentration. This will cause macrophage chemotaxis to change direction accordingly which will result in the movement of NC, see Figures 4.13 and 4.14. There are also corresponding changes in chemoattractant and macrophage density. See Table 4.4 for the values of the time dependent parameters for this case.

Function	Meaning	Value	Units
$L(x, y, t)$	Distribution of Ox-LDL	$\exp \left[ -0.7 \left( \left( x + 0.9 - \frac{21t}{20} \right)^2 + \left( y + 0.5 - \frac{t}{20} \right)^2 \right) \right]$	mg/cm <sup>3</sup>
$M_0$	Macrophage density in endothelium	$4 \times 10^5$	cells/cm <sup>3</sup>
$C_0$	Oxygen Boundary Condition	$5.6 \times 10^{-5}$	mol/L
$f(x, y)$	Oxygen Sources within intima	0	mol/L/day

Table 4.4: Time-dependent parameters for Case C. The time variable  $t$  changes from 0 to 12 months.

### 4.2.4 Case D

Case D has been described as Pathological Intimal Thickening (PIT) transitioning into TCFA by Kubo et al. Figure 4.1 (D) shows a thickened intima at the baseline state free from NC. In the follow-up state a scythe shaped NC appears close to the lumen. Our simulations use mechanisms 1 and 2. The Ox-LDL concentration follows a combination of Gaussians with increasing density. The location of Gaussians was chosen in order to resembel the scythe shaped necrosis in 4.1 (D). Since there is no Ox-LDL in the baseline state, most of the fields are zero, see Figure 4.15. The inflammation naturally increases in time as a response to Ox-LDL increase. There are low levels

of oxygen throughout the intima and PDGF concentrations are maximal at 1 and 7 o'clock. This growth regime introduced some convergence issues and we had to increase the number of elements. Figure 4.16 shows the follow-up state to our simulation. The NC appears in a scythe shape with a TCFA from 3 to 5 o'clock. The distributions of Ox-LDL and macrophages are similar due to the macrophage chemotaxis which results in a scythed shaped NC. Regions of the intima with more macrophages have lower levels of oxygen which corresponds to the consumption of oxygen by macrophages. For this case  $L(t)$  is the sum of Gaussian functions:

$$L(x, y, t) = \sum_{i=1}^{10} L_i(t) \exp \left( -s_i \left( (x - x_0^{(i)})^2 + (y - y_0^{(i)})^2 \right) \right) \quad (4.21)$$

Refer to Appendix B (Table B.1) for the values of  $L_i(t), s_i$  and  $(x_0^{(i)}, y_0^{(i)})$ . For the values of the rest of time dependent parameters for this case, See Table 4.5.

Function	Meaning	Value	Units
$L(x, y, t)$	Distribution of Ox-LDL	See eq. (4.21) and Appendix B	mg/cm <sup>3</sup>
$M_0(t)$	Macrophage density in endothelium	Linear in $t$ and increases from 0 to $1.7 \times 10^5$	cells/cm <sup>3</sup>
$C_0$	Oxygen Boundary Condition	N/A	mol/L
$f(x, y)$	Oxygen Sources within intima	6.7	mol/L/day

Table 4.5: Time-dependent parameters for Case D. The time variable  $t$  changes from 0 to 12 months.

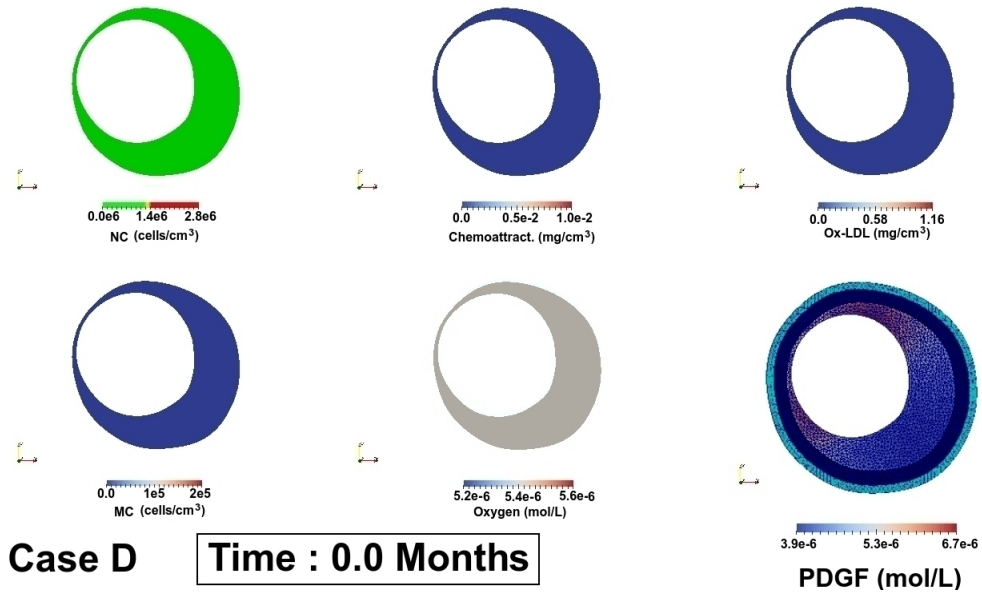


Figure 4.15: Typical 2D plaque model results. Baseline concentrations of NC, Chemoattractant, oxLDL, MC and and oxygen are outputted as spatially dependent fields distributed in the intima. For PDGF concentration, the media and adventitia are also indicated along with the finite element mesh.

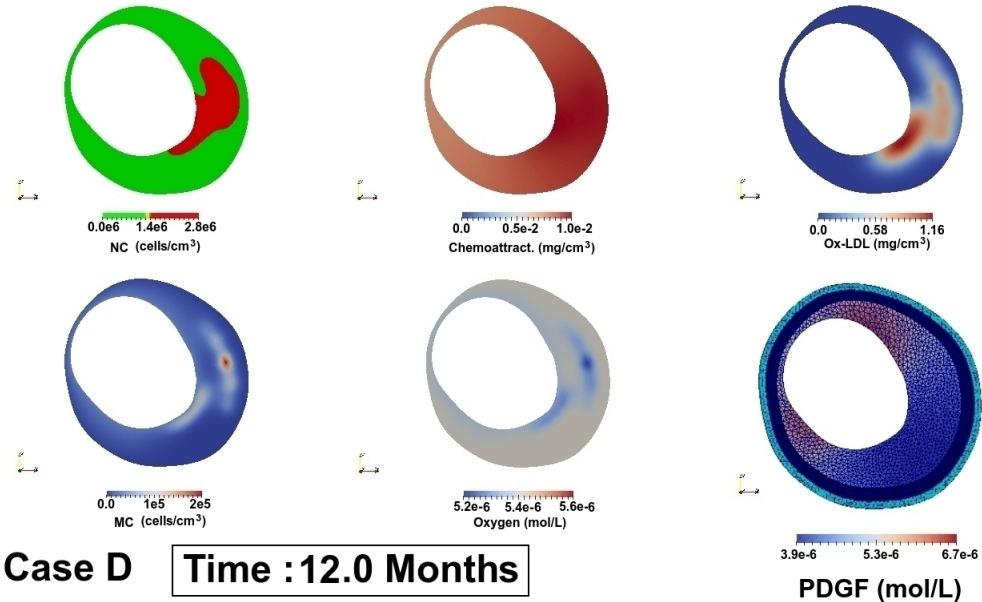


Figure 4.16: Typical 2D plaque model results. Follow-up concentrations of NC, Chemoattractant, oxLDL, MC and and oxygen are outputted as spatially dependent fields distributed in the intima. For PDGF concentration, the media and adventitia are also indicated along with the finite element mesh. See tables 4.5-4.7 for parameter values.

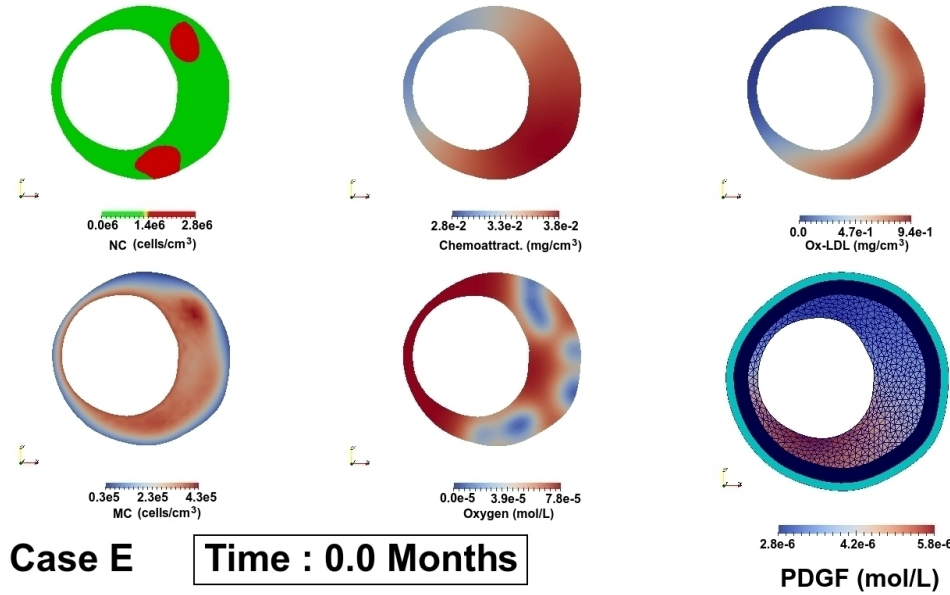


Figure 4.17: Typical 2D plaque model results. Baseline concentrations of NC, Chemoattractant, oxLDL, MC and and oxygen are outputted as spatially dependent fields distributed in the intima. For PDGF concentration, the media and adventitia are also indicated along with the finite element mesh.

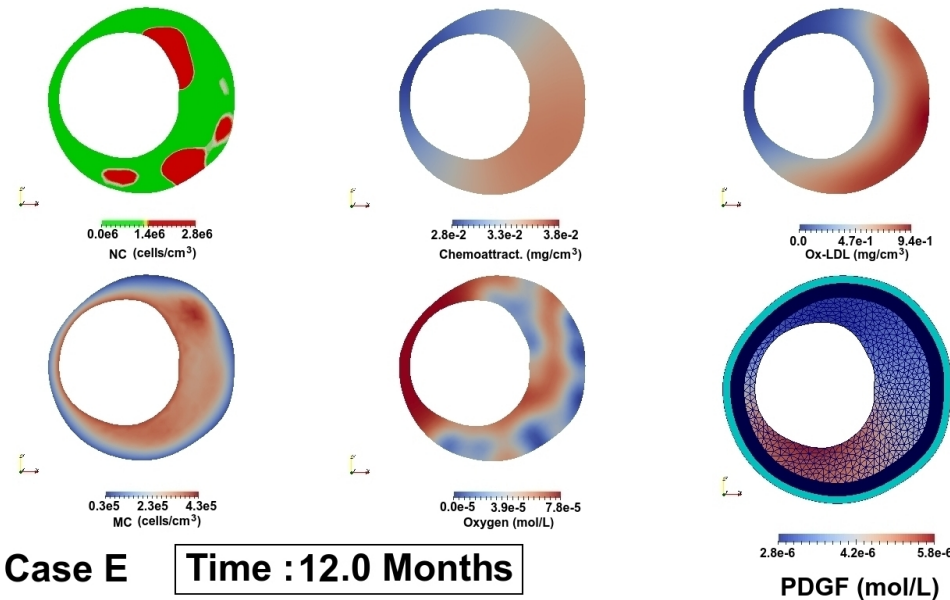


Figure 4.18: Typical 2D plaque model results. Follow-up concentrations of NC, Chemoattractant, oxLDL, MC and and oxygen are outputted as spatially dependent fields distributed in the intima. For PDGF concentration, the media and adventitia are also indicated along with the finite element mesh. See tables 4.6-4.7 for parameter values.

#### 4.2.5 Case E

Finally, case E from Figure 4.1 is described as ThCFA becoming TCFA. The largest NC densities in the baseline state at 2 o'clock and 5 o'clock show some separation from the lumen. In the follow-up state however, we can see a TCFA at 1 to 2 o'clock. For our simulations, we use mechanism 4. The Ox-LDL distribution is given by a combination of Gaussians and there are oxygen sources in the intima (due to vasa vasora), see Figures 4.17 and 4.18. If it was not for vasa vasora, oxygen would have been consumed quickly inside of the intima. The distribution of macrophages is affected by the location of Ox-LDL. For this case, both functions  $L(x, y)$  and  $f(x, y, t)$  are given by:

$$L(x, y) = \sum_{i=1}^5 L_i \exp \left( -3 \left( (x - x_0^{(i)})^2 + (y - y_0^{(i)})^2 \right) \right) \quad (4.22)$$

$$f(x, y, t) = \sum_{j=1}^{21} f_j(t) \exp \left( -s_j \left( (x - x_1^{(j)})^2 + (y - y_1^{(j)})^2 \right) \right) \quad (4.23)$$

Refer to Appendix B (Table B.2) for the values of  $L_i$ ,  $f_j(t)$ ,  $s_i$ ,  $(x_0^{(i)}, y_0^{(i)})$  and  $(x_1^{(j)}, y_1^{(j)})$ . Less chemoattractant in the follow-up state is due to the decrease in the number of macrophages as a result of hypoxia. The PDGF window is located at 6 o'clock. The necrotic core appears at 1 to 2 o'clock adjacent to the lumen similar to the IVUS image. For the values of the rest of time dependent parameters for this case, see Table 4.6.

Function	Meaning	Value	Units
$L(x, y)$	Distribution of Ox-LDL	See eq. (4.22) and Appendix B	mg/cm <sup>3</sup>
$M_0$	Macrophage density in endothelium	$4.2 \times 10^5$	cells/cm <sup>3</sup>
$C_0$	Oxygen Boundary Condition	N/A	mol/L
$f(x, y, t)$	Oxygen Sources within intima	See eq. (4.23) and Appendix B	mol/L/day

Table 4.6: Time-dependent parameters for Case E. The time variable  $t$  changes from 0 to 12 months.

Symbol	Meaning	Case A	Case B	Case C	Case D	Case E	Units
$\mu$	Chemotactic coefficient of MCs	2.26	7.77	4.41	9.17	6.02	(mm <sup>2</sup> /day) × (cm <sup>3</sup> /mg)
$D_1$	Diffusivity of NCs	$3.2 \times 10^{-3}$	$3.3 \times 10^{-3}$	$3.6 \times 10^{-3}$	$3.9 \times 10^{-3}$	$4.3 \times 10^{-3}$	cm <sup>2</sup> /day
$D_2$	Diffusivity of MCs	1.72	1.74	1.92	2.06	2.30	cm <sup>2</sup> /day
$D_3$	Diffusivity of chemoattractants	80.8	81.6	89.7	96.3	107.6	cm <sup>2</sup> /day
$D_4$	Diffusivity of O <sub>2</sub>	172.5	174.3	191.6	205.8	229.9	cm <sup>2</sup> /day
$D_5$	Diffusivity of PDGF	19.4	0	32.3	15.4	21.5	cm <sup>2</sup> /day
$d_1$	Clearance rate of NCs	0.1	0.1	0.1	0.1	0.1	day <sup>-1</sup>
$d_2$	Clearance rate of chemoattractants	10	10	10	10	10	day <sup>-1</sup>
$d_3$	Background O <sub>2</sub> consumption rate	$1.2 \times 10^4$	$1.2 \times 10^4$	$1.2 \times 10^4$	$1.2 \times 10^4$	$1.2 \times 10^4$	day <sup>-1</sup>
$d_4$	Decay rate of PDGF	2	0	2	2	2	day <sup>-1</sup>
$\lambda_1$	Production rate of chemoattractants	$2.5 \times 10^{-6}$	$2.5 \times 10^{-6}$	$2.5 \times 10^{-6}$	$2.5 \times 10^{-6}$	$2.5 \times 10^{-6}$	cm <sup>3</sup> /day
$\lambda_2$	Consumption rate of O <sub>2</sub> by MCs	$2.5 \times 10^{-7}$	$2.5 \times 10^{-7}$	$2.5 \times 10^{-7}$	$2.5 \times 10^{-7}$	$2.5 \times 10^{-7}$	cm <sup>3</sup> /day
$\gamma_{min}$	Normoxic MC death rate	$3 \times 10^{-3}$	$3 \times 10^{-3}$	$3 \times 10^{-3}$	$3 \times 10^{-3}$	$3 \times 10^{-3}$	day <sup>-1</sup>
$\gamma_{min}$	Hypoxic MC death rate	1.2	1.2	1.2	1.2	1.2	day <sup>-1</sup>
$P_0$	PDGF boundary condition	$1.4 \times 10^{-3}$	0	$10^{-3}$	$0.28 \times 10^{-3}$	$0.45 \times 10^{-3}$	mg/cm <sup>3</sup>
$n$	# Injury Points	1	0	1	2	1	none

Table 4.7: Parameter values for equations (4.1)-(4.4) and equations (4.15) and (4.16) used to generate Figures 4.8 to 4.18. Abbreviations: MC = Macrophage Cells, NC = Necrotic Cells, O<sub>2</sub> = Oxygen, PDGF = Platelet Derived Growth Factor.

### 4.3 Conclusion

In this chapter, we proposed an integrated model of atherosclerosis. A system of PDEs was considered for modeling the dynamics of macrophages, chemoattractants, oxygen and necrotic core concentrations. The distribution of Ox-LDLs was given as a Gaussian (or a combination of Gaussian) functions to give us more freedom in controlling their concentration and location. In addition, we used a PDE to model the dynamics of PDGF concentration. This PDE was decoupled from the rest of the PDEs and we used its solution to construct our mechanical growth tensor. All of the PDEs in this problem were solved in their steady states since their timescale is much smaller than the mechanical growth timescale.

Morphoelasticity requires us to apply the growth to the reference domain. However, the PDGF solution is found in a deformed domain. To overcome this issue, we mapped back the values of PDGF field in each element to the same element in the reference domain. This way, we were able to get a spatially dependent growth tensor with respect to the distribution of PDGF in the reference domain.

We introduced our integrated model on 5 domains extracted from medical IVUS images [54]. We defined 4 time dependent biological mechanisms corresponding to our model: changes in Ox-LDL distribution, changes in inflammation, development of vasa vasora and increasing oxygenation. By manipulating the terms in our model pertaining to these mechanisms, we were able to qualitatively mimic the follow-up state of the plaque in the IVUS images from their baseline state. In summary, we were able to see that despite increasing inflammation TCFA can convert to ThFCA by increasing oxygenation. A TCFA can turn into a fibrous plaque by healing the injured sites on the endothelium and gradually reducing the infiltration of LDLs into the intima and consequently reducing inflammation. Also a TCFA location can change by changing the location of Ox-LDL source in the intima. Furthermore, a PIT can exacerbate and turn into TCFA by increasing infiltration of LDLs and macrophages. Finally, ThFCA can become TFCA by controlling the location of vasa vasora. In all of these simulations, oxygen sources and the shape of Ox-LDL distribution had a significant effect on the

shape of the necrotic core. One caveat of this model is neglecting the mechanical properties of the necrotic core. Necrotic cores are known to have different mechanical properties than the fibrotic plaques they reside in [13, 47, 59]. We speculate that this difference can contribute to the thinning of the intima as a result of a vanishing necrotic core (Case B from Kubo’s paper).

Although atherosclerosis has been modeled by many researchers, we believe that our integrated approach reproduces some medically relevant observations. We showed that in addition to a certain amount of inflammation, the intima needs to be thick enough for the formation of a necrotic core. However, the time needed for the simulation in our current model increases dramatically with each PDE added to our histological system of PDEs. This can prevent us from making a more realistic biochemical model of atherosclerosis. The author believes that parallelizing the current algorithms can help resolve this issue.

Due to the physical strain that the catheterization puts on patients, there are not many patient specific IVUS images available. There is usually a baseline image and a follow-up image taken about a year later. Our models can help medical researchers gain some insight about the plaque morphology during this time. In addition, our simulation allows us to speculate on different mechanisms that lead to different follow-up images.

## Chapter 5

### CONCLUSION

In this dissertation, we have investigated biomechanical and biochemical aspects of atherosclerosis. At first, we studied the mechanics of a local plaque growth inside a cylindrical domain. By using morphoelasticity as our mathematical framework and a Holzapfel type strain energy, we explored the effect of growth in each cylindrical direction on Glagov remodeling and strain energy. We saw that the radial growth is the main reason for the arterial encroachment while the circumferential growth mainly contributed to outward remodeling. We also observed that the radial direction is the most energetically favorable direction of growth. Thereafter, we proposed a novel method motivated by the common pressure-displacement minimization method for incompressible materials. But instead of the pressure field, we minimized the energy with respect to growth parameters and displacement. The result was an anisotropic growth with the radial direction as the dominant direction of growth. We compared this anisotropic growth with an isotropic case with the same growth Jacobian and we saw that the anisotropic case introduced more luminal stenosis than the isotropic case. This radially dominant anisotropic growth was in line with experimental results.

Next, we investigated the effect of growth on the residual strain. When cut radially, the cross sections of arteries spring open. This proves the existence of residual stress/strain inside unloaded cross sections. The angle of the opened sector after the radial cut is called the opening angle and has been used by many researchers to estimate the residual stress/strain. We used a general domain extracted from IVUS images to see the effect of growth on the opening angle. We started with growth in a single direction. We saw that growth in the fiber direction creates a larger opening angle than the other two directions. Then we compared the most energetically favorable anisotropic growth

scheme (acquired by our two field minimization) with an isotropic growth with the same Jacobian. We saw that for both cases, strain in the fiber direction was spread out though the whole domain while it was more localized in the other two directions. Due to the geometry of our problem, we saw that the opening angle and strains for the isotropic and anisotropic growth were almost the same. However, having a longer arterial cross section will have the minimization scheme suppress the growth in the axial direction more significantly. Therefore, the difference between the two cases will become more apparent. Our results from chapter 2 and 3 show that plaques can cause significant stenosis and residual strain even when the associated energy is low.

We believe our approach can help experimentalists estimate the residual strain for an artery as a function of stenosis. Also since growth in the fiber direction produces the largest opening angle among the other directions of growth, we think by controlling the growth in this direction one might be able to postpone the plaque rupture.

Finally, we proposed an integrated model of atherosclerosis. We developed a model that takes into consideration the histological aspect of atherosclerotic plaque as well as the mechanical aspect. For the histology, we used a system of PDEs describing the dynamics of macrophages, chemoattractants, oxygen and the necrotic core. We also included a Gaussian function for the distribution of Ox-LDLs. In addition, we described the dynamics of PDGF using a PDE which was decoupled from the aforementioned system of PDEs. The solution to this PDE (mapped back into the reference domain) was used to construct a growth tensor which was used to grow the artery from its reference configuration. We used 5 IVUS images from Kubo's paper [54] to construct our domains. We proposed 4 different mechanisms pertaining to time dependent terms in our model to explain the follow-up plaque states from Kubo's study. The four mechanisms were: changes in Ox-LDL distribution, changes in inflammation, development of vasa vasora and increasing oxygenation. All these factors are thought to be important in affecting atherosclerosis in different stages. We were able to mimic the plaque follow-up states qualitatively using these mechanisms. We believe that the histological part of our algorithm has some room for improvement. By adding more

factors and maybe coupling the PDGF equation with the rest of the PDEs, we can have a clearer understanding of the development of plaques.

This dissertation opens many doors for future work. Numerical or algorithmic improvement of the simulations can lead to a deeper understanding of the plaque histology. Right now, we manually inscribe the location of growth but incorporating fluid-solid interaction models can make the simulations more realistic. More specifically, we could introduce a simple Newtonian Poiseuille flow inside the lumen of a 2D cross section. This determines sites of lower flow velocity which would lead to endothelial dysfunction and the histological and mechanical responses discussed in this thesis. Furthermore, we could evolve the necrotic core using a level set method and integrate the resulting model into image processing algorithms to analyze patient-specific data. The necrotic core could have its own mechanical properties and act as a separate domain. This might help explaining the thinning of the intima in the event of a necrotic core decline. Finally, we hope this work can stimulate further collaboration between clinicians and mathematicians.

## BIBLIOGRAPHY

- [1] Martine Ben Amar and Alain Goriely. Growth and instability in elastic tissues. *Journal of the Mechanics and Physics of Solids*, 53(10):2284–2319, 2005.
- [2] American Heart Association et al. Cardiovascular disease: A costly burden for America projections through 2035, 2017.
- [3] Utkarsh Ayachit. *The paraview guide: a parallel visualization application*. Kitware, Inc., 2015.
- [4] Valentina Balbi and Pasquale Ciarletta. Morpho-elasticity of intestinal villi. *Journal of the Royal Society Interface*, 10(82):20130109, 2013.
- [5] Christie M Ballantyne, Joel Neutel, Anne Cropp, William Duggan, Ellen Q Wang, David Plowchalk, Kevin Sweeney, Nitin Kaila, John Vincent, and Harold Bays. Results of bococizumab, a monoclonal antibody against proprotein convertase subtilisin/kexin type 9, from a randomized, placebo-controlled, dose-ranging study in statin-treated subjects with hypercholesterolemia. *The American Journal of Cardiology*, 115(9):1212–1221, 2015.
- [6] Martine Ben Amar, Min Wu, Miguel Trejo, and Michael Atlan. Morphoelasticity of inflammatory fibrosis: the case of capsular contracture. *Journal of the Royal Society Interface*, 12(111):20150343, 2015.
- [7] Emelia J Benjamin, Paul Muntner, and Márcio Sommer Bittencourt. Heart disease and stroke statistics-2019 update: a report from the american heart association. *Circulation*, 139(10):e56–e528, 2019.
- [8] T Bjornheden, M Levin, M Evaldsson, and O Wiklund. Evidence of hypoxic areas within the arterial wall in vivo. *Arteriosclerosis, Thrombosis, and Vascular Biology*, 19(4):870–876, 1999.
- [9] Tommy Boone. *Introduction to exercise physiology*. Jones & Bartlett Publishers, 2014.
- [10] Herman Branson. The flow of a viscous fluid in an elastic tube: a model of the femoral artery. *The Bulletin of Mathematical Biophysics*, 7(4):181–188, 1945.

- [11] S Lori Bridal, Paul Fornès, Patrick Bruneval, and Geneviève Berger. Parametric (integrated backscatter and attenuation) images constructed using backscattered radio frequency signals (25–56 mhz) from human aortae in vitro. *Ultrasound in Medicine & Biology*, 23(2):215–229, 1997.
- [12] Michael S Brown and Joseph L Goldstein. Lipoprotein metabolism in the macrophage: implications for cholesterol deposition in atherosclerosis. *Annual Review of Biochemistry*, 52(1):223–261, 1983.
- [13] Chen-Ket Chai, Ali C Akyildiz, Lambert Speelman, Frank JH Gijsen, Cees WJ Oomens, Marc RHM van Sambeek, Aad van der Lugt, and Frank PT Baaijens. Local axial compressive mechanical properties of human carotid atherosclerotic plaquescharacterisation by indentation test and inverse finite element analysis. *Journal of Biomechanics*, 46(10):1759–1766, 2013.
- [14] Alexander D Chalmers, Christina A Bursill, and Mary R Myerscough. Nonlinear dynamics of early atherosclerotic plaque formation may determine the efficacy of high density lipoproteins (HDL) in plaque regression. *PLoS ONE*, 12(11), 2017.
- [15] Alexander D Chalmers, Anna Cohen, Christina A Bursill, and Mary R Myerscough. Bifurcation and dynamics in a mathematical model of early atherosclerosis. *Journal of Mathematical Biology*, 71(6-7):1451–1480, 2015.
- [16] Cheng-Jen Chuong and Yuan-Cheng Fung. Residual stress in arteries. In *Frontiers in Biomechanics*, pages 117–129. Springer, 1986.
- [17] CJ Chuong and YC Fung. Three-dimensional stress distribution in arteries. 1983.
- [18] CA Cobbold, JA Sherratt, and SRJ Maxwell. Lipoprotein oxidation and its significance for atherosclerosis: a mathematical approach. *Bulletin of Mathematical Biology*, 64(1):65–95, 2002.
- [19] Kristopher S Cunningham and Avrum I Gotlieb. The role of shear stress in the pathogenesis of atherosclerosis. *Laboratory Investigation*, 85(1):9–23, 2005.
- [20] Alejandro Diego, Armando Pérez de Prado, Carlos Cuellas, Claudia Pérez-Martínez, Manuel Gonzalo-Orden, Jose R Altonaga, Antonio de Miguel, Marta Regueiro, Jose Ajenjo, Fernando Sánchez-Lasheras, et al. Instent restenosis related to vessel injury score degree. are current experimental models valid for drug-eluting stents analysis? *Revista Española de Cardiología (English Edition)*, 64(9):745–751, 2011.
- [21] N El Khatib, S Genieys, and V Volpert. Atherosclerosis initiation modeled as an inflammatory process. *Mathematical Modelling of Natural Phenomena*, 2(2):126–141, 2007.

- [22] CG Fabricant, J Fabricant, MM Litrenta, and CR Minick. Virus-induced atherosclerosis. *The Journal of Experimental Medicine*, 148(1):335–340, 1978.
- [23] Erling Falk. Pathogenesis of atherosclerosis. *Journal of the American College of Cardiology*, 47(8 Supplement):C7–C12, 2006.
- [24] Pak-Wing Fok. Growth of necrotic cores in atherosclerotic plaque. *Mathematical Medicine and Biology: A Journal of the IMA*, 29(4):301–327, 2012.
- [25] Pak-Wing Fok. Multi-layer mechanical model of glagov remodeling in coronary arteries: differences between in-vivo and ex-vivo measurements. *PLoS ONE*, 11(7), 2016.
- [26] Pak-Wing Fok and Kun Gou. Finite element simulation of intimal thickening in 2D multi-layered arterial cross sections by morphoelasticity. *Computer Methods in Applied Mechanics and Engineering*, 363:112860, 2020.
- [27] Douglas J Francis, Christopher R Parish, Mark McGarry, Fernando S Santiago, Harry C Lowe, Kathryn J Brown, John A Bingley, Ian P Hayward, William B Cowden, Julie H Campbell, et al. Blockade of vascular smooth muscle cell proliferation and intimal thickening after balloon injury by the sulfated oligosaccharide PI-88: phosphomannopentaose sulfate directly binds FGF-2, blocks cellular signaling, and inhibits proliferation. *Circulation Research*, 92(8):e70–e77, 2003.
- [28] YC Fung and SQ Liu. Change of residual strains in arteries due to hypertrophy caused by aortic constriction. *Circulation Research*, 65(5):1340–1349, 1989.
- [29] T Christian Gasser and Gerhard A Holzapfel. Modeling plaque fissuring and dissection during balloon angioplasty intervention. *Annals of Biomedical Engineering*, 35(5):711–723, 2007.
- [30] Christophe Geuzaine and Jean-Francois Remacle. GMSH reference manual. *Free Software Foundation Inc., USA*, 2003.
- [31] Christophe Geuzaine and Jean-François Remacle. GMSH: A 3D finite element mesh generator with built-in pre-and post-processing facilities. *International Journal for Numerical Methods in Engineering*, 79(11):1309–1331, 2009.
- [32] Samaneh Ghazanfari, A Driessens-Mol, GJ Strijkers, FMW Kanters, FPT Baaijens, and CVC Bouter. A comparative analysis of the collagen architecture in the carotid artery: second harmonic generation versus diffusion tensor imaging. *Biochemical and Biophysical Research Communications*, 426(1):54–58, 2012.
- [33] George D Giannoglou, Antonios P Antoniadis, Yiannis S Chatzizisis, Efthalia Damvopoulos, George E Parcharidis, and George E Louridas. Prevalence of narrowing  $\geq 50\%$  of the left main coronary artery among 17,300 patients having

- coronary angiography. *The American Journal of Cardiology*, 98(9):1202–1205, 2006.
- [34] Seymour Glagov, Elliot Weisenberg, Christopher K Zarins, Regina Stankunavicius, and George J Kolettis. Compensatory enlargement of human atherosclerotic coronary arteries. *New England Journal of Medicine*, 316(22):1371–1375, 1987.
  - [35] SE Greenwald, JE Moore Jr, A Rachev, TPC Kane, and J-J Meister. Experimental investigation of the distribution of residual strains in the artery wall. 1997.
  - [36] Daniel M Greif, Maya Kumar, Janet K Lighthouse, Justine Hum, Andrew An, Ling Ding, Kristy Red-Horse, F Hernan Espinoza, Lorin Olson, Stefan Offermanns, et al. Radial construction of an arterial wall. *Developmental Cell*, 23(3):482–493, 2012.
  - [37] Peter H Groves, Adrian P Banning, William J Penny, Malcolm J Lewis, Hilary A Cheadle, and Andrew C Newby. Kinetics of smooth muscle cell proliferation and intimal thickening in a pig carotid model of balloon injury. *Atherosclerosis*, 117(1):83–96, 1995.
  - [38] Morton E Gurtin. *Topics in finite elasticity*, volume 35. SIAM, 1981.
  - [39] Masae Haga, Akimasa Yamashita, Jacek Paszkowiak, Bauer E Sumpio, and Alan Dardik. Oscillatory shear stress increases smooth muscle cell proliferation and akt phosphorylation. *Journal of Vascular Surgery*, 37(6):1277–1284, 2003.
  - [40] Göran K Hansson and Andreas Hermansson. The immune system in atherosclerosis. *Nature Immunology*, 12(3):204, 2011.
  - [41] Wenrui Hao and Avner Friedman. The LDL-HDL profile determines the risk of atherosclerosis: a mathematical model. *PLoS ONE*, 9(3), 2014.
  - [42] Christopher J Hardy, Manojkumar Saranathan, Yudong Zhu, and Robert D Darrow. Coronary angiography by real-time mri with adaptive averaging. *Magnetic Resonance in Medicine: An Official Journal of the International Society for Magnetic Resonance in Medicine*, 44(6):940–946, 2000.
  - [43] Bo Herrlin and Christopher Sylvén. Increased arterial oxygen contentan important compensatory mechanism in chronic moderate heart failure. *Cardiovascular Research*, 25(5):384–390, 1991.
  - [44] Gerhard A Holzapfel. Nonlinear solid mechanics: a continuum approach for engineering science. *Meccanica*, 37(4):489–490, 2002.

- [45] Gerhard A Holzapfel, Thomas C Gasser, and Ray W Ogden. A new constitutive framework for arterial wall mechanics and a comparative study of material models. *Journal of Elasticity and the Physical Science of Solids*, 61(1-3):1–48, 2000.
- [46] Gerhard A Holzapfel, Gerhard Sommer, Christian T Gasser, and Peter Regitnig. Determination of layer-specific mechanical properties of human coronary arteries with nonatherosclerotic intimal thickening and related constitutive modeling. *American Journal of Physiology-Heart and Circulatory Physiology*, 2005.
- [47] Gerhard A Holzapfel, Gerhard Sommer, and Peter Regitnig. Anisotropic mechanical properties of tissue components in human atherosclerotic plaques. *J. Biomech. Eng.*, 126(5):657–665, 2004.
- [48] Lillemor Mattsson Hultén and Max Levin. The role of hypoxia in atherosclerosis. *Current Opinion in Lipidology*, 20(5):409–414, 2009.
- [49] M Iwaki, SF Wickham, K Ikezaki, T Yanagida, and WM Shih. A programmable DNA origami nanospring that reveals force-induced adjacent binding of myosin VI heads. *Nature Communications*, 7(1):1–10, 2016.
- [50] Louis N Katz. Experimental atherosclerosis. *Circulation*, 5(1):101–114, 1952.
- [51] DN Kim, H Imai, J Schmee, KT Lee, and WA Thomas. Intimal cell mass-derived atherosclerotic lesions in the abdominal aorta of hyperlipidemic swine part 1. cell of origin, cell divisions and cell losses in first 90 days on diet. *Atherosclerosis*, 56(2):169–188, 1985.
- [52] Vyacheslav A Korshunov and Bradford C Berk. Strain-dependent vascular remodeling: the Glagov phenomenon is genetically determined. *Circulation*, 110(2):220–226, 2004.
- [53] Vyacheslav A Korshunov, Stephen M Schwartz, and Bradford C Berk. Vascular remodeling: hemodynamic and biochemical mechanisms underlying Glagov's phenomenon. *Arteriosclerosis, Thrombosis, and Vascular Biology*, 27(8):1722–1728, 2007.
- [54] Takashi Kubo, Akiko Maehara, Gary S Mintz, Hiroshi Doi, Kenichi Tsujita, So-Yeon Choi, Osamu Katoh, Kenya Nasu, Andreas Koenig, Michael Pieper, et al. The dynamic nature of coronary artery lesion morphology assessed by serial virtual histology intravascular ultrasound tissue characterization. *Journal of the American College of Cardiology*, 55(15):1590–1597, 2010.
- [55] Hans Petter Langtangen and Anders Logg. *Solving PDEs in Python: The FEniCS Tutorial I*, volume 1. Springer International Publishing, 2016.

- [56] CM Lawrence, DV Nelson, E Udd, and T Bennett. A fiber optic sensor for transverse strain measurement. *Experimental Mechanics*, 39(3):202–209, 1999.
- [57] Peter Libby, Paul M Ridker, and Attilio Maseri. Inflammation and atherosclerosis. *Circulation*, 105(9):1135–1143, 2002.
- [58] Ju Liu and Alison L Marsden. A unified continuum and variational multiscale formulation for fluids, solids, and fluid–structure interaction. *Computer Methods in Applied Mechanics and Engineering*, 337:549–597, 2018.
- [59] Howard M Loree, Barbara J Tobias, Lorna J Gibson, Roger D Kamm, Donald M Small, and Richard T Lee. Mechanical properties of model atherosclerotic lesion lipid pools. *Arteriosclerosis and Thrombosis: A Journal of Vascular Biology*, 14(2):230–234, 1994.
- [60] TE Machella. The velocity of blood flow in arteries in animals. *American Journal of Physiology-Legacy Content*, 115(3):632–644, 1936.
- [61] Douglas D Mair and Donald G Ritter. Factors influencing systemic arterial oxygen saturation in complete transposition of the great arteries. *American Journal of Cardiology*, 31(6):742–748, 1973.
- [62] Guido Majno and Isabelle Joris. Apoptosis, oncosis, and necrosis. an overview of cell death. *The American Journal of Pathology*, 146(1):3, 1995.
- [63] Adel M Malek, Seth L Alper, and Seigo Izumo. Hemodynamic shear stress and its role in atherosclerosis. *Jama*, 282(21):2035–2042, 1999.
- [64] RH Mohiaddin, ED Burman, SK Prasad, A Varghese, RS Tan, SA Collins, RL Hughes, PD Gatehouse, P Jhooti, DB Longmore, et al. Glagov remodeling of the atherosclerotic aorta demonstrated by cardiovascular magnetic resonance: the CORDA asymptomatic subject plaque assessment research (CASPAR) project. *Journal of Cardiovascular Magnetic Resonance*, 6(2):517–525, 2004.
- [65] Mary Jo Mulligan-Kehoe. The vasa vasorum in diseased and nondiseased arteries. *American Journal of Physiology-Heart and Circulatory Physiology*, 298(2):H295–H305, 2010.
- [66] Santa Mundi, Marika Massaro, Egeria Scoditti, Maria Annunziata Carluccio, Victor WM van Hinsbergh, Marial Luisa Iruela-Arispe, and Raffaele De Caterina. Endothelial permeability, LDL deposition, and cardiovascular risk factors a review. *Cardiovascular Research*, 114(1):35–52, 2018.
- [67] Anuja Nair, Barry D Kuban, E Murat Tuzcu, Paul Schoenhagen, Steven E Nissen, and D Geoffrey Vince. Coronary plaque classification with intravascular ultrasound radiofrequency data analysis. *Circulation*, 106(17):2200–2206, 2002.

- [68] Kazunori Nakagawa and Yutaka Nakashima. Pathologic intimal thickening in human atherosclerosis is formed by extracellular accumulation of plasma-derived lipids and dispersion of intimal smooth muscle cells. *Atherosclerosis*, 274:235–242, 2018.
- [69] Yutaka Nakashima, Thomas N Wight, and Katsuo Sueishi. Early atherosclerosis in humans: role of diffuse intimal thickening and extracellular matrix proteoglycans. *Cardiovascular Research*, 79(1):14–23, 2008.
- [70] Raymond W Ogden. *Non-linear elastic deformations*. Courier Corporation, 1997.
- [71] Jacques Ohayon, Olivier Dubreuil, Philippe Tracqui, Simon Le Floc'h, Gilles Rioufol, Lara Chalabreysse, Françoise Thivolet, Roderic I Pettigrew, and Gérard Finet. Influence of residual stress/strain on the biomechanical stability of vulnerable coronary plaques: potential impact for evaluating the risk of plaque rupture. *American Journal of Physiology-Heart and Circulatory Physiology*, 293(3):H1987–H1996, 2007.
- [72] Robert D Okada, Charles A Boucher, H William Strauss, and Gerald M Po-host. Exercise radionuclide imaging approaches to coronary artery disease. *The American Journal of Cardiology*, 46(7):1188–1204, 1980.
- [73] Tobias Olsson and Anders Klarbring. Residual stresses in soft tissue as a consequence of growth and remodeling: application to an arterial geometry. *European Journal of Mechanics-A/Solids*, 27(6):959–974, 2008.
- [74] Charles S Peskin. Numerical analysis of blood flow in the heart. *Journal of Computational Physics*, 25(3):220–252, 1977.
- [75] Jean Poiseuille. Recherches expérimentales sur le mouvement des liquides dans les tubes de très petits diamètres [experimental research on the movement of liquids in capillary of very small diameters]. *Comptes Rendus Hebdomadaires des Séances de l'Académie des Sciences*, 11:1041–1048, 1840.
- [76] Alfio Quarteroni, Stefania Ragni, and Alessandro Veneziani. Coupling between lumped and distributed models for blood flow problems. *Computing and Visualization in Science*, 4(2):111–124, 2001.
- [77] Elaine W Raines. PDGF and cardiovascular disease. *Cytokine & Growth Factor Reviews*, 15(4):237–254, 2004.
- [78] Edward K Rodriguez, Anne Hoger, and Andrew D McCulloch. Stress-dependent finite growth in soft elastic tissues. *Journal of Biomechanics*, 27(4):455–467, 1994.
- [79] Ankit Rohatgi. Webplotdigitizer, 2019.

- [80] Russell Ross. Atherosclerosis is an inflammatory disease. *New England Journal of Medicine*, 340(2):115–126, 1999.
- [81] Russell Ross and John A Glomset. The pathogenesis of atherosclerosis. *New England Journal of Medicine*, 295(7):369–377, 1976.
- [82] Russell Ross, Elaine W Raines, and Daniel F Bowen-Pope. The biology of platelet-derived growth factor. *Cell*, 46(2):155–169, 1986.
- [83] Stanley A Rubin, Harvey V Brown, and HJ Swan. Arterial oxygenation and arterial oxygen transport in chronic myocardial failure at rest, during exercise and after hydralazine treatment. *Circulation*, 66(1):143–148, 1982.
- [84] Shiva Rudraraju, Derek E Moulton, Régis Chirat, Alain Goriely, and Krishna Garikipati. A computational framework for the morpho-elastic development of molluskan shells by surface and volume growth. *PLoS Computational Biology*, 15(7):e1007213, 2019.
- [85] Arnav Sanyal and Hai-Chao Han. Artery buckling affects the mechanical stress in atherosclerotic plaques. *Biomedical Engineering Online*, 14(S1):S4, 2015.
- [86] Stephen M Schwartz, Denis deBlois, and Edward RM O'Brien. The intima: soil for atherosclerosis and restenosis. *Circulation Research*, 77(3):445–465, 1995.
- [87] Spencer J Sherwin, Luca Formaggia, Joaquim Peiro, and V Franke. Computational modelling of 1D blood flow with variable mechanical properties and its application to the simulation of wave propagation in the human arterial system. *International Journal for Numerical Methods in Fluids*, 43(6-7):673–700, 2003.
- [88] Kentaro Shimokado, Elaine W Raines, David K Madtes, Thomas B Barrett, Earl P Benditt, and Russell Ross. A significant part of macrophage-derived growth factor consists of at least two forms of PDGF. *Cell*, 43(1):277–286, 1985.
- [89] Mien Sho, Eiketsu Sho, Tej M Singh, Masayo Komatsu, Akihiro Sugita, Cheng-pei Xu, Hiroshi Nanjo, Christopher K Zarins, and Hirotake Masuda. Subnormal shear stress-induced intimal thickening requires medial smooth muscle cell proliferation and migration. *Experimental and Molecular Pathology*, 72(2):150–160, 2002.
- [90] Judith C Sluimer and Mat J Daemen. Novel concepts in atherogenesis: angiogenesis and hypoxia in atherosclerosis. *The Journal of Pathology: A Journal of the Pathological Society of Great Britain and Ireland*, 218(1):7–29, 2009.
- [91] George A Stouffer and Gary K Owens. TGF-beta promotes proliferation of cultured SMC via both PDGF-AA-dependent and PDGF-AA-independent mechanisms. *The Journal of Clinical Investigation*, 93(5):2048–2055, 1994.

- [92] Larry A Taber and Jay D Humphrey. Stress-modulated growth, residual stress, and vascular heterogeneity. *J. Biomech. Eng.*, 123(6):528–535, 2001.
- [93] Wei-Che Tsai, Keng-Yi Wu, Gen-Min Lin, Sy-Jou Chen, Wei-Shiang Lin, Shih-Ping Yang, Shu-Meng Cheng, and Chin-Sheng Lin. Clinical characteristics of patients less than forty years old with coronary artery disease in Taiwan: a cross-sectional study. *Acta Cardiologica Sinica*, 33(3):233, 2017.
- [94] Hiroto Ueba, Masanobu Kawakami, and Toshio Yaginuma. Shear stress as an inhibitor of vascular smooth muscle cell proliferation: role of transforming growth factor- $\beta$ 1 and tissue-type plasminogen activator. *Arteriosclerosis, Thrombosis, and Vascular Biology*, 17(8):1512–1516, 1997.
- [95] Ramesh N Vaishnav and Jafar Vossoughi. Residual stress and strain in aortic segments. *Journal of Biomechanics*, 20(3):235–239, 1987.
- [96] C Velican and Doina Velican. Intimal thickening in developing coronary arteries and its relevance to atherosclerotic involvement. *Atherosclerosis*, 23(2):345–355, 1976.
- [97] Stefan Verheyen, Guido RY De Meyer, Rob Kramps, Mark M Kockx, Luc CA Van Damme, Babak Mousavi Gourabi, Michiel WM Knaapen, Glenn Van Langenhove, and Patrick W Serruys. Intravascular thermography: Immediate functional and morphological vascular findings. *European Heart Journal*, 25(2):158–165, 2004.
- [98] Renu Virmani, Jagat Narula, Martin B Leon, and James T Willerson. *The vulnerable atherosclerotic plaque: strategies for diagnosis and management*. John Wiley & Sons, 2008.
- [99] HM Wang, H Gao, XY Luo, C Berry, BE Griffith, RW Ogden, and TJ Wang. Structure-based finite strain modelling of the human left ventricle in diastole. *International Journal for Numerical Methods in Biomedical Engineering*, 29(1):83–103, 2013.
- [100] HM Wang, XY Luo, H Gao, RW Ogden, BE Griffith, C Berry, and TJ Wang. A modified holzapfel-ogden law for a residually stressed finite strain model of the human left ventricle in diastole. *Biomechanics and Modeling in Mechanobiology*, 13(1):99–113, 2014.
- [101] Brian H Wayman, W Robert Taylor, Alexander Rachev, and Raymond P Vito. Arteries respond to independent control of circumferential and shear stress in organ culture. *Annals of Biomedical Engineering*, 36(5):673–684, 2008.
- [102] Si-Fan Yin, Shi-Lei Xue, Bo Li, and Xi-Qiao Feng. Bio–chemo–mechanical modeling of growing biological tissues: Finite element method. *International Journal of Non-Linear Mechanics*, 108:46–54, 2019.

- [103] Olek C Zienkiewicz and Robert L Taylor. *The finite element method for solid and structural mechanics*. Elsevier, 2005.

## Appendix A

### DOMAIN AND MESH GENERATION

In chapters 2 and 3, we started using general domains extracted from IVUS images. To create these domains for simulations we take the following steps:

1. Find a list of point coordinates on the boundaries of the arteries in the IVUS images.
2. Find a the best fit trigonometric polynomial for these points.
3. Use GMSH spline to create the boundaries.
4. Use GMSH to create mesh and sent it to python for simulations.

To find a list of point coordinates on the boundaries, we upload the image on the website <https://automeris.io/WebPlotDigitizer> [79].

This website creates an excel file with the coordinates that can be uploaded to Matlab. From there, we were able to use Matlab to find the coefficients of the best fit trigonometric polynomial for each boundary. Below are the equations for the endothelium and IEL for case A:

$$\begin{aligned} f_1(\Theta) = & 0.7512 + 0.0124 \cos(\Theta) + 0.0414 \cos(2\Theta) + 0.0120 \cos(3\Theta) + 0.01111 \cos(4\Theta) \\ & - 0.0061 \cos(5\Theta) - 0.0008 \cos(6\Theta) - 0.00001 \cos(7\Theta) + 0.0033 \cos(8\Theta) + 0.0217 \sin(\Theta) \\ & - 0.0197 \sin(2\Theta) - 0.0027 \sin(3\Theta) - 0.0084 \sin(4\Theta) - 0.0135 \sin(5\Theta) - 0.0034 \sin(6\Theta) \\ & - 0.0001 \sin(7\Theta) - 0.0048 \sin(8\Theta) \end{aligned} \tag{A.1}$$

$$\begin{aligned}
f_2(\Theta) = & 1.0284 + 0.0362 \cos(\Theta) - 0.0557 \cos(2\Theta) + 0.0190 \cos(3\Theta) - 0.0185 \cos(4\Theta) \\
& + 0.0038 \cos(5\Theta) + 0.0045 \cos(6\Theta) - 0.0002 \cos(7\Theta) + 0.0006 \cos(8\Theta) - 0.1984 \sin(\Theta) \\
& - 0.0173 \sin(2\Theta) - 0.0008 \sin(3\Theta) - 0.0133 \sin(4\Theta) - 0.0026 \sin(5\Theta) - 0.0066 \sin(6\Theta) \\
& - 0.0029 \sin(7\Theta) + 0.0064 \sin(8\Theta)
\end{aligned} \tag{A.2}$$

where  $0 \leq \Theta \leq 2\pi$ . For the boundary between media and adventitia and the outer boundary, we just add two different constants to  $f_2(\Theta)$ . After finding these equations, we are ready to feed them to our mesh generator. GMSH is an open source 3D finite element mesh generator with a built-in CAD engine and post processor [30, 31]. GMSH has a user friendly graphical interface that allows the user to create simple meshes. It also has its own script language which enables us to create complicated boundaries like the ones above. Therefore, we use equations (A.1) and (A.2) in GMSH script to sample boundary points. Then with the use of GMSH function `Spline`, we can create continuous closed curves resembling the boundaries in the IVUS images, see Figure A.1.

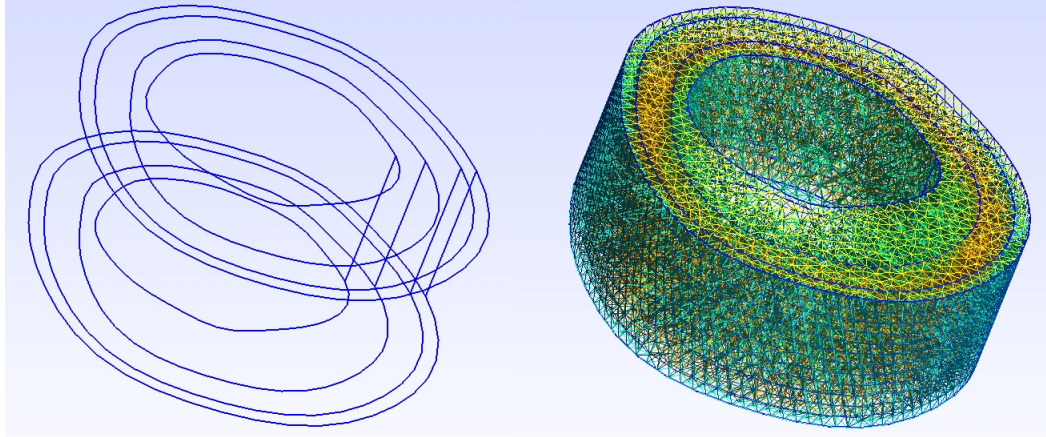


Figure A.1: A sample 3D domain and its meshed version in GMSH environment

All the GMSH scripts have .geo extension and the mesh will be saved with a .msh extension. This is the key feature that enables us to use these meshes on FEniCS. Upon installing FEniCS on a Linux or Mac computer the following command will be added to the terminal commands.

```
dolfin-convert Your-GMSH-Output.msh Mesh.xml
```

This command will convert your mesh and all of its facet and physical elements into files with .xml extension. This is the extension that can be imported on FEniCS. To see a sample of .geo, .msh and .xml files refer to the github address:

[https://github.com/nmirzaei/ATHEROSCLEROSIS-IN-3D-WITH-HISTOLOGY  
/tree/master/A\\_2D](https://github.com/nmirzaei/ATHEROSCLEROSIS-IN-3D-WITH-HISTOLOGY/tree/master/A_2D)

After simulations are done via FEniCS, the results are saved in .vtu or .pv. These are the extensions used by the software Paraview. This is an open source free software with many visualization and post processing tools [3]. It is also compatible with python and can export data in .csv format (with comma separated values) for further processing.

## Appendix B

### PARAMETERS FOR GAUSSIAN FUNCTIONS

Below you can find the parameters for equations (4.21)-(4.23) from chapter 4.

$i$	$L_i(t)$	$s_i$	$(x_0^{(i)}, y_0^{(i)})$
1	$0.77(t/12)$	20	(0.115, -0.534)
2	$t/12$	20	(0.324, -0.409)
3	$t/12$	20	(0.406, -0.164)
4	$0.9(t/12)$	30	(0.752, -0.353)
5	$0.9(t/12)$	30	(0.771, -0.057)
6	$0.9(t/12)$	45	(0.682, 0.195)
7	$0.55(t/12)$	50	(0.577, 0.405)
8	$0.19(t/12)$	55	(0.484, 0.525)
9	$0.13(t/12)$	55	(0.426, 0.594)
10	$0.1(t/12)$	60	(0.397, 0.608)

Table B.1: Parameters for equation (4.21).

$i$	$L_i$	$(x_0^{(i)}, y_0^{(i)})$	$j$	$f_j(t)$	$s_j$	$(x_1^{(j)}, y_1^{(j)})$
1	0.77	(0.66, 0.71)	1	$11.2(1 - t/24)$	40	(0.33, 0.64)
2	0.77	(1.00, -0.20)	2	$11.2(1 - t/12)$	40	(0.45, 0.41)
3	0.56	(0.04, -1.11)	3	$11.2(1 - t/36)$	40	(0.34, 0.94)
4	0.56	(0.64, -0.85)	4	11.2	40	(0.85, 0.93)
5	0.42	(-0.67, -0.95)	5	12.32	20	(0.89, -0.43)
			6	9.52	40	(0.29, -0.76)
			7	$9.52(1 - t/24)$	35	(0.11, -0.85)
			8	9.52	35	(-0.24, -0.90)
			9	$9.52(t/24)$	40	(-0.11, 0.74)
			10	9.52	40	(0.11, 0.58)
			11	$7.84(t/12)$	60	(0.25, 0.35)
			12	$7.84(t/12)$	60	(0.32, 0.18)
			13	$7.84(t/12)$	30	(0.90, 0.47)
			14	$7.84(t/12)$	40	(1.00, 0.08)
			15	$16.8(t/12)$	40	(0.81, -0.76)
			16	$1.12(t/12)$	40	(0.43, -1.00)
			17	$9.52(t/12)$	40	(-0.58, -0.83)
			18	$11.2(t/12)$	40	(0.33, 0.07)
			19	$4.48(t/12)$	60	(0.31, -0.2)
			20	$4.48(t/12)$	60	(0.96, -0.06)
			21	$5.6(t/12)$	60	(0.52, -0.63)

Table B.2: Parameters for equation (4.22) and (4.23).